THE UNIVERSITY
OF ADELAIDE
AUSTRALIA

The Influence of Jet Precession on Particle Distributions

Cristian Heinrich Birzer

School of Mechanical Engineering

The University of Adelaide

South Australia 5005

January, 2009

Supervisors:

Prof. G.J. Nathan

Dr. P.A.M. Kalt

Dr. N.L. Smith

In memory of my Father

Carl - Heinz Birzer

3rd of June, 1923 – 3rd of October, 2008

Abstract

This thesis assesses the extent to which jet precession can be used to control the mean and instantaneous particle distributions in particle-laden jet flows. Investigations were conducted, providing quantitative, planar measurements of instantaneous particle distributions in the first 10 nozzle diameters of a particle-laden co-annular nozzle with centrally located Precessing Jet (PJ). Equipment was specifically designed to conduct the investigations, a laser diagnostic technique developed and a methodology to quantify particle clusters was devised. The experimental facilities are scaled to simulate the near burner region of a typical rotary cement kiln. The laser diagnostic technique, called *planar nephelometry*, enables non-intrusive, quantitative, instantaneous, planar measurements of particle distributions without the need to identify individual particles. The methodology to quantify particle clusters is designed to enable statistical comparison of clusters without ambiguity.

Measurements of the influence of particle mass loading and jet precession on the distribution of particles emerging from an particle-laden co-annular nozzle, with a centrally located PJ nozzle, are presented. These data include mean and standard deviation of the particle distributions and statistics on particle cluster characteristics. The results indicate that small amounts of momentum through the PJ nozzle causes an elongation of the jet, but larger amounts of momentum through the PJ nozzle will result in a wider mean particle distribution and greater mean centreline decay rate. An increase in jet precession also results in an increase in the fluctuations in the particle distributions.

The transition is determined by the interplay of momentum of the particle-laden and precessing streams.

The physical characteristics of identified particle clusters in the instantaneous planar flow field are also influenced by jet precession. An initial increase in the amount of jet precession results in an overall decrease in the average number of both small- and large-clusters. The size of small-clusters generally reduces with increasing jet precession, whereas large-clusters reach maximum sizes for an intermediate relative momentum of jet precession. Analogous to the influence of jet precession on the mean distribution of particles, increasing jet precession also results in a greater spread of small- and large-clusters.

Results also indicate that increasing the mass flow rate of particles results in an elongation of the jet. However, these variations correspond to an increase in annular jet momentum, rather than an addition of secondary phase. The particle mass flow rate has a minor influence on the general characteristics of particle clusters.

Acknowledgements

First and foremost I would like to thank my supervisors, Professor G.J. Nathan, Dr P.A.M. Kalt and Dr N.L. Smith for their support and assistance with this project.

A great deal of workshop assistance was required for the building of the wind tunnel and ancillary equipment. The Mechanical Engineering, Electronics and Chemical Engineering workshop staff, past and present, are therefore given a great deal of thanks.

It is acknowledged that this project would not have been possible without the financial assistance provided by the Australian Research Council and FCT-Combustion.

Finally, thanks goes to all my friends and family that have supported me.

Declaration

This work contains no material which has been accepted for the award of any other degree or diploma in any university or other tertiary institution and, to the best of my knowledge and belief, contains no material previously published or written by another person, except where due reference has been made in the text.

I give consent to this copy of my thesis, when deposited in the University Library, being made available for loan and photocopying, subject to the provisions of the Copyright Act 1968.

SIGNED: ..... DATE: .....

Contents

List of Tables

List of Figures

Notation

Latin

a	acceleration [ms^2]
A	area [m^2]
A_{total}	total cluster area [m^2]
$\overline{A_c}$	average cluster area [m^2]
a_{slip}	acceleration of a particle relative to a fluid [ms^{-2}]
C	constant [-]
C_D	drag coefficient [-]
C_κ	correction factor [-]
d	particle diameter [m]
D	nozzle / jet diameter [m]
d_{eq}	cluster equivalent diameter [m]
$\overline{d_{eq}}$	average cluster equivalent diameter [m]
f_p	frequency of precession [Hz]
F	force [N]
F_D	drag force [N]
G	momentum flux [Nm^{-2}]
I'	local corrected intensity of laser sheet [a.u.]
I_0	incident illumination [a.u.]
L	characteristics length [m]
m	mass [kg]
$\dot{m}$	mass flow rate [kgs^{-1}]
$\overline{N_c}$	average number of clusters [-]
n_p	number of particles in the volume [-]
P_c	cluster perimeter [m]

PF	pulverised fuel
PJ	Precessing Jet
r	radial location [m]
r_p	particle radius [m]
Re	Reynolds number [-]
S'	fluctuating signal [a.u.]
S	signal [a.u.]
$\overline{S}$	mean signal [a.u.]
Sk	Stokes number [-]
t	time [s]
u	velocity [ms^{-1}]
u_{slip}	velocity of a particle relative to a fluid [ms^{-1}]
U	characteristic fluid velocity [ms^{-1}]
V	volume [m^3]
$\dot{V}$	volume flow rate [m^{3}s^{-1}]
x	axial distance [m]
x_p	axial location of peak signal [m]

Greek

β	particle mass loading ratio [-]
λ	wavelength [m]
λ_I	integral-length / Taylor macro-scale [m]
λ_K	Kolmogorov length scale [m]
λ_M	characteristic width of flow / macro-scale [m]
λ_T	Taylor micro-scale [m]
μ	dynamic viscosity [Nsm^{-2}]
ϕ	particle / fluid volume fraction [-]
Φ	signal [a.u.]
ψ_{as}	Mie-scattering cross section [m^2]
ρ	density [kg/m^3]
τ	response time [s]
τ	transfer efficiencies [-]
ω	solid angle [rad]

Subscripts

ANN	annular stream
$ANN(f)$	fluid based annular stream
E	exit of nozzle
f	fluid
i	illumination
$inlet$	inlet of the nozzle
l	large-clusters
p	particle
p	pixel
P	peak
PJ	Precessing Jet
s	collection
s	small-clusters
$total$	total of three flow streams
V	volume
1	inlet orifice / throat
2	outlet orifice / lip
2,1	area / diameter
3,2	volume / area

.

Chapter 1

Introduction

1.1 Pollutant emissions from rotary cement kilns

Fossil fuel combustion has been a major source of energy since the industrial revolution. Heat generated by fossil fuel combustion has been used most notably for transportation, electricity generation and the production of glass, steel, lime, cement and other such materials. Side-effects of the emissions from fossil fuel combustion, including global warming and photochemical smog, are detrimental to the environment. Reductions in the production of these emissions are required and can be achieved via reducing fossil fuel use, as well as increasing the efficiency of fossil fuel combustion. Renewable fuels and energy sources are becoming increasingly viable as an alternative to fossil fuels. However, under present economic structures, the capital costs associated with harvesting alternative fuels and energy sources can be high, rendering them more expensive than fossil fuels for many applications. Therefore improving the efficiency of fossil fuel combustion is still required. One possible method to improve the efficiency of fossil fuel combustion is improving the mixing of the fuel with the combustion air. This can potentially be achieved by manipulating the flow from burners. For pulverised fuel

(PF) combustion systems, controlling the mixing of the fuel and the combustion air is possible with manipulation of the flows. In PF systems, regions of high localised particle concentrations, known as particle clusters, have possible benefits to combustion [Zhang and Wall, 1993]. The enhancement of particle clusters has been successfully achieved using a Precessing Jet (PJ) nozzle [Nathan et al., 2000]. However, there is limited knowledge of the fluid mechanics relating to particles clustering. Indeed there is not even a rigorous method to identify clusters. There is also limited knowledge of the time-averaged distribution of particles when influenced by PJ flows. The objective of the current body of work is to quantify time-averaged and instantaneous particle distributions in a PJ flow with a view to enable increased efficiency of coal combustion in PF fired rotary cement kilns.

Cement is the most extensively used building material in the world. Rotary kilns typically produce environments conducive to the specific endothermic processes required for cement production. A rotary cement kiln flame typically has temperatures of approximately 2000^oC generated by a burner located at the lower end of the kiln. Feed material is introduced at the higher end of the kiln, so that counter-flow heat exchange occurs between the flame and the feed material. As the feed material travels down the kiln it undergoes a calcining reaction at approximately 800^oC, followed by a clinkering reaction at approximately 1450^oC. The clinkered material is then cooled and ground to form cement powder. The quality of cement is influenced by the burner [Bauer, 1990]. High quality cement can be produced by highly radiant flames which produces a hot burning zone close to the exit of the kiln [Ono, 1980]. Such flames produce high clinker exit temperatures, allowing for rapid cooling, which is a major factor in determining clinker quality. However, the heat flux profile and mixing performance of the burner also influence fuel consumption, fuel efficiency, emissions of nitrogen monoxide, NO, and nitrogen dioxide, NO_2 (which are collectively known as NO_X) and energy efficiency [Rhine and Tucker, 1991, Nathan and Manias, 1995].

Approximately 90% of the world's cement kilns are PF fired and the most commonly

used PF is coal. Coal is cheaper than other fossil fuels in terms of mining, processing, transportation and storage. As at 1990 the world's known reserves of coal were predicted to last 200 years based on the consumption rate at 1988 [Fulkerson et al., 1990]. However, information from the Energy Information Administration, based on a combination of 2002 and 2005 statistics, indicates that there is approximately only 155 years of recoverable coal available, at current consumption rates [EIA, 2005]. Newly converted, well controlled combustion systems that use waste products to displace fossil fuels can often reduce emissions [Hansen, 1993]. However, fossil fuels are readily available and relatively inexpensive to recover. They can be used to generate many types of industrial flames, each designed to have favourable heat transfer characteristics for particular applications [Fulkerson et al., 1990].

The combustion of coal results in flame temperatures sufficiently high for cement production. However, it also produces numerous potentially harmful emissions including NO_X, the oxides of sulphur, (SO_X) and carbon dioxide (CO_2). Carbon dioxide is the world's most prevalent greenhouse gas and is produced by complete combustion of all carbon based fuels. Production rates of CO_2 are directly dependent on the carbon content and consumption of the fuel. Similarly, SO_X production is subject to the amount of sulphur in the fuel. Reductions of both CO_2 and SO_X are therefore subject to fuel composition and combustion efficiency. The production rates of NO_X emissions are dependent on the nitrogen content in the fuel, as well as characteristics of the combustion environment, such as temperature and stoichiometry. The combustion environment is important because of the available nitrogen content in air. The production of NO_X can therefore be altered by manipulations to the combustion environment, for a wide range of fuels.

Great concern exists over the pollutants produced from the combustion of fossil fuels and their adverse effects on the atmosphere [Prather and Logan, 1994]. The extent of global warming, ozone layer depletion, photochemical smog formation, haze, acid rain and related respiratory health problems have all increased since the industrial

revolution [Davis and Cornwell, 1998]. The release of CO_2 from the combustion of fossil fuels, in particular coal, is widely accepted as a primary cause of global warming [IPCC, 2007]. It is predicted that there will be a global average temperature rise of up to 4° by the year 2100. The possible consequences of such a temperature rise include rising sea levels from between 0.5m and 2m, reduced rainfall over land areas, increased droughts, and increased intensity and frequency of cyclones.

The reaction of NO_X with water vapour in the atmosphere can produce acid rain, causing damage to mineral and vegetable matter, such as buildings, forests and crops. The contribution of anthropogenic NO_X to acidity in rain has been estimated to be 25-30% [Bowman, 1992]. It has the rate limiting role in photochemical smog production, which leads to respiratory problems and eye irritation. Furthermore, NO_X is classified as a greenhouse gas. Coal combustion has been reported to produce as much as 30% of the global NO_X emissions [Fulkerson et al., 1990]. The detrimental effects of NO_X emissions have resulted in the implementation of legislation in most industrialised countries to regulate and limit total production of NO_X [Bowman, 1992]. Although cement production accounts for only approximately 0.5% of the global anthropogenic NO_X [Deussner, 1995], the localised NO_X emissions from cement kilns are high and can produce damaging effects to the local environment.

Despite the clear detrimental effects that fossil fuel combustion has on the environment, there is still a increase in energy requirements that results from the increasing human population. Due to the high availability and relative cheapness of fossil fuels compared with renewable energy, it is evident that fossil fuel combustion, and specifically coal combustion, will continue to be the major source of global energy for the foreseeable future. It is therefore imperative to provide means to improve coal combustion to minimise the harmful emissions produced. The production of CO_2 relates directly to the carbon content in the fuel and the rate of fuel consumption. The production of NO_X is based not only on the fuel composition, but also the combustion environment, and therefore air / fuel mixing. Minimising the rate of consumption of fossil fuels will

result in the reduction of both CO_2 and NO_X, but optimising the mixing of fuel and air can provide further reductions to NO_X.

Reducing anthropogenic NO_X emissions from fossil fuel combustion is a high priority [Dunsome, 1995, McQueen et al., 1995]. Previous studies into reducing NO_X emissions from gas flames in rotary kilns have resulted in the development of various burner design modifications. These low-NO_X burners utilise devices to modify near-burner aerodynamics to reduce the amount of NO_X produced. However, their success has been limited by the simultaneous increase in harmful carbon monoxide, CO, emissions, and impairment of the heat flux profile to the charge, thereby lowering product quality [Mullinger, 1994]. Despite the extensive use of, and research conducted into, rotary kilns, they still require further optimisation. Furthermore, rotary kilns are inefficient. It is evident that further improvements in emissions control and energy consumption are required [Turns, 2000]. Optimised burner designs are needed to produce high quality clinker with minimal fuel consumption or harmful emission production.

1.2 The Precessing Jet

Studies undertaken by researchers at The University of Adelaide have resulted in the design and commercialisation of the Precessing Jet (PJ) nozzle. The flows from PJ nozzles have been studied over the last couple of decades because of the beneficial influences on mixing they offer in some applications [Nathan et al., 1992, Schneider et al., 1997b, Smith et al., 1998b, Wong et al., 2003].

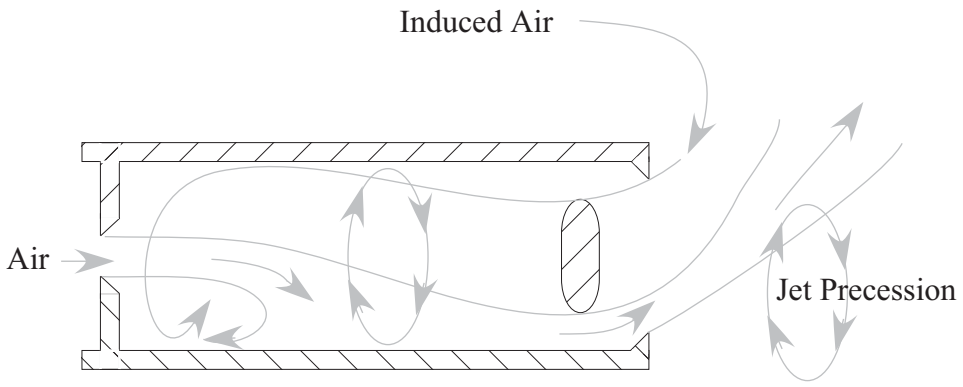

Figure 1.2: A schematic diagram of the Precessing Jet nozzle.

The PJ nozzle is shown in Figure 1.2. It consists of a large sudden expansion, a chamber, a small exit lip and a centrebody located slightly upstream of the lip. Fluid enters the chamber via the sudden expansion. If the inlet flow Reynolds number is sufficiently large ($Re_{inlet} \gtrsim$ 20,000), the dominant flow mode is an asymmetrically reattaching flow that precesses naturally about the nozzle axis due to a naturally occurring flow instability [Nathan et al., 1998]. The flow emerges from the nozzle without filling the entire exit plane, and continues to precess in the near external field [Wong et al., 2003]. Due to the small lip at the exit plane, the flow exits at a deflection angle of about 45^o to the nozzle axis. The unsteady flow results in a rapid initial jet spread, where the initial entrainment of ambient fluid is enhanced by up to a factor of five relative to a simple jet [Nathan and Luxton, 1991, Nathan et al., 1998]. However,

entrainment is restricted within the nozzle chamber and the far-field rates of spread and decay are comparable with that of a simple jet [Nathan et al., 2006]. The exiting jet flow from the Precessing Jet nozzle generates large-scale mixing, so that the scale of the dominant fluid structures is significantly larger than those in a simple jet [Hill et al., 1992, Nathan et al., 1998].

The flows from PJ nozzles can be beneficial in natural gas-fired rotary cement kilns, as they can provide a $40 - 60\%$ reduction in NO_X emissions [Nathan et al., 1995], while also improving product quality and fuel savings by typically $4 - 8\%$. Product quality is increased by maximising the clinker cooling rate [Ono, 1980]. An increased clinker cooling rate is achieved by translating the peak release closer to the burner. The full-scale measurements from Nathan et al. [1995] are consistent with the pilot-scale measurements from Parham et al. [2000]. Nathan et al. [1995] measured a 4% increase in radiant heat transfer and inferred a 30% reduction in NO_X emissions relative to a high momentum jet flame with a Craya-Curtet number of 2.7. The results are also consistent with trends in laboratory scale flames, which show that the radial initial spread leads to decreased global mixing rates, increased presence of soot, increased radiation and decreased thermal NO_X emissions [Nathan et al., 2006].

The difference between single- and two-phase flows are significant, and discussed in Section 1.4. Nevertheless, the PJ nozzle has also shown benefits in pulverised coal fired rotary cement kilns [Smith et al., 1998a, Megalos et al., 2001, Smith et al., 2002]. Using data from a PF fired rotary kiln simulator, Smith et al. [1998a] reported that for PF flames, the PJ nozzle aerodynamics produce a 60% reduction in NO_X emissions, a 50% reduction in ignition distance, and increased heat transfer from the near-burner region to the kiln walls. By using a precessing air jet to alter coal particle trajectories, Smith et al. [1998a,b] reduced the ignition distance four-fold, thereby improving flame stabilisation. Nathan and Hill [2001, 2002] determined that the PJ nozzle provided a 20-30% reduction in NO_X emissions and a 5% increase in fuel efficiency in a short-term trial at Ash Grove Cement. Full scale tests have also shown that altered heat flux

profiles, similar to those found in experimental PJ flames, cause an improvement in cement product quality [Nathan and Hill, 2001]. For the cement industry these trends translate to improved control of emissions, increased flame stability and higher fuel efficiency respectively [Smith et al., 1997, 1998a,b, Nathan et al., 2000].

The fundamental understanding of how PJ flows can influence the mean and instantaneous distribution of particles and by which PJ flow may enhance the formation of high localised particle concentrations, remains poorly understood. No detailed measurements of the influence of jet precession on the mean or instantaneous particle distribution have been published.

The general aim of the current research is to address the gap of knowledge relating to the influence of jet precession on particle distributions and the formation of high localised particle concentrations. The knowledge gained for the current research is focused towards the industrial requirement of optimising PF fired rotary cement kilns for cement product quality and to reducing harmful emissions production.

1.3 Combustion of particles in suspension

The understanding of gas combustion cannot necessarily be applied directly to PF combustion. Gore and Crowe [1989] reported that the interactions between solid particles and gases have a dominating influence on the transfer of heat and mass in combusting flows. Furthermore, it is known that the combustion of PF is directly affected by the dispersion rate of particles [Longmire and Eaton, 1992]. To further develop the understanding of fluid mechanics of particle-laden jets for applications into PF fired combustion systems, it is necessary to review combustion in relation to fuel-particle distribution. In this section the combustion process of pulverised coal and the effects of particle dispersion on coal combustion are briefly discussed.

The mechanisms for the production of flames fueled by solid particles and those fueled by gases are both very complex, but significantly different. Gas combustion, the simpler of the two processes, involves the fuel and air mixture heating up to the ignition temperature and then igniting. The ignition of coal particles can occur by either two mechanisms [Essenhigh et al., 1989]. When coal particles heat up, they can undergo a process known as devolatilisation [Williams et al., 1997]. In this process the volatile gases evolve from the coal particle. If ignition occurs with the volatile gases it is known as homogeneous combustion. However, if combustion occur directly with the solid particle, it is known as heterogeneous combustion. These two mechanisms are not mutually exclusive, and for any given particle the combustion process can alter between the two. For either mechanism, the remaining mineral matter transforms into ash, slag or fine particulate fumes [Turns, 2000].

Results from investigations into single particle combustion have shown that smaller particles ($d_p \lesssim 100\mu$m) tend to experience heterogeneous ignition, while larger particles ignite homogeneously [Costa et al., 1994]. There is also evidence that particles that heat slowly (< 100°C/s) will also undergo homogenous ignition, while particles that are heated at a faster rate experience heterogeneous ignition [Essenhigh et al., 1989].

Not only are particle size and heating rates factors in combustion, but coal volatile matter and ambient conditions are also factors that influence the type of ignition [Du et al., 1995]. However, in full scale kilns, where high mass loading of coal results in significant particle interactions, particles must be considered collectively and not individually [Ryan and Annamalai, 1991]. The combustion of particle clusters can not be accurately treated as an extension of single particle combustion [Cassel and Leibman, 1958]. Furthermore, Abbas et al. [1993], who investigated the effects of coal particle size on NO formation, found that nonuniform particle distributions have a strong effect on burner performance.

Cassel and Leibman [1958] compared ignition temperatures (based on the ambient temperatures) for single particles and monodispersed clouds of particles (clusters) at various concentrations. They determined that for a single particle, decreasing particle size generally results in an increase in ignition temperature. However, for multiple particles at high enough concentrations, the ignition temperatures of fine particles are lower than those of coarser particles. Depending of concentration, the ignition temperature of particle clusters is lower than that of the corresponding single particle. Quantitatively, they found that ignition temperatures drop by 50 - 300 K for particle clusters, relative to single particles; the drop in ignition temperatures is greatest for fine particles. Cassel and Leibman [1958] theorised that less heat loss occurs for particles close together than for isolated particles. Higher density clouds have a higher total heat generating area, lower particle heat loss and therefore require lower ignition temperatures.

Zhang and Wall [1993] analysed ignition of coal clusters for varying particle sizes and feed rates, as well as varying cluster sizes. For high particle feed rates, they determined that ignition temperature only depends on cluster size or density and not on particle size. Increasing the particle size results in a decrease in ignition temperatures, but only for low feed rates. They also show that ignition temperatures for dense clusters decrease as the cluster density or size increases. Ryan and Annamalai [1991] presented

results from a simple group combustion model. They determined that the concentration of a cluster will dictate the combustion mechanism that occurs. Dilute clusters will experience heterogeneous combustion, while dense clusters experience homogeneous combustion.

The formation of clusters of pulverised coal particles in experimental flames have been correlated with the reduction in NO_X emissions, ignition distance and increase heat transfer shown by Smith et al. [1998a] using jet precession, as discussed in Section 1.2. The formation of these clusters can be enhanced using a PJ burner [Nathan et al., 2000]. The fluid mechanics of particle clustering is discussed in Section 1.5.

From the above, it is evident that the understanding of the combustion of a single particle can not be directly applied to industrial scale burners. The distribution of all fuel particles needs to be considered collectively, and not simply as a uniform distribution, but as nonuniform distributions. It is clear that manipulation of the distribution of particles can be used to influence the combustion environment and it is the distribution of particles that is of interest in the current research. It should be noted that from Zhang and Wall [1993], the size distribution of particles, which can influence combustion for low particle loading, does not significantly influence the combustion for cases where the particle loading is high, such as those experienced in rotary cement kilns. However, as the particle distribution spreads in a jet, the local mass loading ratio decreases and the influence of particle size distribution may become more significant.

1.4 Two-phase particle-laden jet flows

The addition of solid-particles into a jet flow can have pronounced effects on the flow [DiGiacinto et al., 1982]. Particles are an additional source of momentum that can be transfered to and from the fluid phase. This transfer can influence the overall flow properties, so that knowledge of a single-phase jet flow can not necessarily applied to particle-laden flows. The motion of particles in jet flows is still relatively unexplored and poorly understood [Hishida et al., 1992, Longmire and Eaton, 1992]. The current section provides a review of literature relating to particle-laden jet flows, with specific focus towards particle distributions and concentrations.

1.4.1 Governing parameters

The motion of a spherical particle of diameter d_p, density ρ_p, and mass m_p in suspension can be described by Newton's second law,

$$F_p = m_p a_{slip} = \frac{1}{6}\pi d_p^3 \rho_p \frac{du_{slip}}{dt}, \tag{1.1}$$

where a_{slip} and u_{slip} are the acceleration and velocity of the particle relative to the fluid. If $\rho_p \gg \rho_f$, where ρ_f is the density of the carrier fluid, and the concentration of particles is low then all forces other than drag force, F_D, can be neglected [Crowe et al., 1998].

The drag force on a spherical particle is given by,

$$F_D = \frac{C_D A_p \rho_f |u_{slip}|^2}{2}, \tag{1.2}$$

where A_p is the projected area of the particle and C_D is the coefficient of drag. The term C_D can be determined from Stokes' Law as

$$C_D = \frac{24}{Re_p}, \tag{1.3}$$

for $Re_p < 0.1$ where

$$Re_p = \frac{\rho_f d_p |u_{slip}|}{\mu}, \tag{1.4}$$

and μ is the fluid viscosity.

By substituting Equations 1.3 and 1.2 into Equation 1.1 and rearranging, the equation for the motion of a spherical particle with $Re_P < 0.1$ is

$$\frac{du_{slip}}{dt} = -\frac{18\mu}{d_p^2 \rho_p} |u_{slip}|. \tag{1.5}$$

The general solution for this equation is

$$u_{slip} = C \exp\left(-\frac{t}{\tau_p}\right), \tag{1.6}$$

where C is a constant and τ_p is determined by

$$\tau_p = \frac{d_p^2 \rho_p}{18\mu}. \tag{1.7}$$

For the limiting case of $u_p = 0$ for $t = 0$ the solution then becomes

$$u_p = u_f \left[1 - \exp\left(-\frac{t}{\tau_p}\right)\right]. \tag{1.8}$$

The term τ_p is known as the *particle time scale*, *particle relaxation time* or *particle response time*. For the current work it will be referred to as the particle response time. From Equation 1.8 it can be seen that τ_p is the time it takes for a particle to accelerate from rest to 63% of the fluid velocity. However, in most flows of interest, the limiting case of $u_p = 0$ for $t = 0$ is not necessarily applicable. It it therefore common practice to compare τ_p to the fluid time scale, τ_f to produce the non-dimensional Stokes number,

$$Sk = \frac{\tau_p}{\tau_f}. \tag{1.9}$$

The fluid time scale is typically equated as

$$\tau_f = \frac{L}{U}, \tag{1.10}$$

where L is the characteristic length of the flow and U is the characteristic fluid velocity.

The response of particles in a flow can be characterised by Sk. It has been shown that there are three dominant regimes of particle response to a flow, characterised by three regions of Stokes number, $Sk \ll 1$, $Sk \simeq 1$, and $Sk \gg 1$ [Levy and Lockwood, 1981, Crowe, 1982, Hardalupas et al., 1989, Squires and Eaton, 1990, Longmire and Eaton, 1992, Wylie and Koch, 2000]. A particle with $Sk \ll 1$ responds to most flow fluctuations. A particle with $Sk \gg 1$ is generally unresponsive to the motions of the flow. A particle with $Sk \simeq 1$ will respond strongly to large flow fluctuations, but it will have enough inertia to be unaffected by the smallest scales of turbulence.

Care must be taken with the estimation of Sk, specifically with L. For turbulent flows there are four characteristic length scales frequently cited in literature [Turns, 2000]; three of these four length scale have been used to calculate Sk in literature. In increasing order of size, these four turbulent length scales are:

- The Kolmogorov length scale, λ_K;
- The Taylor micro-scale, λ_T;
- The integral-length / Taylor macro-scale, λ_I; and
- The characteristic width of flow / macro-scale, λ_M.

Hagiwara et al. [2002] provides other possible definitions of length scales. Although these are specific to their investigations, and therefore not discussed here in detail, they do highlight the numerous means of assessing the response of particles to fluid flow. Unfortunately, because of the wide range of actual length and time scales in a given flow, the proper choices can be ambiguous [Aggarwal, 1993]. The "appropriate" selection of L is thus typically based on the length scales of interest.

Smith [2000] and Nathan et al. [2000] conducted investigations of a particle-laden Precessing Jet nozzle. Their nozzle consisted of a central PJ nozzle, with a particle-laden co-annular jet. There was also a co-flow surrounding the nozzle. To determine Sk they used a characteristic length scale, L of three times the nozzle chamber diameter, D_{PJ}, as it corresponds well with the large scale structures in the near-nozzle region downstream from this nozzle. To calculate the characteristic fluid velocity, U, they incorporated the influence of central and co-annular jets with a surrounding co-flow. This velocity is calculated using a momentum weighted mean of the total velocities,

$$U_{total} = \frac{u_1 G_1 + u_2 G_2 + u_3 G_3}{G_1 + G_2 + G_3}, \tag{1.11}$$

where u and G are velocity and momentum flux respectively. The subscripts 1, 2, and 3 represent the central, annular and co-flows. The momentum flux of a jet, G, is given as

$$G = \frac{\dot{m}^2}{A\rho}, \tag{1.12}$$

where $\dot{m}$ is the mass flow rate of the fluid, ρ is the density of the flow and A is the cross sectional area.

However, the addition of particles to the co-annular stream will increase the momentum of that stream. The momentum flux of the co-annular stream with particles is then calculated by

$$G = G_f + G_p = \frac{\dot{m}_f}{A\rho_f} + \frac{\dot{m}_p}{A\rho_p}, \tag{1.13}$$

where subscripts f and p designate fluid and particles respectively.

Furthermore, the area of the exit flow from a PJ nozzle is approximately one third of the area between the centrebody and wall (see Figure 1.2). Therefore the momentum flux from the PJ nozzle is approximated as

$$G_{PJ} = \frac{12\dot{m}_{PJ}^2}{\pi\rho(D_{PJ}^2 - (0.79D_{PJ})^2)}, \tag{1.14}$$

where $\dot{m}_{PJ}$ is the mass flow rate through the PJ and D_{PJ} is the chamber diameter of the PJ nozzle. The ratio of PJ to co-annular momentum can then be determined using Equations 1.13 and 1.14.

Based on the equations from Smith [2000] and Nathan et al. [2000] for the current work

$$\tau_f = \frac{3D_{PJ}}{U_{total}}, \tag{1.15}$$

and therefore

$$Sk = \frac{d_p^2 \rho_p U_{total}}{54\mu D_{PJ}}. \tag{1.16}$$

It is generally agreed that, in addition to Sk, [Aggarwal, 1993], the particle mass loading ratio, β, also governs particle behaviour [DiGiacinto et al., 1982, Modarress et al., 1984a]. The definition for β, given by DiGiacinto et al. [1982], is the ratio of solid-phase mass to gaseous-phase mass per unit volume of suspension,

$$\beta = \frac{\dot{m}_p}{\dot{m}_f}. \tag{1.17}$$

The corresponding volume loading ratio, ϕ, can be determined from the equation

$$\phi = \frac{\dot{V}_p}{\dot{V}_f}, \tag{1.18}$$

where $\dot{V}$ is the volume flow rate.

For very low ϕ, the influence of the particles on the flow is negligible. Only the influence of the flow on the particles needs consideration. This situation is termed *one-way coupling*. These flows occur for $\phi \leq 10^{-6}$. With sufficient ϕ, the influence of particles

on the flow cannot be neglected: The flow influences the particles and the particles influences the flow. This situation is known as *two-way coupling* [DiGiacinto et al., 1982, Kulick et al., 1994] and occur for $10^{-6} \leq \phi \leq 10^{-3}$. For most two-phase flow studies presented in literature, including the current study, ϕ is sufficiently high to generate a two-way coupling situation. A third classification of coupling was investigated by Geiss et al. [2003]. *Four-way coupling* occurs when the particle-particle interactions are significant, which is typically for $\phi \geq 10^{-3}$.

It should be noted that in jet flows, the time average local value of β (and therefore ϕ) decrease with axial distance from the nozzle as the jet mixes with the surrounding fluid. Therefore, the effects of β on the flow are greatest in the near field.

1.4.2 Jet and channel flows

The majority of investigations into the motion of particles in particle-laden jets have used round jets. However, the fundamental results of particle motion are also clear in other flows such as co-annular jet flows, channel flows and shear mixing layers. Table 1.1 provides a summary of the experimental conditions, techniques and data collected from selected literature, for particle-laden round jets. Table 1.2 presents conditions for selected research with particle-laden co-annular jets. It should be noted that these investigations predominantly provide velocity data, although some also provide data relating to particle distributions and concentrations. The data reported from these studies are typically the mean and standard deviation. Very few provide instantaneous data. Instantaneous results are reviewed in Section 1.5

The effect of particles on the jet spread, concentration distribution and diffusion can be substantial [Hardalupas et al., 1989, Chein and Chung, 1987]. The addition of particles can influence fluid turbulence kinetic energy and energy dissipation rates [Mostafa and Mongia, 1988, Kulick et al., 1994, Fessler and Eaton, 1999]. Subsequently, the

turbulence kinetic energy of two-phase systems can influence the spreading rate of, and turbulence in, a jet [Levy and Lockwood, 1981].

Wall et al. [1982] experimentally investigated the spread, mixing and entrainment of clean and particle-laden round jets up to ten diameters from the nozzle. From their results they determined that the length scales, momentum thickness, vorticity thickness and both radial spread of the shear layers of the jet and of the potential core all increase linearly with axial distance, for all particle diameters and mass flow rates investigated, as well as clean jets. However, the increase in these gradients varied with changes in d_p and β. Specifically, they found that increasing particle size range from $20 \leq d_p \leq 45\mu$m to $150 \leq d_p \leq 180\mu$m results in a decrease in jet spread and decrease in length of the potential core. Increasing d_p has also be shown to reduce particle dispersion by Hishida et al. [1992] in shear flows, Fan et al. [1990, 1996b] in co-annular flows, and Pothos and Longmire [2002] in channel flows. These findings can be explained by results from Al Taweel and Landau [1977].

Al Taweel and Landau [1977] produced a model to predict the influence of particles on the turbulence of two-phase jets. They show that particles do not completely follow the turbulent fluctuations of the flow. They also show that the shear between the relative velocities results in a dissipation of turbulent intensity and a corresponding increase in particle kinetic energy. In jet flows, the model of Al Taweel and Landau [1977] indicates that turbulent kinetic energy is directly linked to the spreading rate of the jet. A dissipation of energy therefore results in a suppression of the jet spread. Gore and Crowe [1989] state that large particles create turbulence in their wake and thus increase turbulent intensity of the gas. Therefore turbulent kinetic energy from the particles is transfer to the flow, increasing the turbulent intensities of the gas. Wall et al. [1982] show that small particles have a greater spread than the larger particles. This is because the small particles follow the turbulent fluctuations closer than the larger particles causing less energy dissipation and thus greater the jet spread. Similar findings were also presented in simple jets by Hishida et al. [1985], Tsuji et al. [1988]

and Aggarwal [1993]; co-annular jets by Fan et al. [1992, 1996a,b] and Wicker and Eaton [2001]; and channel flows by Pothos and Longmire [2002] and Lain et al. [2003].

The above results indicate that there is an intermediate value of d_p that causes the maximum spread of particles. Gore and Crowe [1989] used the ratio of d_p to integral length scale, λ_I, as a criterion whether the particles will dissipate or produce turbulent kinetic energy, and there have maximum spread. They found that $d_p/\lambda_I < 0.1$ results in energy dissipation and $d_p/\lambda_I > 0.1$ energy production. Cui et al. [2006] suggest that the critical Stokes number is $88 < Sk < 157$ as the criterion.

Wall et al. [1982] found for a fixed particle size range, that increasing β results in a decrease in the jet spread and lengthening of the potential core. This was also found by Hedman and Smoot [1975]. Numerous authors have shown that particle-laden jets are narrower than their corresponding single-phase jets [Popper et al., 1974, Wall et al., 1982, Modarress et al., 1984a,b, Fan et al., 1992, 1996a, 1997].

Shuen et al. [1985] experimentally and numerically investigated turbulent, dilute, monodisperse, particle-laden jets injected into a still environment. The aim of their work was to assess computational models; however, they also reported that increasing β reduces the velocity decay rate of both phases. This was confirmed by Hardalupas et al. [1989] in simple jet flows. Hardalupas et al. [1989] also determined that an increase in β causes the initial velocity profile to become flatter. Their experimental conditions were similar to Levy and Lockwood [1981], except particle size is an order of magnitude smaller.

In a two-phase flow there is a transfer of momentum between the phases and accordingly the velocities of the phases can also be influenced by the addition of particles to the flow. Fleckhaus et al. [1987] stated that, due to particle inertia, the maximum obtainable particle velocity in a constant-velocity particle laden nozzle will always be lower than the maximum fluid velocity. Modarress et al. [1984a,b] reported no detectable difference

in the fluid velocity profile at the nozzle exit with the introduction of particles. Fan et al. [1992, 1996a,b] show that the velocity of the gas-phase at the nozzle exit is higher than the solid-phase, but further downstream the particle-velocity has the higher velocity of the two phases, a finding supported by Albagli and Levy [1990].

Exiting the nozzle, the velocities of both air and particles decrease, but the particle velocity decay rate is lower than the fluid velocity decay rate. Consequently the fluid velocity eventually decreases below that of the particles [Fleckhaus et al., 1987]. The centreline velocity decay rate decreases with increasing β, as shown by Shuen et al. [1985], Tsuji et al. [1988] and Zoltani and Bicen [1990]. However, Jou et al. [1993] found that β has little effect on the axial mean velocity at the jet nozzle exit, and their results show little variations within the first 10 diameters. The results from Sadr and Klewicki [2005] also show little variation in near field of a particle-laden co-annular jet.

The influence of β on both velocity and jet spread can be explained with the results from Mostafa and Mongia [1988]. They produced a mathematical model for turbulent two-phase flows, with the assumption that particles are sufficiently dispersed so that particle-particle interactions are negligible (i.e. two-way coupling, not four-way coupling). The model was applied to a round free jet laden with solid particles, and their results were validated with the data from Shuen et al. [1985]. The results from Mostafa and Mongia [1988] show that that increasing β results in a reduction in turbulent kinetic energy. As discussed above, the kinetic energy relates directly to the spread of the jet. As kinetic energy is proportional to the square of velocity, it is clear that a reduction in kinetic energy corresponds to a reduction in velocity. Furthermore, they show that momentum transfer is proportional to β. It follows that increasing β results in a decrease in velocity decay rates of both phases and a narrowing of jet spread, as the axial momentum is still higher. The findings of Mostafa and Mongia [1988] have been confirmed by numerous authors, including Popper et al. [1974], Levy and Lockwood [1981], Mostafa et al. [1989], Hetsroni [1989], Fan et al. [1990] and Kulick et al. [1994].

Although it is clear from the above that β has an influence on jet spread and velocities, this influence is minor relative to the influence of particle size. Levy and Lockwood [1981] found that β for a fixed particle size has only little influence on the jet spread. At the nozzle exit, Fan et al. [1990] also found that the influence of β is almost negligible. However, they showed that the particles at the edge of the jet are significantly small than those found along the centerline. This was determined by conducting experiments with silica gel particles with approximately 85% of particles, by weight, having a particle diameter of $30 \leq d_p \leq 160\mu$m.

The distribution of particles exiting a jet or channel has been investigated by Pothos and Longmire [2002] and Ayranci et al. [2007]. They show that as particles emerge from a jet / channel, they generally concentrate on the edge and subsequently, in the near field of the jet, the particles are still concentrated near to the jet edge.

A key notion from the findings of Fan et al. [1990] is that the distribution of particles may not be uniform, even for a steady jet. This is supported by Ayranci et al. [2007] who measured particle concentrations emerging from an upwards facing vertical air jet. Their work was focussed on improving the measurement technique and therefore they only present results from radial locations at $x/D = 1.2$. However, from their results it is evident that, at $x/D = 1.2$, an increase in particle (volume) flow rate results in an increase in the normalised particle concentration at the edge of the jet.

1.4.3 Summary

The governing dimensionless parameters for two-phase flows are Sk and β. As Sk is a function of d_p, and as Sk can be determined many different ways, it is understandable that most literature describes particle size in terms of d_p, rather than using Sk exclusively. The general findings from the above investigations can be summarised as follows: When particles at rest are introduced into a jet, they will have significantly

lower momentum and velocity compared to the carrier fluid. There is a transfer of momentum from the fluid to the particles, which will result in an increase in the velocity of the particles. However, as the driving flow rate is constant, there is no reduction in bulk fluid velocity resulting from the transfer of momentum. At the nozzle exit the maximum velocity of the particles will be lower than the maximum velocity of the fluid. Although the bulk fluid velocity in the nozzle and at the exit will not be changed by the addition of particles, increasing β will result in flatter particle velocity and concentration profiles. However, Fan et al. [1990] claims that small variations in β will have little influence on the particle distribution at the nozzle exit.

Downstream from the nozzle exit plane both gas-phase jets and particle-laden jets will spread linearly, but the spread will be influenced by d_p and β. Very small particles will result in a jet that is wider than a clean jet. Increasing particle size will result in a narrower jet, as well as a lengthening of the potential core. Similarly, increasing β will also result in a narrowing of the jet and lengthening of the potential core. For flows with a large range of particle sizes, the large particles will tend to have a narrower spread than smaller particles and so the particles on the edge of the jet are significantly smaller than flows with narrower particle size range.

Table 1.1: Experimental flow conditions from selected investigations of particle-laden simple jets

Author, year	D_{nozzle} [mm]	Re_{nozzle}	U_{exit} [m/s]	d_p [μm]	β [kg/kg]	Range [x/D_{nozzle}]	Data	Techniques
Laats and Frishman [1970]			29 - 60	17 32 49 72 80	0.3 0.77 1.4	2.5 - 30		
Popper et al. [1974]	25	10 000 - 100 000	10 - 30	≤ 50 †	*10^{-6}	10-29 (gas) 8 - 14 rad 0-20 axial	velocity	LDA and hot wire
Levy and Lockwood [1981]	15	20 000		180 - 250 300 - 500 380 - 700 600 - 850 850 - 1200	1.14 3.5	20	velocity	LDA
Wall et al. [1982]	24	26 000		20 - 45, 45 - 53, 53 - 75, 75 - 90, 90 - 105, 125 - 150, 150 - 180	0.22, 0.34, 0.50	1 - 10	concentration velocity	isokinetic sampling, impact tube, micro-manometer

* volume fraction # in water † oil droplets

NB values left blank were not originally report.

Author, year	D_{nozzle} [mm]	Re_{nozzle}	U_{exit} [m/s]	d_p [μm]	β [kg/kg]	Range $[x/D_{nozzle}]$	Data	Techniques
Tsuji et al. [1984]	30.5		8-20	200 - 3000	0 - 5		velocity	LDA
Modarress et al. [1984a,b]	20		10.2	200	0.8	0.1 - 30	concentration	LDA pulse
			12.6	50	0.32, 0.85			counting
Hishida et al. [1985]	13		30	64				
Shuen et al. [1985]	10.9		32.1	79 $\pm$18	0.2,	1- 50	velocity	LDA
				119 $\pm$19	0.66		concentration	isokinetic
				207$\pm$24				sampling
Nouri et al. [1987]	25.4			100 -	* 0.001-		velocity	LDA
		59 200	2.33	500	0.14			
		$^{\#}$39 650	$^{\#}$2.45					
Fleckhaus et al. [1987]	13	20 000	30	64,	0.3	10 - 30	velocity	LDA
				132			concentration	LDA pulse counting
Tsuji et al. [1988]	20		11	170	0.86	1 - 20	velocity	LDA pulse counting
			23	243	0.71		concentration	fiber optic probe
			24	1400	0.94			Pitot tube
Hardalupas et al. [1989]	15	13 000	11	40	< 0.80	1 - 28	velocity	PDA
				80	< 0.86			
				200	< 0.37			

* volume fraction $^{\#}$ in water † oil droplets

NB values left blank were not originally report.

Author, year	D_{nozzle} [mm]	Re_{nozzle}	U_{exit} [m/s]	d_p [μm]	β [kg/kg]	Range $[x/D_{nozzle}]$	Data	Techniques
Mostafa et al. [1989]	25.3		4.74	105	0.2 1.0	≤ 12	velocity	PDA
Zoltani and Bicen [1990]	25.4	29 000	17.7	60 - 95	0.015	1 - 9	particle and gas velocity	LDA
Fan et al. [1990]	42	40 179 53 571 66 964	15 20 25	18.5 - 261.6	0.21 0.30 0.48	1, 10, 20	concentration size	LDM
Jou et al. [1993]	15	20 000		180-240, 710-840	0 - 3.6	0 - 100	velocity	LDA
Sakakibara et al. [1996]	20	9300	7	55 86	3.2	0.0036	particle and gas velocity	PIV
Gillandt et al. [2001]	12	5700	7.7	110	1	12.5	velocity size	PDA
Cui et al. [2006]	20, 40	2500 - 13750		50 - 350	0.6	1 - 20	velocity	visualisation PIV PDPA
Ayranci et al. [2007]	6	1187 - 10 369		6.52 - 8.04	*2.0 - 13.0	1.2	velocity concentration	LDA pulse counting

* volume fraction # in water † oil droplets

NB values left blank were not originally report.

Table 1.2: Flow conditions from selected investigations of particle-laden co-annular jets

Author, year	D_1 [mm]	D_2 [mm]	Re_1	Re_2	U_1 [m/s]	U_2 [m/s]	d_p [μm]	Range [x/D_1]	β	Measurements	Techniques
Hedman and Smoot [1975]	25.4	127			273 -	30.8 -	6,	0 - 8	0.24	gas velocity particle concentration	Pitot static tube, isokinetic sampling
Albagli and Levy [1990]	14	103			42.5	22.5	20	0 - 23	β	particle and gas velocity gas (CO_2) concentration	LDV, isokinetic sampling
Fan et al. [1992, 1996a,b]	40	68			20	30 - 60	0 - 300	0 - 30	0 - 1.5	velocity, concentration	LDA, LDM
Wicker and Eaton [1999, 2001]	20	60	13 000		10	11.5	55, 90, 150	0 - 12		gas velocity concentration	hot-wire, particle counting
Sadr and Klewicki [2005]	30	75	#41000		1.39	0.19 - 1.51	210 - 250	0 - 6	*0.03 *0.06 *0.09	velocity	MTV

* volume fraction # in water † oil droplets

NB values left blank were not originally report.

1.5 Preferential concentration and particle clustering

A naturally occurring phenomenon in particle-laden jet flows is *preferential concentration*. Preferential concentration can result in the formation of regions of high localised particle concentrations, known as *particle clusters*. As discussed in Section 1.2, the enhancement of particle clusters has been correlated with improved combustion [Smith et al., 2002].

Squires and Eaton [1990] numerically investigated particle response in isotropic turbulence. They determined that the size of the particles influences the formation of particle clusters. Particles with $Sk \gg 1$ are insensitive to turbulent velocity fluctuations, whereas particles with $Sk \ll 1$ behave more like fluid elements. Both were found to exhibit less clustering than particles with $Sk \simeq 1$. For their work, Sk was calculated based on the longitudinal length scale, $q^2/3^{1/2}$, where q^2 is twice the turbulence kinetic energy. Kajishima and Takiguchi [2002] found similar results for Sk based on the initial state values in a numerical investigation into particle distributions of particles falling by gravity.

Longmire and Eaton [1992] assessed particle distributions in acoustically forced jets. They found that particles with $Sk \simeq 1$ preferentially concentrate in regions immediately downstream from vortex rings produced by the acoustic excitation. These regions corresponds to regions of high strain and low vorticity. Their calculation of Sk was based on the eddy length-scale and velocity-scale. Preferential concentration of particles with $Sk \simeq 1$ in regions of high strain and low vorticity is supported by Fessler et al. [1994] for particle at the centreline of a turbulent channel flows using the Kolmogorov time scale. Wark et al. [2000] also found similar results when investigating acoustic excitation of reacting liquid droplets from a vertically orientated round jet. They used the spacing between structures as the characteristic length scale to calculate Sk.

Wicker and Eaton [2001] investigated the particle motion in a co-axial swirling jet and found that particles are preferentially concentrated in the regions between the vortex rings, which correlates to regions of high strain and low vorticity. Hagiwara et al. [2002], who investigated particles settling in a horizontal duct, found that particles with $Sk \simeq 1$ preferentially concentrate inside recirculation zones.

There is also support from Wood et al. [2005] who investigated the concentration of particles subjected to homogeneous and isotropic turbulence. Using the Kolmogorov length scale to calculate Sk, they found the largest magnitude of preferential concentration occurs for particles with $Sk \simeq 1$.

The results from above literature all show that particle of $Sk \simeq 1$ preferentially concentrate in regions of high strain and low vorticity as a result of particles centrifuging away from vorticies. The only minor contradiction is from Winkler et al. [2004] who investigated preferential concentration of particles in a fully developed turbulent square duct flow using large eddy simulations. They found that these particles preferentially concentrate in vortex cores, which corresponds to regions of high strain and low swirling strength, rather than low vorticity.

In addition, there are a number of other postulated mechanisms that can cause the formation of particle clusters. From the numerical simulations of isotropic suspension of particles by Wylie and Koch [2000], two possible mechanisms for particle clustering were reported; microscopic clustering, which occurs at the length scale of individual particles, and macroscopic clustering. Microscopic clustering is suggested to occur due to hydrodynamic interactions between small groups of particles. Macroscopic clustering is postulated to result from the rate of viscous dissipation of the solid phase. However, Elperin et al. [1998], who investigated particle dynamics in fast rotating turbulent fluid flows, determined that particles preferentially concentrate at either boundaries or centers of turbulent eddies as a result of the [sic] Coriolis force. As the Coriolis force is limited to atmospheric scale flows, such as cyclones, and Elperin et al. [1998] conducted

experiments on a much smaller scale, it is suggested here that it is the centrifugal force of turbulent eddies that cause particles to preferentially concentrate at the very centre, or outside of, the eddies. Based on this reinterpretation, the mechanisms for the formation of particle clusters proposed by Elperin et al. [1998] is in support of previous findings.

Goldhirsch and Zanetti [1993] produced a theoretical analysis of high density clusters of inelastically colliding particles. They suggest inelastic collision between particles is the mechanism for preferential concentration. Wassen and Frank [2001] conducted simulations of cluster formation in gas-solid flows to investigate particle clustering. Their results also show that the formation of particle clusters is enhanced by collisions between particles. They focussed their investigation on inter-particle collisions during cluster formation and not phase-coupling. For low particle mass loading ratios, collisions tend to enhance particle dispersion, whereas for high particle mass loading ratios, collisions enhance the development of clusters.

Kajishima and Takiguchi [2002] investigated the two-way interaction between particles and fluid falling by gravity, using Direct Numerical Simulations (DNS). They simulated a homogeneous distribution of particles falling by gravity and assessed the formation of particle clusters. The mechanism of cluster formation due to the wake of other particles was presented and they also suggest that vortex shedding enhances clusters. However, they found that the fluid turbulence created by the formation of clusters results in the break-up of clusters.

Hagiwara et al. [2002] investigated the settling of particles, but experimentally and for particles in turbulent water flows. They found that the formation of particles cluster is related to regions of high strain rate and low vorticity, as have previous authors. However, when using τ_p to calculate Sk, they found that the particles that preferentially concentrate to form particle clusters have $Sk \ll 1$. They conclude that τ_p is an inappropriate characterisation of particle response in relation to cluster formation.

It is clear that there is still some uncertainty as to the mechanisms that preferentially concentrate particles to form clusters. Furthermore, although there is agreement by most authors who investigated particles in jet flows as to the basic mechanism [Eaton and Fessler, 1994], these findings may not necessarily relate to particles influenced by jet precession.

The desire to assess how jet precession can be used to enhance particle clusters results from the expected industrial applications of PF combustion. In industry, any use of acoustically excited burners is expected to raise occupational health and safety issues due to noise and the possible resonant frequency matching of the numerous interconnecting systems. Although acoustic excitation provides the possibility of enhancing the formation of particle clusters, they have not found much practical application. Precessing Jets are fluidically excited jets and have no moving parts and therefore do not suffer this same limitation [Smith et al., 1997].

The general consensus from literature is that the mechanisms for the enhancement of preferential concentration, and therefore increased probability of particle cluster formation, are particles with $Sk \simeq 1$ in regions of high strain and low vorticity. However, for PJ flows Smith [2000] suggests an alternative mechanism for enhanced preferential concentration and the existence of different types of clusters, although to date there is little quantitative supporting data.

Smith et al. [1998a,b] conducted experiments with a PJ nozzle with a co-annular particle laden stream and investigated particle clustering produced from large scale turbulent motion from jet precession. They found that large particles and small particles clustered in different regions of the flow. The clustering of the small particles ($St \ll 1$) occurs in the near burner region where, in single-phase flows, large scale structures are present due to the jet precession. The larger particles, ($St \gg 1$ and $St \simeq 1$) which are less sensitive to jet precession, cluster in the far field. Smith [1996] reported that for reacting two-phase flows, the Precessing Jet exhibits significant influence on par-

ticle trajectories, ignition distances and particle clustering. More recent work, using the same nozzle configuration, has shown that the larger size particle clusters can be produced with an increase in the ratio of PJ momentum to that of the particle laden stream [Nathan et al., 2000].

1.6 Summary

From the above review, it is evident that particle-laden flows are significantly different from single-phase flows, predominantly due to the momentum exchange between the phases in the flow. Similarly, the combustion of solid fuels and gas / liquid fuels are also different, not just in the chemical properties, but also in how the fuel is distributed in response to the flow fields. As a result, optimisation of PF burners requires specific knowledge of the fluid mechanics and combustion of particle-laden flows to understand how the fuel and air interact.

The combustion of PF is dependent on the mixing between the fuel and surrounding air. The mean and instantaneous distributions of fuel particles are important to the flame properties. There is evidence that the formation of particle clusters can be beneficial in certain applications, although, it is possible that they may also be detrimental in other applications. Enhancement of particle clustering has been correlated with reduced NO_X emissions and, in the cement industry, reduced fuel consumption and improved product quality. However, the fundamental understanding of the formation of particle clustering to provide a means of enhancing this phenomenon is not fully understood. To date, there is little data on the mean distribution of particles in the near-field of jet flows. There is also very little data on the instantaneous distribution of particles throughout the entire flow.

For jet flows, many authors agree that the preferential concentration of particles and the formation of particle clusters occurs when $Sk \approx 1$ in regions of high strain and low vorticity. However, great care is required in defining Sk, because there are numerous length scales in the flow and hence characteristic definitions that are used in the available scientific literature, and various methods to calculate them.

Jet precession has been shown to enhance preferential concentration and the formation of particle clusters. The enhancement of particle clusters has been correlated with

improved combustion and flames conducive to improved cement production. However, there is insufficient knowledge of the influence of jet precession on particle distributions for optimisation of burner design. This lack of knowledge is for both mean and instantaneous data.

There is no data relating to the influence of jet precession on the mean and instantaneous distributions of particles. Nonetheless, PJ flows can be used to improve PF fired combustion systems, but there is insufficient data, either qualitative and quantitative, to provide design guidelines. The major focus of the current research is to contribute to the body of knowledge relating to particle-laden PJ flows.

1.7 Thesis aims

The aim of the current research project is to increase the body of knowledge relating to the influence of jet precession on the distribution of particles. This will help enable improved designs of PJ nozzles for PF fired rotary cement kilns resulting in reduced harmful emissions and improve product quality. This general aim is broken down into specific objectives.

These specific objectives are as follows:

- To quantify the influence of jet precession, described by the ratio of jet to annular momenta (G_{PJ}/G_{ANN}) on the mean and fluctuating distribution of particles.
- To quantify the effect of particle mass loading, β, on the mean and fluctuating distribution of particles.
- To develop a method of identifying and quantifying particle clusters.
- To quantify the influence of G_{PJ}/G_{ANN} on the characteristics of particle clusters.
- To quantify the effect of β on the characteristics of particle clusters in Precessing Jet flows.

These objectives are addressed by physically modelling the near-burner region of a PF fired rotary cement kiln. A wind tunnel has been specifically designed and built for the purpose of simulating this region of flow. Particle selection has been conducted to provide $Sk < 1$ (based on Equation 1.16), as this is typical of industrial applications. A quantitative planar laser technique has been developed to measure distributions of particles. This technique enables investigations into flows with moderately high particle mass loadings where attenuation of light occurs. A method of identifying and characterising particle clusters is presented and used to provide statistical data on particle clusters.

An analysis of the data provides further understanding of particle-laden jet flows and the mechanisms of particle clustering produced by a Precessing Jet. This information should further enable enhanced particle clustering for industrial applications, such as rotary cement kilns.

1.8 Thesis outline

This thesis contains 10 chapters. Chapter 2 provide specifications of the equipment used for the experiments. The technique and corrections to determine the relative particle concentrations are outlined in Chapter 3. The wind tunnel, feeding system and particle concentration measurement technique have been designed and developed as part of, or in parallel with, the current research and are therefore discussed in-depth. Chapters 4 and 5 provide results and analysis of the influence of jet precession and particle mass loading respectively, on the mean and standard deviations of the particle distributions. The methodology used to identify particle clusters in the current research was developed as part of the research project and is detailed in Chapter 6. Chapters 7 and 8 present the results and analysis of the influence of jet precession and β on particle clusters respectively. Discussions of the results for chapters 4, 5, 7 and 8 are provided within each chapter. Chapter 9 presents a summary and conclusions of the current work, with scope for future work in the field given in Chapter 10.

Chapter 2

Equipment

2.1 Wind tunnel

Experiments were conducted in an open loop wind tunnel to simulate the near-nozzle region of a pulverised coal burner. The experiments were non-reacting and conducted at room-temperature, since it is necessary to understand the non-reacting flow before proceeding to a reacting case. However, the data are also directly relevant to the near-nozzle, pre-ignition region of a PF flame, where thermal gradients are small relative to the combustion zones [Smart, 1992].

The wind tunnel is vertically oriented to avoid gravity bias and has a square cross-section of 650 mm $\times$ 650 mm and a working section of 1500 mm length. The tunnel has a uniform co-flow of 8.0 ± 0.3 m/s, which is typical of the velocity in a rotary cement kiln. This flow is conditioned by a series of wire-mesh screens and a honeycomb section upstream from the working section. The honeycomb section, with a length to diameter ratio of 50:1, reduces irregularities in the flow direction [Lumley, 1964, Lumley and McMahon, 1967, Loehrke and Nagib, 1979]. The wire mesh screens range in mesh size

from 6 mesh per inch to 16 mesh per inch with spacings between screens set at 300 mm. Directly downstream from the working section is another wire-mesh screen. These screens increase velocity uniformity [Bradshaw and Pankhurst, 1964]. Due to space limitations, a smooth contraction to the tunnel working section was not incorporated. Further downstream is a cyclone separator, used to remove particulate matter from the exhaust air. The cyclone was designed in accordance with guidelines by Dirgo and Leith [1986]. The walls of the wind tunnel working section are constructed from 16 mm thick Perspex enabling the application of laser-based measurement techniques. Figure 2.1 shows the wind tunnel arrangement.

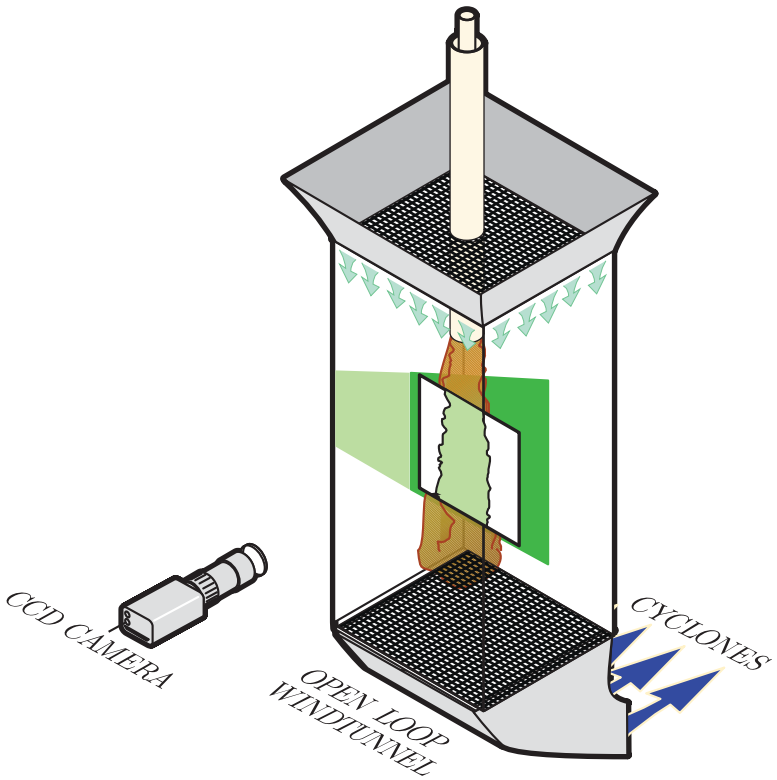

Figure 2.1: Layout of the wind tunnel.

2.2 Solid phase

Pulverised coal particles were simulated using hollow glass spheres (Q-Cel^{TM} 5070s). These particles have a specified density of $\rho_p = 700$ kg/m^3, which is about half that of coal. Figure 2.2(a) shows the solid phase particles under magnification. A Malvern Mastersizer 2000 was used to measure particle diameter distribution based on the ratio of particle volume to particle area, $d_{3,2}$. This was conducted with the particles in a water suspension. The laser diagnostic technique used for the current investigation detects light scattered under generalised Lorenz-Mie scattering, so the measured intensity is proportional to the total surface area of scattering bodies. The distribution results provided by the Malvern particle sizers are converted to surface-area weighted diameter, $d_{2,1}$, distributions in order to maintain consistency with the measurement technique.

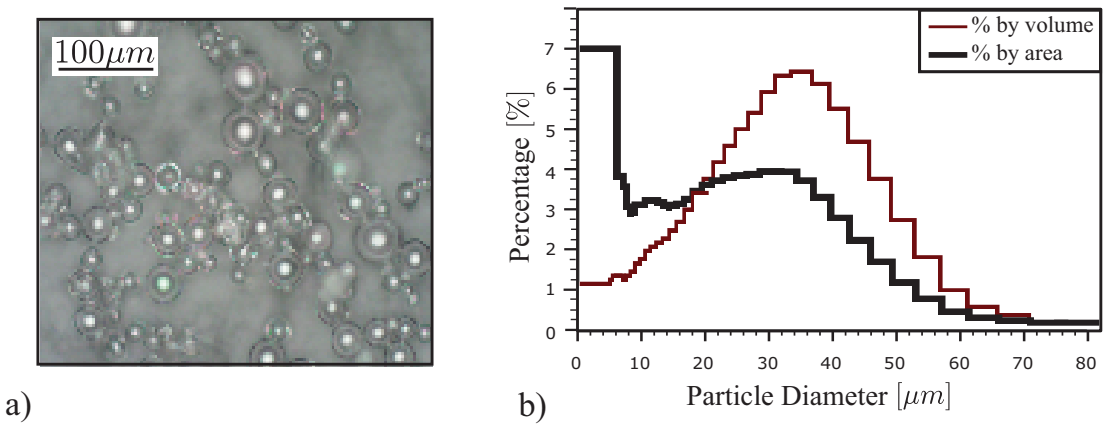

Figure 2.2: a) The 20 μm nominal diameter glass spheres used in the investigation under magnification. b) The size distribution of the particles, as measured by a Malvern-Particle Sizer.

The probability density function, PDF, of the distribution of $d_{3,2}$ and $d_{2,1}$ are shown in Figure 2.2(b). This indicates that 85% of particles have a diameter in the range of $7 \leq d_{2,1} \leq 50$ μm. This is broader than the manufacturer's specified range of 25-45 μm. The mean diameter of the distribution for the particles used in the current investigation was determined to be $d_{2,1} \simeq 20\mu$m. The particles have a range of $0.03 \leq Sk \leq 0.51$, and an average of $Sk \approx 0.08$, calculated using Equation 1.16 with $d_{2,1}$, length scale

$L = 3D_{PJ}$, and characteristic fluid velocity based on the momentum weighted mean U_{total}. An alternative calculation for Sk can be determined using $\tau_f = 1/f_p$ where f_p is the frequency of precession (see Section 2.6). Using this alternate mean, the the particles have $Sk \leq 0.2$. From both of these estimates, it is expected that most particles will follow the large-scale motions reasonably closely, but some departure may be evident with the largest particles.

Despite a large particle size distribution of the particles used, it is narrower than that used by Fan et al. [1990], and only slightly wider than that of Ayranci et al. [2007]. The range of particle sizes is similar to Hardalupas and Horender [2003] and significantly narrower than Geiss et al. [2003], although the mean diameter is much smaller for the current work. The particle mass loading ratio, β, was varied from 0.041 to 0.461. For the cases with fixed particle mass loading, $\beta = 0.14 \pm 0.02$.

2.3 Feeder

The solid phase is introduced into the nozzle using a fluidised bed feeder. The feeder is a sealed vertical cylinder with an internal diameter of 120 mm and height of 490 mm. Regulated compressed air enters the base of the feeder and is passed through a sintered plate to fluidise the particles. The particles and fluidising air exit via three 2 mm holes drilled into a horizontal pipe located pipe located approximately 20 mm from the base of the fluidised bed. From the exit pipe, the fluidising air and particles travel to the low-pressure inlet of a venturi and then to the manifold of the nozzle.

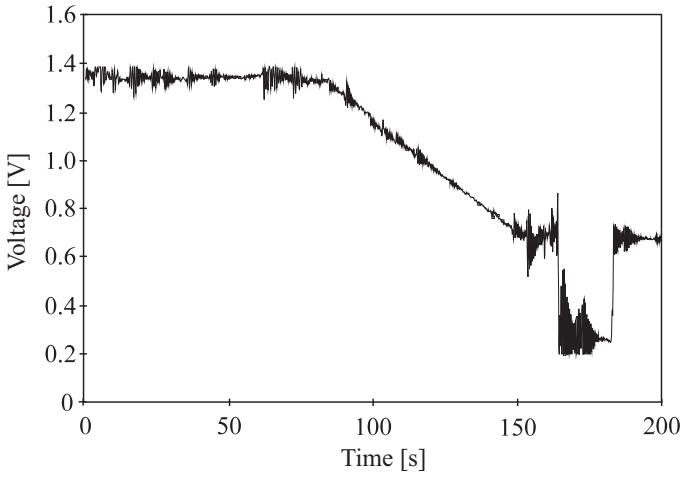

Figure 2.3: Example of the loadcell output.

Particle mass flow rates were adjusted using a small clamp to vary the cross-sectional area of the hose downstream from the feeder. Mass loadings were determined by the change in mass of the feeder, as measured by a load cell, for the duration of the experimental runs. Calibration of the feeder was conducted for each experimental run using a 100 g weight. Figure 2.3 presents an example of the output produced by the load cell. The calibration from a 100 g weight can be clearly seen as a change in voltage of approximately 0.5 V. The profile from approximately 80 ms to 150 ms is typical of the linear profile obtained during the experiments. The calculation of the mass flow rate during experiments was determined from the gradient of the profile.

2.4 Nozzle

The nozzle used for the current research consists of a central Precessing Jet nozzle, with a co-annular nozzle. The nozzle configuration is shown schematically in Figure 2.4. Upstream from the PJ chamber is a 1500 mm long, 50 mm internal diameter pipe. At the end of this pipe is a smooth contraction to a 10 mm diameter inlet, d_1, into the PJ chamber. The PJ chamber has an internal diameter, D_{PJ}, of 50 mm and length, L_{PJ}, of 140 mm. A 45 degree contraction at the end of the PJ chamber creates an exit diameter, d_2, of 40 mm. A center body, used to reduce the probability of axial jet mode, has a diameter of 35 mm, thickness of 10 mm and rounded edges. The front edge of the centre body is located 12 mm upstream from the nozzle exit plane. The dimensions were selected based on the recommendations of Wong et al. [2003]. The co-annular nozzle has inner diameters of $d_{in} = 60$ mm and outer diameter $d_{out} = 70$ mm. The total length of 1700 mm, which equates to over 340 gap-widths. The co-annular gap is consistently 5 mm, with care taken to minimise asymmetry.

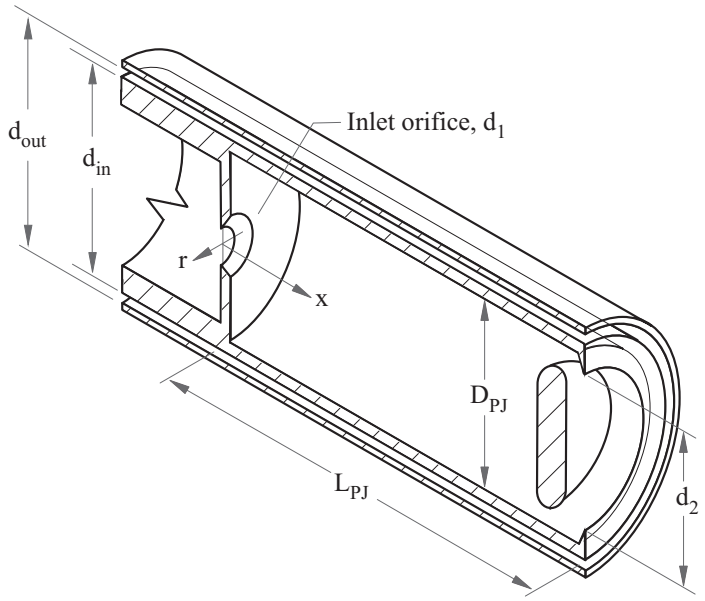

Figure 2.4: Schematic diagram of the nozzle.

Solid particles are conveyed through the co-annular jet, rather than through the PJ

nozzle itself to prevent erosion of the PJ internal components. This configuration is similar to that employed at Ash Grove Cement, Durkee, Oregon [Nathan and Hill, 2001]. Particles from the feeder enter the manifold via the venturi ejector with the conveying air.

2.5 Experimental arrangement

The experimental configuration is shown in Figure 2.5. A Quantel Twins B Nd:YAG laser was used, frequency doubled to provide visible light at 532 nm, with pulse duration of 10 ns and pulse frequency of 10 Hz. The laser power was fixed. The optics train consisted of two 45 degree mirrors, an iris to clean the beam profile, a combination of ± 100 mm cylindrical lens pairs and a -25 mm cylindrical lens. The optical train produced a vertical sheet less than 2 mm thick. A Kodak Megaplus ES 1.0 CCD with Fujinon TV H6 ×12.5R1:1.2/12.5-75 lens was aligned perpendicular to the laser sheet to prevent the need for optical distortion corrections in the post processing of data. A horizontally polarised lens was attached to the front of the camera lens. This filter was used to reduce the signal from multiple scatterings out-of-plane which depolarise the scattered light. The camera lens was set with f# 4 for the experiments. The image array is 1008 pixels × 1018 pixels, which corresponds to approximately 509 mm × 514 mm (504 μm per pixel resolution). Images were collected using Epix V2 software on an AMD computer. Experiments typically yielded 202 images with 10 bit resolution for each case. Data was saved as 16 bit images with prefix 0 bits and processed using open source OMA image processing [Kalt and Long, 2008]. The technique used to measure particle distribution, known as *planar nephelometry*, is discussed in Chapter 3.

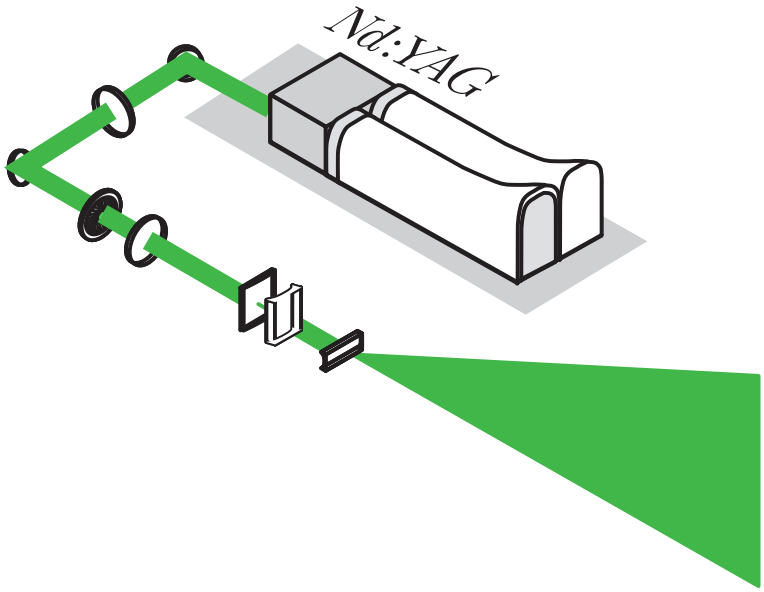

Figure 2.5: Layout of the laser and optics.

2.6 Flow parameters

Filtered and compressed air was supplied through both the annular and central jets. For the investigation into the influence of G_{PJ}/G_{ANN} on the distribution of particles, the velocity at the PJ inlet was varied over the range $0 \leq U_1 \leq 287$ ms^{-1}. This gives a Reynolds number range, based on d_1 (Figure 1), of $Re_{PJ} \leq 188,500$. Based on Nathan et al. [1998], the frequency of precession, f_p, was estimated to be $7Hz$ based on $U_1 = 287$ ms^{-1}. The annular velocity $U_{ANN} = 18$ ms^{-1} was not varied. The Reynolds number based on the annular gap is $Re_{ANN} = 5900$. A constant value of $\beta = 0.14 \pm 0.021$ was used. Details of the experimental conditions are summarised in Tables 4.1 and 5.1.

Chapter 3

Measurement techniques

3.1 Existing techniques

Previous measurements of particle concentrations in particle-laden jets have typically been restricted to single point techniques. Single point measurements can provide good statistical data, but are unable to provide instantaneous planar information as is needed to assess flow structures. As discussed in Section 1.3, the instantaneous distribution of particles is an important factor for combustion related applications and therefore planar (or even volumetric) data are desirable.

Tables 1.1 and 1.2 provide details of experimental configurations selected from previous publications. Wall et al. [1982] conducted particle concentration measurements using isokinetic sampling, which is a time-averaged, single point, intrusive technique. For this technique a probe is inserted into the flow. For a known time interval, particles are extracted from the flow at a velocity rate equal to the local mean flow velocity. These particles are collected and weighed to provide a particle mass per unit time measurement, per probe cross sectional area. This technique is quite limited because

it is not capable of providing instantaneous particle concentration data of a flow, is a single point technique with poor spatial resolution, and is intrusive, therefore possibly altering the flows investigated. Isokinetic sampling has also been used by Laats and Frishman [1970] and Shuen et al. [1985].

Laser Doppler anemometry, LDA, (also known as laser Doppler velocimetry, LDV) is a non-intrusive, single point laser based technique that is used to measure the velocity of particles in a flow. Typically, two collimated, monochromatic, coherent light beams intersect at a point in the flow. Due to constructive and deconstructive interference of the two beams, a series of straight fringes, with known fringe spacing, are generated at this point. A photomultiplier is configured to record scattered light from the point of intersection. As a particle passes through the fringes, it will scatter light, but only when there is constructive interference. The photomultiplier will receive a series of pulsed signals as a particle passes each fringe. The velocity of the particle is determined from frequency of these pulses multiplied by the spacing of the fringes.

Particle number densities can be determined by counting the number of pulses recorded on the photomultiplier, divided by the number of fringes. Pulse counting with LDA / LDV has been conducted by numerous authors, including Mostafa et al. [1989], Fleckhaus et al. [1987] and Tsuji et al. [1988]. Unlike isokinetic sampling, pulse counting is non-intrusive and can be used to obtain a standard deviation of the particle concentration at that point. However it is still limited as a single point technique. In addition Tsuji et al. [1988] found that LDA is limited to low particle mass loadings. For higher particle mass loadings, they used a purpose-built fiber optic probe. This probe consisted of a central fiber that emitted light and six surrounding fibers that detected light. The probe is inserted into the flow so that the fibers are perpendicular to the flow direction. As a particle passes in front of the probe it scatters light from the the central fiber. The light scattering is recorded by the surrounding fibers. Although their fiber optic probe enabled concentration measurements at high mass loading cases, it is a semi-intrusive technique that requires the probe to be inserted very close to the

region of interest.

Fan et al. [1990, 1992] used LDA to measure the mean and fluctuating velocity distributions of both solid and gas phases. To determine the particle concentration distribution and particles distributions, they used a Malvern laser diffraction instrument, which is based on Fraunhofer diffraction theory. The data are then subjected to a tomography transformation based on the work of Cormack [1963], cited by Fan et al. [1990]. This technique only provides line integrals of the concentration, and assumes that the particle concentration and particle size distribution are axisymmetric.

One of the significant limitations that single-point and even line-integral techniques have, is that they are unable to provide data of the instantaneous planar flow structures. Wark et al. [2000] used phase Doppler interferometry (PDI) to measure particle size, velocity, and number density of reacting and nonreacting, droplet-laden, acoustically excited, vertically orientated, round jets. The PDI technique is an extension to LDA, and is therefore subject to the same limitations of LDA. However, Wark et al. [2000] simultaneously conducted flow visualisation of their nozzle configuration using a pulsed light sheet with an Nd:YAG laser, phase-locked with the acoustic excitation, and a 35 mm camera. As these results were only for flow visualisation, they provide only qualitative data, but still enables greater understanding of the instantaneous flow structures.

To gain an understanding of instantaneous flow structures instantaneous planar or volumetric data are required, and the image sizes must be sufficiently large to resolve the large scale flow structures. Unfortunately, there are no developed quantitative volumetric techniques to provide this data, but some quantitative planar measurement techniques are available.

Zimmer et al. [2002a,b] use planer droplet sizing to obtain Sauter mean diameters. The planer droplet sizing method requires simultaneous measurements of both Mie-

scattering and planar laser induced fluorescence (PLIF). The Mie-scattering utilises the scattering of light from the droplets, and is used to measure the liquid droplet surface area. The PLIF technique requires that the droplets comprise a specific fluorescing dye of known concentration, and can be used to measure the volume of the droplets. The ratio of the two signals is proportional to the Sauter mean diameter. This technique has been previously reported by Yeh et al. [1993], LeGal et al. [1999] and Stojkovic and Sick [2001]. Domann and Hardalupas [2001a,b] have reported the limitations and uncertainties. A major limitation of planar droplet sizing is that it is restricted to droplets. The use of PLIF in particle-laden flow is possible, but the cost of pretreated particles is very high, and financially limits experiments to short run times and low particle mass loadings.

Longmire and Eaton [1992] investigated the structure of a particle-laden round jet. Particle velocities were measured using LDA. Planar measurements of the particle number density were obtained by particle counting of individually identification particles from photographs of the flow, illuminated by a pulsed laser sheet. Although particle counting provides absolute planar particle number densities, it is limited in spatial resolution and requires a sufficiently low particle loading to ensure that individual particles are identifiable. Particle mass loading has a strong influence on the flow field. Simulating conditions in cement kilns to enable assessment of the flow field should incorporate high mass loadings. However, the mass loading of PF in a cement kiln exceed the limits where particle counting is practical.

3.2 Planar nephelometry

The current research has a focus towards the understanding of the instantaneous planar field and as such, single point techniques are not suitable. Planar or volumetric instantaneous images are therefore required to investigate particle clustering.

A non-intrusive laser-based technique that provides instantaneous planar concentration data and corrects for light attenuation has been developed. The technique is known as planar nephelometry. During the experimental phase of the current research, the planar nephelometry technique was still under development. Therefore, for the current research, an early version of the planar nephelometry technique was used. The current section briefly describes this technique.

3.2.1 Nephelometry

Planar nephelometry is a non-intrusive laser based technique designed to determine instantaneous particle number densities in a plane. The technique does not require identification of individual particles and is therefore not a particle counting method as used by Eaton and Fessler [1994]. Planar nephelometry is an extension of marker nephelometry, which was first considered by Rosensweig et al. [1961], but also presented in Becker et al. [1965], Becker [1966] and Becker [1977]. The technique is commonly used in pharmaceutical and medical research where the determination of concentrations of particles in a solution are required. A small probe volume of a well-mixed particle laden solution is illuminated by a converging beam. The intensity of light scattered from particles is recorded on a photomultiplier. The concentration of particles in the probe volume is directly inferred from the voltage output of the photomultiplier. The scattering of n_p identical particles is n_p times that from a single particle.

As shown by Becker [1977] the general formulation for the detected signal from a

volume, Φ_V, is

$$\int_0^\infty \Phi_V d\lambda = \pi r_p^2 n_p \omega_i \omega_s \int_0^\infty \psi_{av} \tau_L \tau_1 \tau_s \tau_2 \tau_p I_0 d\lambda, \tag{3.1}$$

where τ are the transfer efficiencies of the signal through stages of detection, ω_i and ω_s are the solid angles of illumination and collection, ψ_{av} is the Mie-scattering cross section, and I_0 is the incident illumination.

This equation is based on two major assumptions. The first assumption is that the intensity of illuminating light on all of the n_p particles is constant. This assumption is valid in marker nephelometry because of the convergence of the beam illuminating the small probe volume. A particle in a collimated light sheet casts a shadow with cross sectional area equal to that of the particles. The shadow will persist down-beam of the particle with constant cross section, neglecting diffusion. If the light source is converging, the shadow will also converge. In the case of marker nephelometry, the effect of the shadows becomes negligible due to the strong convergence of the laser beam and the small probe volume that is investigated.

The second assumption is that the scattering of light is not diminished by interference by neighbouring particles. The criterion for effectively independent scatter by mono-dispersed spheres is that the centre-to-centre distance between particles is greater than three particle radii [Van De Hulst, 1957]. This criterion is easily obtained even with substantial particle loadings.

3.2.2 Extension from single-point to planar measurements

Planar nephelometry uses a light sheet to illuminate a plane and records the light scattered from particles on to a CCD array. The principle of the two methods is the

same; the scattering of light correlates to the number of particles. Whereas marker nephelometry provides a single voltage to indicate concentration of particles in a probe volume, planar nephelometry provides a value of intensity at each pixel. However, planar nephelometry cannot use the assumption that the incident light for each particle is equal. The light sheet used in planar nephelometry will typically diverge and the shadow cast by a particle can not be neglected. Therefore, quantification of the attenuation created by particle shadows and subsequent data correction are required to provide a quantitative assessment of particle concentration.

A calibration of planar nephelometry is provided by Kalt and Birzer [2005]. A method to correct for attenuation of particle loadings for collimated and diverging light sheets is described by Kalt et al. [2007] and Kalt and Nathan [2007] respectively.

For planar nephelometry the equation for the intensity of light scattered from particles and recorded on a given pixel of a CCD array Φ_p is

$$\Phi_p = \overline{\pi r_p^2} C_\kappa n_p I', \tag{3.2}$$

where $\overline{\pi r_p^2}$ is the average particle cross-sectional area available to scatter the signal and n_p is the number of particles in the volume. The term I' is the local corrected intensity of the laser sheet adjusted for losses, including extinction and divergence. The term C_κ is a scaling constant which is a function of wavelength, λ; particle characteristics, including size and reflectivity; and collection optics, such as magnification and f#.

3.2.3 Correction factor, C_κ

Determination of C_κ for the current work was via empirical data from Foreman [2008]. The experimental arrangement used by Foreman [2008], was similar to the current

arrangement, with the same particles and similarly dimensioned nozzle, but the particle distributions in Foreman [2008] had a greater level of axisymmetry at the nozzle exit. The laser and camera were the same for both research campaigns; however the laser sheet divergence was slightly different. The pixel resolution was 311 μm per pixel, whereas the current work has a resolution of 504 μm per pixel.

Figure 3.1: Uncorrected and corrected mean particle distributions. Raw data courtesy of Foreman [2008].

Figure 3.1 shows the uncorrected and correct mean images from an ensemble sourced from Foreman [2008]. The false colour map is scaled to highlight the flow structures. The nozzle exit is at the top of the individual images, and the flow is moving downwards. The 2 mm thick laser sheet comes from left to right of image. Both images have been

corrected for background noise, and cropped to size. The image on the right has been corrected for attenuation, using $C_\kappa = 1.5 \times 10^{-5}$ [Kalt and Nathan, 2007]. The good symmetry about the nozzle axis can clearly be seen in both images. However, as the laser light moves from left to right of the flow, attenuation of the light occurs. As a result, the signal strength on the right hand side of the uncorrected image is lower than the left, despite symmetry of the particle distributions. Visual inspection of the corrected image shows that the application of the attenuation correction is successful when using $C_\kappa = 1.5 \times 10^{-5}$.

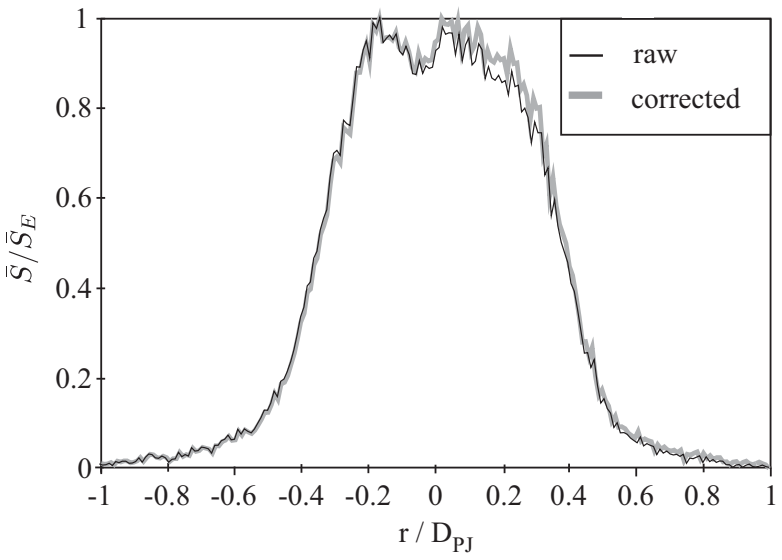

Figure 3.2: Uncorrected and corrected signal intensity at $x/D_{PJ} = 1$ for mean signal in the current data.

The current work does not have the same high level of symmetry as the example from Foreman [2008]. Therefore the same method to determine C_κ can not be applied. As stated previously, the value of C_κ is a function of the particle scattering characteristics, transmitting and receiving optics, and laser wavelength. The current work uses the same particles and laser and only differs with transmitting and receiving optics. To assess the suitability of the use of $C_\kappa = 1.5 \times 10^{-5}$ for the current work, a sensitivity study was conducted to assess the influence of C_κ on the signal intensity. The results show that, for the current work, there is little sensitivity to C_κ. Due to this fact, and

the strong similarities between the current experimental system and that of Foreman [2008], the value of $C_\kappa = 1.5 \times 10^{-5}$ is also used for the current work. The application of the attenuation correction with C_κ on the radial profile of data from the current research is shown in Figure 3.2. The symbol $\bar{S}$ is an approximation of the corrected signal Φ_p from Equation 3.2. It is an approximation because the actual particle radii are not constant, although this is assumed in the equation. The subscript E indicates the value determined at the exit plane. From this example the maximum correction to the data is 4%. Planar nephelometry has been used for the data processing in Birzer et al. [2004, 2005, 2008a,b, 2009].

3.2.4 Assumptions for planar nephelometry

Planar nephelometry is a technique that enables determination of particle concentrations based on the scattered light from particle. However, the particle number density cannot be determined without the assumption that size distribution is consistent throughout the flow. For this reason, all data is presented in terms of surface area, which does not require this assumption to be made. Nevertheless, since $Sk \leq 0.51$ for all particles and the average $Sk \approx 0.08$ (see Section 2.2), all particles respond well to the dominant large-scale motions. On this basis, while some variations in size distribution through the flow are inevitable, they are expected to be small, and the term "apparent concentration" is also employed in the text. For the current work, the estimated uncertainty of the applied corrections is 3%.

Chapter 4

Influences of jet precession on mean and fluctuating components of particle distributions

4.1 Introduction

The current chapter presents experimental results and a discussion on the influence of jet precession, in the form of the momentum ratio (G_{PJ}/G_{ANN}), on the distribution of the mean and fluctuating components of the particle distributions. For each experimental run, 202 instantaneous Mie-scattering images were collected. Mean and fluctuating components of the particle distribution data were produced from the ensembles of 202 images for each case. Details of the experimental conditions are summarised in Table 4.1.

Table 4.1: Operating conditions -variable jet precession experiments.

Parameter	Experimental Run Number						
	1	2	3	4	5	6	7
PJ inlet jet velocity, $U_{PJ(inlet)}$ [ms^{-1}]	0.0	22	54	99	154	211	286
PJ inlet Reynolds number, $Re_{PJ(inlet)}$	0.0	14245	35612	64218	101947	138955	188532
PJ momentum flux, G_{PJ}[N]	0.000	0.014	0.086	0.290	0.709	1.32	2.42
Annular jet velocity, U_{ANN} [ms^{-1}]	18.0	18.0	18.0	18.0	18.0	18.0	18.0
Annular Reynolds number, Re_{ANN}	5935	5935	5935	5935	5935	5935	5935
Annular momentum flux, $G_{ANN(f)}$ [N]	0.39	0.39	0.39	0.39	0.39	0.39	0.39
Annular momentum flux, G_{ANN}[N]	0.47	0.48	0.49	0.50	0.51	0.51	0.49
Momentum ratio, G_{PJ}/G_{ANN}	0.00	0.03	0.18	0.58	1.46	2.60	4.90
Momentum ratio, $G_{PJ}/G_{ANN(f)}$	0.00	0.04	0.22	0.74	1.81	3.36	6.19
Particle mass loading ratio, β	0.120	0.129	0.148	0.152	0.158	0.161	0.148

4.2 Results and discussion

Figure 4.1 shows the normalised mean particle distributions for seven cases of momentum ratios ranging from $0.00 \leq G_{PJ}/G_{ANN} \leq 4.90$. For each image individual scaling of the false colour map is used for clarity. The fluid-phase momentum flux of the annulus, $G_{ANN(f)}$, β, and therefore G_{ANN} are held constant in all cases. A qualitative trend of significantly increasing spread and decay rates with increasing G_{PJ}/G_{ANN} can be seen. The zone immediately downstream from the nozzle exit plane, identified by the lack of particles, can be seen to reduce in axial length with increasing $G_{PJ}/G_{ANN} \geq 0.03$.

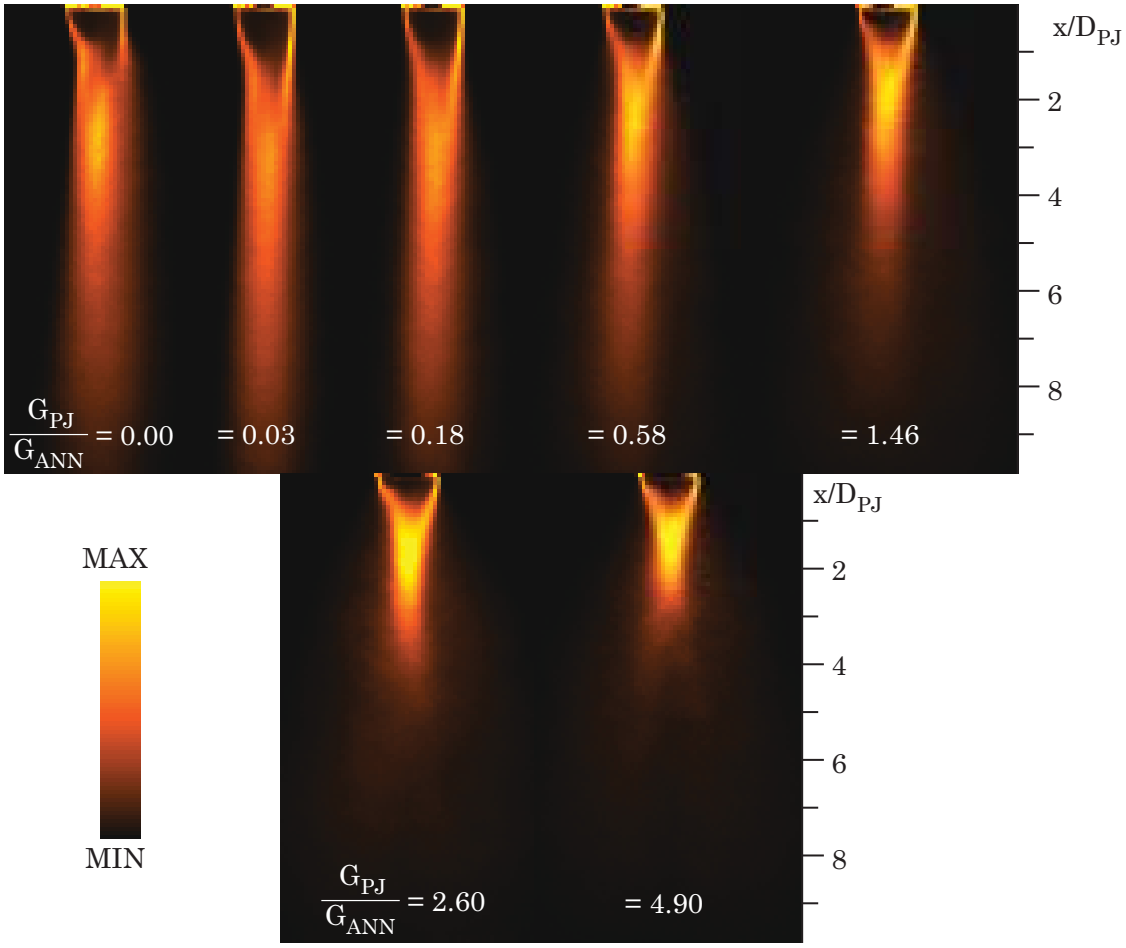

Figure 4.1: Mean particle distributions for $0.00 \leq G_{PJ}/G_{ANN} \leq 4.90$. Images are normalised to the maximum signal in each image.

The initial particle distributions immediately downstream from the jet exit are not symmetrical about the nozzle axis. This asymmetry is due to a non-uniform azimuthal distribution of particles in the co-annular jet, possibly due to a roping phenomenon within the co-annulus. The bias is particularly evident for $G_{PJ}/G_{ANN} = 0.00$ and can be seen to persist downstream. However, increasing G_{PJ}/G_{ANN} reduces the influence of the asymmetry.

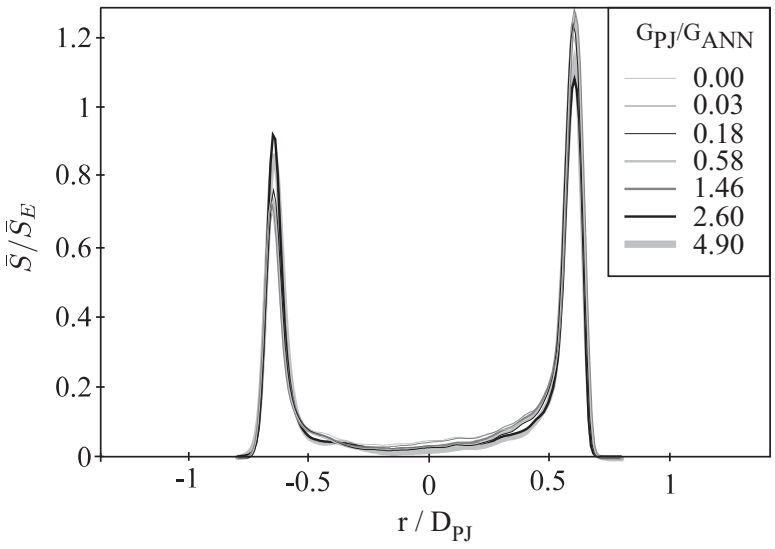

Figure 4.2: Radial profiles of normalised mean signals at $x/D_{PJ} = 0.1$ indicating bias due to asymmetry of the particle distributions in the annulus.

The particle distributions at the true exit plane cannot be measured accurately due to interference of light scattered by the nozzle. However, this interference is negligible for $x/D_{PJ} \geq 0.1$. Therefore the location $x/D_{PJ} = 0.1$ is used as the closest practical measure of distributions in the nozzle exit plane. The radial profiles at this location are presented in Figure 4.2. The profiles are normalised by the average of the maximum signal from each side of the annulus, along this radius for each case, which is termed $\overline{S}_E$.

The normalised particle distributions at $x/D_{PJ} = 0.1$ clearly show significant particle bias with an asymmetry about the nozzle axis. There is a difference in signal strength at

the two peaks of approximately 33 ± 3% for all cases except for the highest momentum ratio case, $G_{PJ}/G_{ANN} = 4.90$, where the bias is 20%. This indicates that the influence of the PJ for high G_{PJ}/G_{ANN} is significant upstream from $x/D_{PJ} = 0.1$.

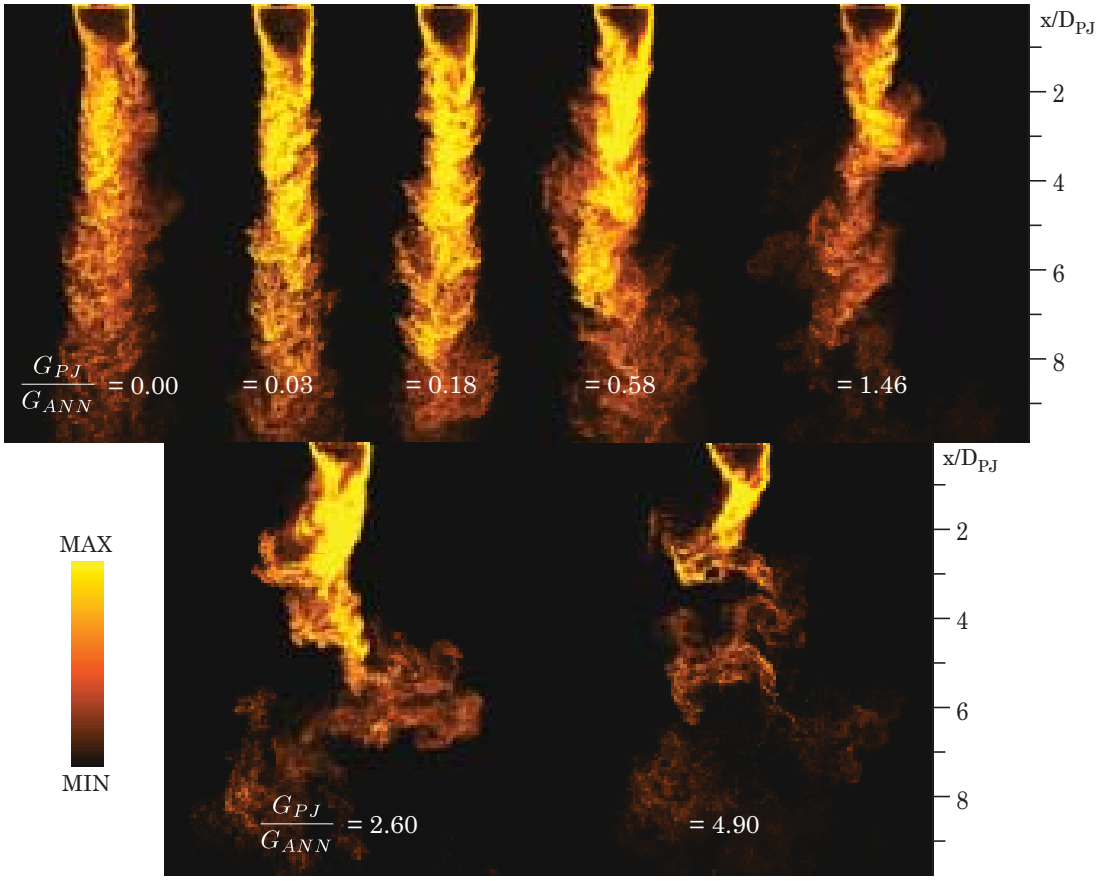

Figure 4.3: Instantaneous images for $0.00 \leq G_{PJ}/G_{ANN} \leq 4.90$.

Figure 4.3 provides seven instantaneous images that correspond to the mean images shown in Figure 4.1. By comparison of Figures 4.1 with Figure 4.3 it can be seen that, for $G_{PJ}/G_{ANN} \leq 0.18$, the shapes of the instantaneous distributions of particles are similar to their respective mean images. However, the instantaneous images become increasingly different from the mean with increased $G_{PJ}/G_{ANN} \geq 0.58$. These differences are evident throughout the flow field investigated. (N.B. The standard deviation of the particle distribution, S', is a direct measure of the difference between the instantaneous and mean data. These results are discussed later in this chapter.) Two features of the flow require specific discussion: The large, high particle concentration structures, that are only evident in the instantaneous image (especially for $G_{PJ}/G_{ANN} \geq 1.46$); and

the particle-devoid zone downstream of the nozzle exit plane, which can be seen in both mean and instantaneous images.

The large, high particle concentration structures that are evident in the instantaneous image relate to a phenomenon known as *preferential concentration*. These structures are discussed in Chapter 7. However, it should be noted that these structures confirm that the particles exhibit a strong response to the dominant large-scale flow oscillations.

For $G_{PJ}/G_{ANN} = 0.00$, the flow is that of a particle-laden annular flow with bluff body. A recirculation zone is created downstream of the bluff body (seen as the particle-devoid zone). As shown by Wicker and Eaton [1999, 2001], particles in jet flow are not easily entrained into a recirculation zone, and therefore these zones are identifiable by a void of particles. By increasing the momentum of the central jet slightly, the amount the recirculation decreases, and is possibly eliminated, because the bluff body effect is minimised, if not negated altogether. However, as the central jet is not particle-laden, the region downstream of the nozzle exit plane is still devoid of particles. This can be seen in both the mean and instantaneous images for $G_{PJ}/G_{ANN} \leq 0.18$.

As discussed in Section 1.2, with sufficient flow into the PJ nozzle inlet, jet precession occurs and consequently the jet exiting the nozzle has a deflection angle of approximately 45 degrees, and cuts across the face of the nozzle. The jet cross-section only fills about one third of the available nozzle exit. The influence of this jet can be seen qualitatively on the region immediately downstream of the nozzle exit plane for $G_{PJ}/G_{ANN} \geq 0.58$. The jet exiting the nozzle entrains the surrounding fluid. The side of the jet closest to the particle-laden annular flow entrains particles across the nozzle face, while the side of this jet closest to the nozzle centreline will cause a recirculation zone, which entrains some particles from the opposite size of the nozzle into the particle-devoid zone. Increasing G_{PJ}/G_{ANN} results in an increase in entrainment of particles across the nozzle face. As this jet precesses about the nozzle centreline, the mean image shows a shorter particle-devoid zone for increasing G_{PJ}/G_{ANN} (see Figure

4.7).

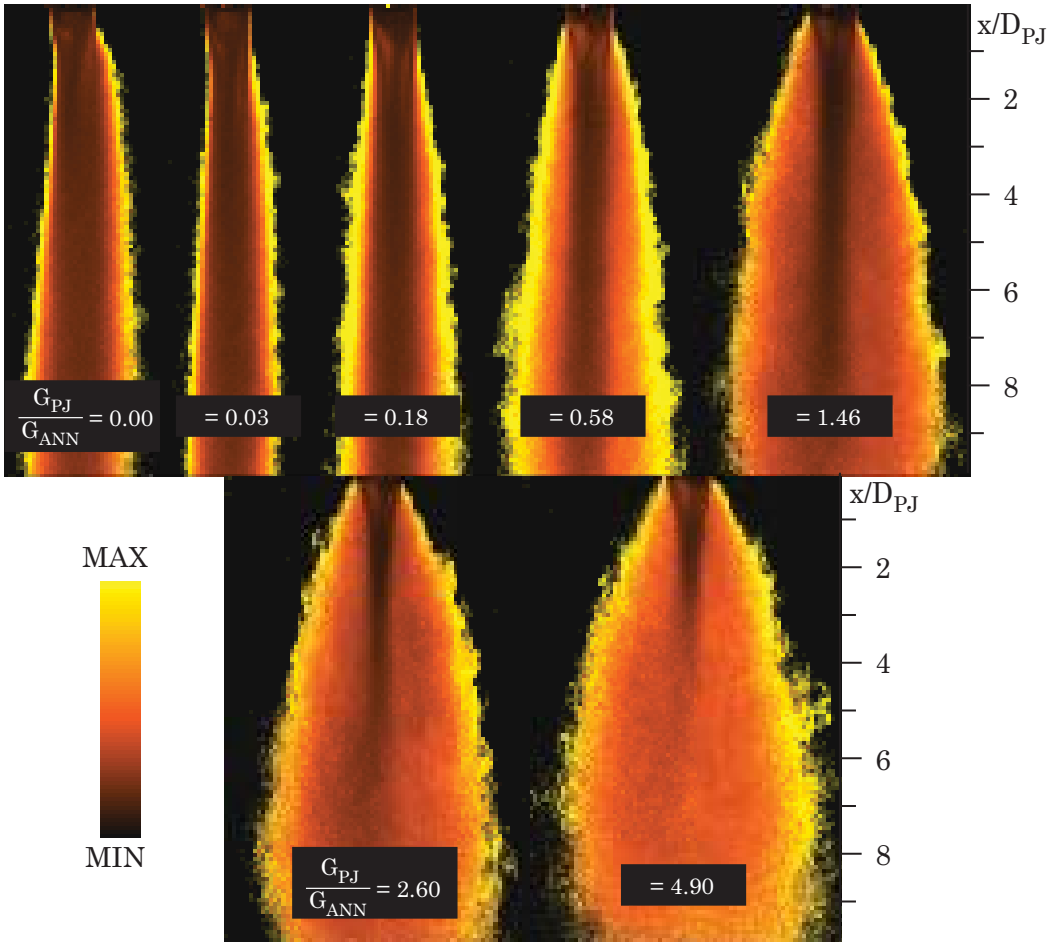

Figure 4.4: A set of images of the relative fluctuations, $S'/\overline{S}$, for $0.00 \leq G_{PJ}/G_{ANN} \leq 4.90$. The false colour map is optimised for each case.

The relative intensity of the fluctuating component of the particle distribution is determined by normalising the standard deviation of the particle distribution, S', by the local mean particle distribution, $\overline{S}$. This is termed the *relative fluctuations*. The relative fluctuations of the seven different momentum ratio cases are shown in Figure 4.4. The scale of the false colour map is set to highlight features in each case, and so differ from case to case. In particular, these images highlight the edges of the jets since, unlike the mean, the relative fluctuations exhibit very steep gradients near to the jet edge. This steep gradient results from the low mean signal near to the jet edge. In support of the findings from the mean data, the particle bias of the emerging jet is evident for $G_{PJ}/G_{ANN} = 0.00$ and 0.03. However, the influence of particle bias is less

pronounced for $G_{PJ}/G_{ANN} \geq 0.18$. The bias is not clearly noticeable at the nozzle exit plane for $G_{PJ}/G_{ANN} = 4.90$.

Increasing G_{PJ}/G_{ANN} above 0.18 results in increased spread of the jet edge. Interestingly this figure also shows that the spreading angle of the PJ flows decrease with axial distance. That is, the spreading rate is greatest close to the nozzle and decreases towards the downstream end of the image. This is consistent with trends in single-phase investigations, where the PJ flow is found to converge toward a far-field state comparable with a simple jet [Nathan et al., 2006]. The jet spread is also comparable with particle-laden swirling, co-annular jets with forced vortex generators investigated by Wicker and Eaton [1999].

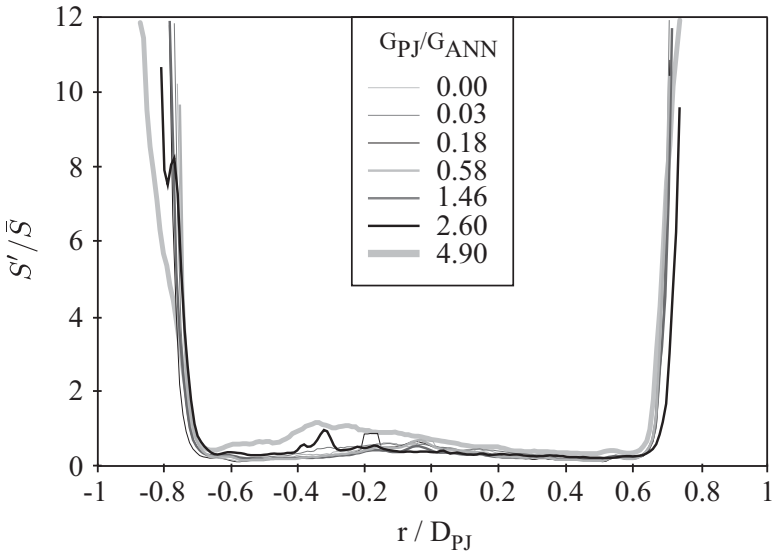

Figure 4.5: Radial profiles of relative relative fluctuations at $x/D_{PJ} = 0.1$.

Figure 4.5 shows profiles of the relative fluctuations at $x/D_{PJ} = 0.1$. Here, it can be seen that there is little difference in $S'/\overline{S}$ for increasing G_{PJ}/G_{ANN}, other than a slight increase for $G_{PJ}/G_{ANN} = 4.90$ in the range $-0.6 \leq r/D_{PJ} \leq 0$ and also a greater divergence on the left hand side of the image. Although this variation in profile for $G_{PJ}/G_{ANN} = 4.90$ is only present on the left hand side, and therefore asymmetric, it does support the previous findings that the influence of jet precession can have

an influence as close to the nozzle exit as $x/D_{PJ} = 0.1$. It also indicates that the entrainment of particles into the particle-devoid zone increases with G_{PJ}/G_{ANN}.

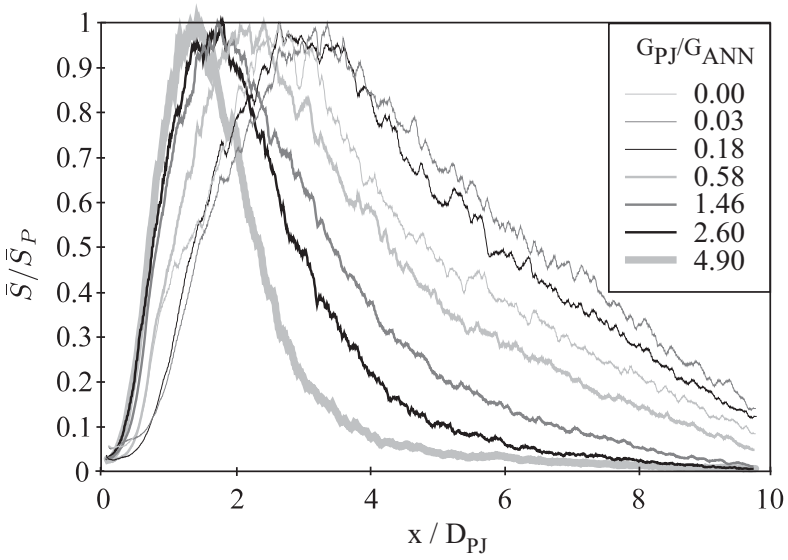

Figure 4.6: Normalised axial mean particle distributions along the nozzle axis for varying values of G_{PJ}/G_{ANN}.

Figure 4.6 shows the mean distributions of particles along the nozzle axis for the cases shown in Figure 4.1. For each case, the mean signal, $\overline{S}$, is normalised by the peak mean signal along the centreline, $\overline{S}_p$. It can be seen that there is an initial increase in $\overline{S}/\overline{S}_p$ to a peak associated with the convergence of the co-annular stream towards the centreline. This peak is called the *centreline concentration peak* and is located a distance x_p from the nozzle exit plane (see Figure 4.7 for notation).

An increase from $G_{PJ}/G_{ANN} = 0.00$ to $G_{PJ}/G_{ANN} = 0.03$ causes a decrease in the initial concentration gradient through this convergence region. Subsequent increases in G_{PJ}/G_{ANN} cause this gradient to increase. It is only when $G_{PJ}/G_{ANN} \geq 0.58$ that the initial rate of increase in apparent particle concentration is greater than that for $G_{PJ}/G_{ANN} = 0.00$. Downstream from the centreline concentration peak, the decay in centreline concentration can be seen to be highly dependent on G_{PJ}/G_{ANN}. Figure 4.7 illustrates these divergence and convergence regions in relation to centreline

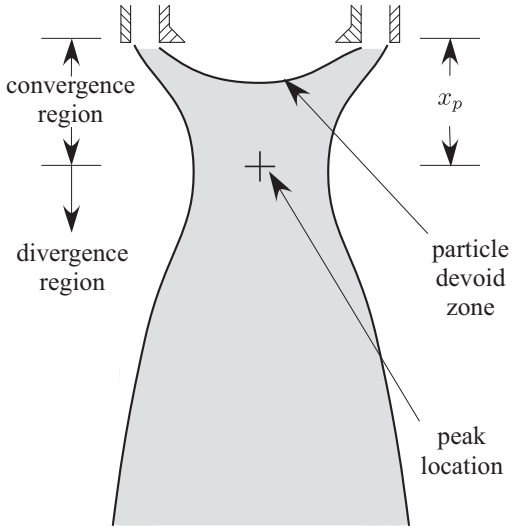

Figure 4.7: Schematic diagram of the mean particle distribution, showing the location of the centreline concentration peak and the convergence and divergence regions.

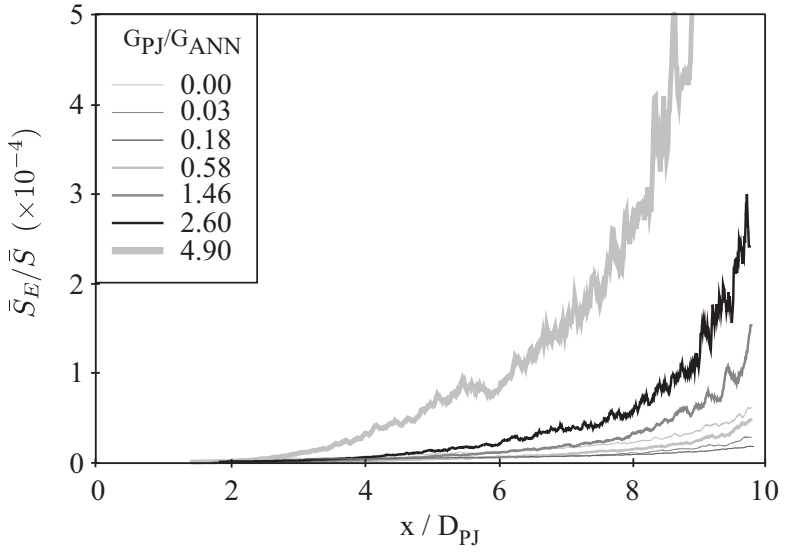

Figure 4.8: Inverse axial mean particle distributions along the nozzle axis for varying values of G_{PJ}/G_{ANN} and $x/D_{PJ} \geq x_p$.

concentration peak and distance x_p.

Figure 4.8 presents the inverse normalised axial mean particle distributions, $\overline{S}_E/\overline{S}$, for $x/D_{PJ} \geq x_p$. These profiles highlight the influence of jet precession on the centreline decay rate over the region $4 \leq x/D_{PJ} < 10$, and so complements Figure 4.6. From these results it is clear that for $G_{PJ}/G_{ANN} \leq 0.58$ there are only small difference between these profiles, but significant changes occur for $G_{PJ}/G_{ANN} \geq 1.46$. The profiles for $G_{PJ}/G_{ANN} < 1.46$ are not well resolved on this scale, but it is evident that they have not converged to a linear inverse decay within this axial range. Clearly, the profile for $G_{PJ}/G_{ANN} = 4.90$ exhibits a much higher decay rate than the other cases over the entire range downstream from the centreline concentration peak, and there is no evidence of the decay rate returning to a value more like that of a simple jet within this measurement range.

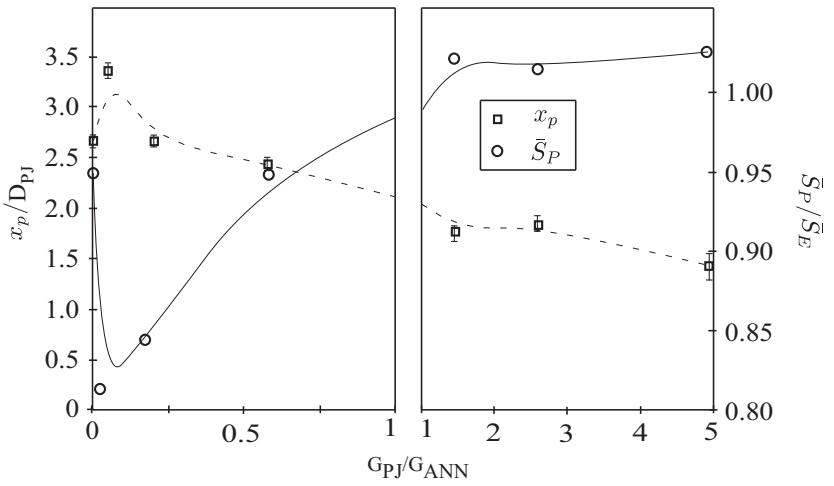

Figure 4.9: Normalised length to the centreline concentration peak (x_p/D_{PJ}) and normalised peak signal ($S'/\overline{S}$) for varying G_{PJ}/G_{ANN}.

The dependence of both the location of the centreline concentration peak, and its magnitude, $\overline{S}_p$, on G_{PJ}/G_{ANN} are shown in Figure 4.9 (note the two scales). The error bars correspond to a $\pm$ 3% variation in the magnitude of the signal, $\overline{S}_p$. The influence of increased G_{PJ}/G_{ANN} is clearly evident and highlighted by the trend lines. An increase in G_{PJ}/G_{ANN} from 0.00 to 0.03 results in the location of the centreline

concentration peak being translated further from the nozzle exit. Subsequent increases in G_{PJ}/G_{ANN} translates the centreline concentration peak closer to the nozzle exit plane. Again, for the cases investigated, it is only for $G_{PJ}/G_{ANN} \geq 0.58$ that the centreline concentration peak is closer to the nozzle than for $G_{PJ}/G_{ANN} = 0.00$. A similar trend, but in the opposite direction, is exhibited by $\overline{S}_p$. The asymptotic-like convergence suggests that most of the benefits of jet precession can be expected to be achieved with $G_{PJ}/G_{ANN} \approx 4.90$, although some benefits are present as early as $G_{PJ}/G_{ANN} = 1.46$. The implication of these results is that the jet exhibits two possible modes; an annular-dominated mode, and a PJ-dominated mode. The annular-dominated mode occurs for $0.00 \leq G_{PJ}/G_{ANN} < 0.18$ ($0.00 \leq G_{PJ}/G_{ANN(f)} < 0.22$). The PJ-dominated mode occurs for $G_{PJ}/G_{ANN} \gtrsim 1.46$ ($G_{PJ}/G_{ANN(f)} \gtrsim 1.86$). For $0.18 \lesssim G_{PJ}/G_{ANN} \lesssim 1.46$ ($0.22 \lesssim G_{PJ}/G_{ANN(f)} \lesssim 1.86$) there is a transition between the two modes.

These modes are also present in the instantaneous distributions shown in Figure 4.3. In the annular-dominated mode the instantaneous images are similar to the mean images. The particle-devoid zone can be seen to grow longer, and therefore the centreline concentration peak, which must be downstream of this zone, is shifted away from the nozzle. In the PJ-dominated mode, the precessing motion of the PJ can be seen to create regions of high concentration and increase the spread of the jet. The particle-devoid zone is shorter than those found in the annular-dominated mode, and therefore the centreline concentration peak is closer to the nozzle exit plane. For $0.18 \leq G_{PJ}/G_{ANN} \leq 1.46$ the transition from annular-dominated to PJ-dominated is clearly evident.

The corresponding radial profiles at the centreline concentration peak are presented in Figure 4.10. These values are normalised to $\overline{S}_p$. Although some asymmetry is present, the severity of asymmetries present at $x/D_{PJ} = 0.1$ (Figure 4.2) are greatly reduced. All radial profiles shown in Figure 4.10 exhibit approximately Gaussian distributions. The profiles on the left-hand side of the nozzle axis overlap more strongly than on the

right-hand side. The location of the peaks are biased slightly towards the right-hand side of the nozzle axis; that is, to the side with the higher particle mass loading at the nozzle exit plane. Despite the bias, it is clear that G_{PJ}/G_{ANN} has an observable influence in reducing the profile widths at the location of the centreline concentration peak. However, care must be taken in any direct comparison due to the different axial location of each profile. As the location of the centreline concentration peak corresponds to the narrowest width of the jet, these results indicate that jet precession can cause a significant reduction in the minimum width of the jet.

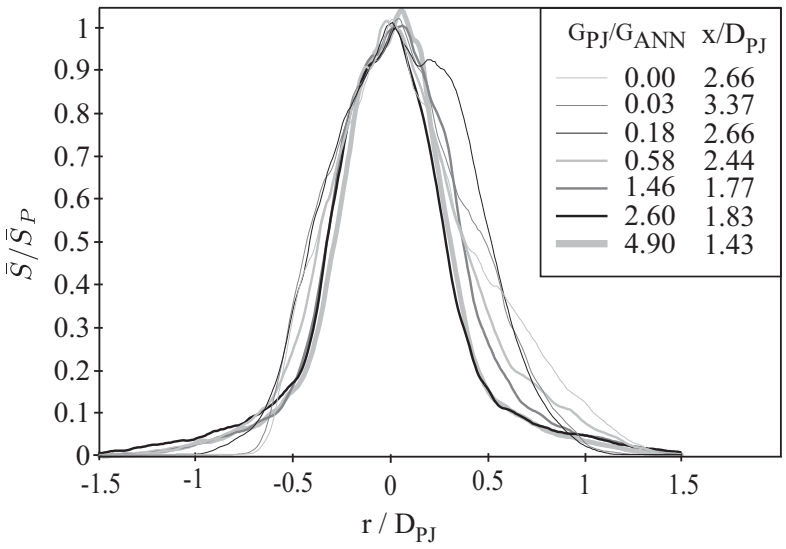

Figure 4.10: Radial profiles of normalised mean signals at the centreline concentration peaks, (i.e. the neck region).

The relative fluctuations along the centreline are shown in Figure 4.11. For $G_{PJ}/G_{ANN} \geq 0.58$ a near-field hump in $S'/\overline{S}$ is found at $x/D_{PJ} \approx 0.5$. This near-field hump is not evident for the cases with lower G_{PJ}/G_{ANN}. In the instantaneous images shown in Figure 4.3 it can be seen that some particles are entrained into the particle-devoid zone, when G_{PJ}/G_{ANN} is high. However, the mean image (see Figure 4.1) still shows this region to be almost completely devoid of particles. A result is that there is a much higher value of $S'/\overline{S}$.

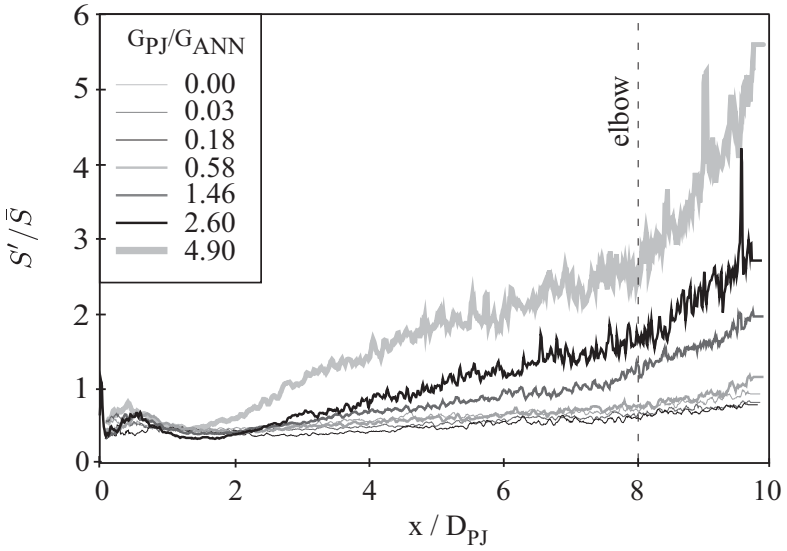

Figure 4.11: Relative fluctuation of the centreline particle distribution.

Further downstream in the region of $1.4 \lesssim x/D_{PJ} \lesssim 3.4$, each case exhibits a local minimum for the relative fluctuations along the centreline (Figure 4.11). These minima correspond to the respective locations of the centreline concentration peaks. This is because the instantaneous jet cuts across the nozzle axis at the centreline concentration peak, drawing particles with it. Hence, the precession always takes the particles through this point, so that the relative fluctuations are lowest. (Note that the cycle to cycle variations are still significant).

Downstream from the centreline concentration peak, $S'/\overline{S}$ steadily increases for all cases. This increase is marginally steeper for higher values of G_{PJ}/G_{ANN} between 0.00 and 0.58. For $G_{PJ}/G_{ANN} \geq 1.46$ this rate becomes much greater with increasing G_{PJ}/G_{ANN}. The increase in slope with increasing G_{PJ}/G_{ANN} is a result of the increased spreading of the mean jet and corresponding lower mean signal along the centreline. It should be remembered from the instantaneous images that regions of high and low particle concentrations form. For the case of $G_{PJ}/G_{ANN} = 4.90$ shown in Figure 4.3 it can be seen that along the centreline between $6 < x/D_{PJ} < 8$ the signal is very low (if not zero). There are also sudden transitions from high signal strength

to low (or negligible) signal strength. However, the mean signal for this location is non-zero and shows a rather smooth transition. The comparison of the instantaneous and mean signals, as represented by $S'/\overline{S}$, are correspondingly high. It can therefore be suggested that the steep increase in $S'/\overline{S}$ may correspond to an increase in these regions of high particle concentration. In Figure 4.11 the profiles also exhibit a sudden change in slope, or an elbow point, at $x/D_{PJ} \approx 8$. This elbow is discussed below in conjunction with the halfwidth profiles.

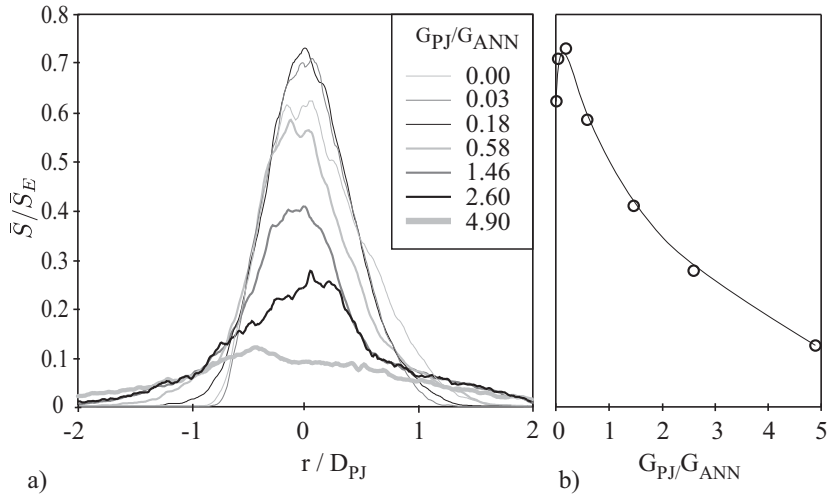

Figure 4.12: Radial profiles of normalised mean signals at $x/D_{PJ} = 4$.

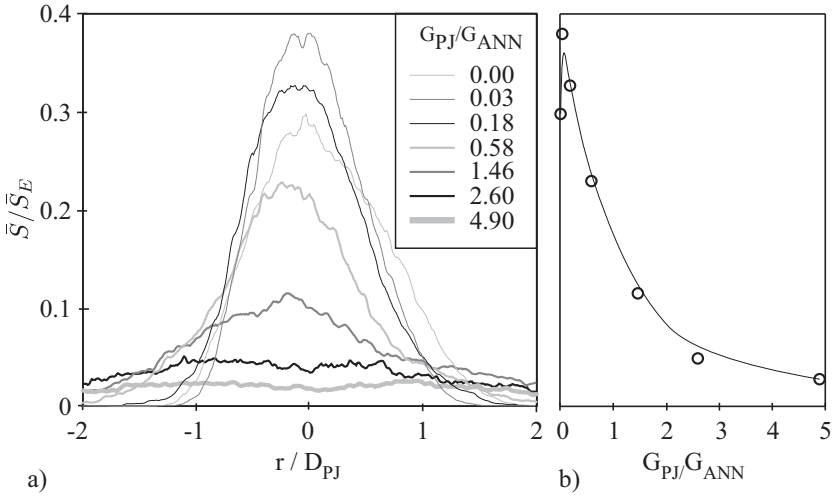

Figure 4.13: Radial profiles of normalised mean signals at $x/D_{PJ} = 7$.

The mean radial profiles at $x/D_{PJ} = 4$ and 7 are presented in Figures 4.12 and 4.13 respectively. The profiles are normalised to $\overline{S}_E$ for each case, as before. The radial profiles show that the influence of particle bias is greatly reduced at these axial locations. A clear trend is apparent, that a small increase in G_{PJ}/G_{ANN} from zero results in a taller, narrower near-field peak. However, further increases for $G_{PJ}/G_{ANN} \geq 0.58$ result in a significant lowering and broadening of the peak. This is indicative of the enhanced mixing created by jet precession.

The trend of flatter, wider profiles for increasing G_{PJ}/G_{ANN} in the range $G_{PJ}/G_{ANN} \geq 0.03$ is also evident at $x/D_{PJ} = 7$. The difference between the PJ-dominated and the annular-dominated cases are greater at $x/D_{PJ} = 7$ compared with $x/D_{PJ} = 4$. This indicates that the influence of G_{PJ}/G_{ANN} continues to manifest further downstream. This may also be evidence of the flow exhibiting a transition from the near field to reach a more fully developed region by $x/D_{PJ} = 7$.

Figures 4.12 and 4.13 also show corresponding plots of the peak value of $\overline{S}_E$ with variations to G_{PJ}/G_{ANN}. These profiles highlight the strong similarities in the trends discussed; that is, the elongation of the jet for annular-dominated cases and a shortening and widening of PJ-dominated case.

A small increase in G_{PJ}/G_{ANN} from 0.00 to 0.03 results in a narrowing of the radial profile of the relative fluctuations at both axial locations. As discussed above, this range of G_{PJ}/G_{ANN} corresponds to annular-dominated flows. As G_{PJ}/G_{ANN} increases above $G_{PJ}/G_{ANN} \geq 0.03$, the flow becomes more PJ-dominated and the profile of the relative fluctuations at both radial locations become wider and flatter.

The relative fluctuations along radial profiles $x/D_{PJ} = 4$ and 7 are shown in Figures 4.14 and 4.15 respectively. These results support the finding that the jet width increases for $G_{PJ}/G_{ANN} \geq 0.03$.

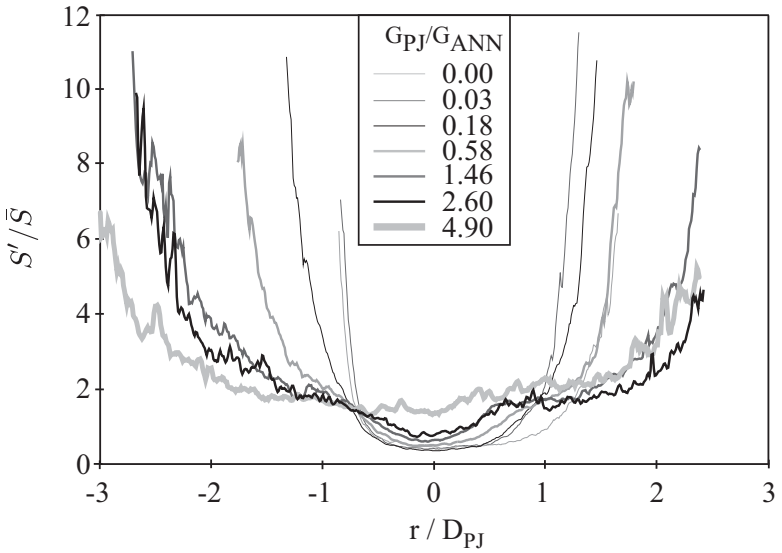

Figure 4.14: Radial profiles of relative relative fluctuations at $x/D_{PJ} = 4$.

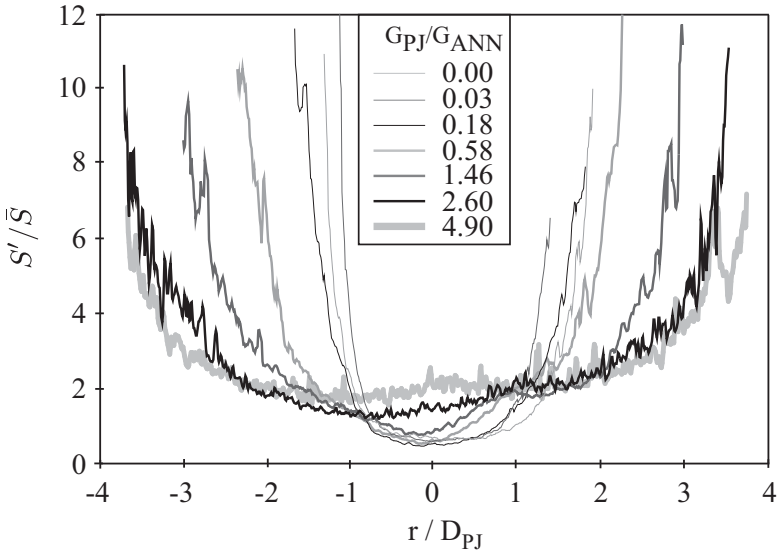

Figure 4.15: Radial profiles of relative fluctuations at $x/D_{PJ} = 7$.

From Figures 4.11, 4.14 and 4.15 it can be seen that, for each case, the relative fluctuations increase downstream from centreline concentration peak and radially outwards from the nozzle centreline. A small increase in G_{PJ}/G_{ANN} from 0.00 to 0.03 results in a decrease in the relative fluctuations both axially and radially and a narrowing of the

outer edge of the jets. However, further increases in $G_{PJ}/G_{ANN} \geq 0.18$ increases the fluctuations and the width of the outer edge of the jet downstream from the centreline concentration peak. This is due to the dominance of the PJ flow.

Figure 4.16 shows the halfwidth concentration profiles for the seven cases. In all cases the halfwidths initially converge to a narrow *waist* and then diverge with increasing distance downstream. The waist for $G_{PJ}/G_{ANN} = 0.00$ is narrower than for $0.03 \leq G_{PJ}/G_{ANN} \leq 0.18$. For $G_{PJ}/G_{ANN} \geq 0.03$ an increase in G_{PJ}/G_{ANN} result in greater initial convergence rates and a narrowing of the waists. These characteristics can also be identified in the instantaneous images shown in Figure 4.3. The divergence of the halfwidths downstream from the waist are similar for cases $G_{PJ}/G_{ANN} \leq 0.58$. However, the divergence increases greatly with increases in $G_{PJ}/G_{ANN} \geq 1.46$. From a comparison of Figure 4.16 to Figure 4.11 it can be seen that the elbow at $x/D \approx 8$ also corresponds to the location where the radial spread of the jet decreases.

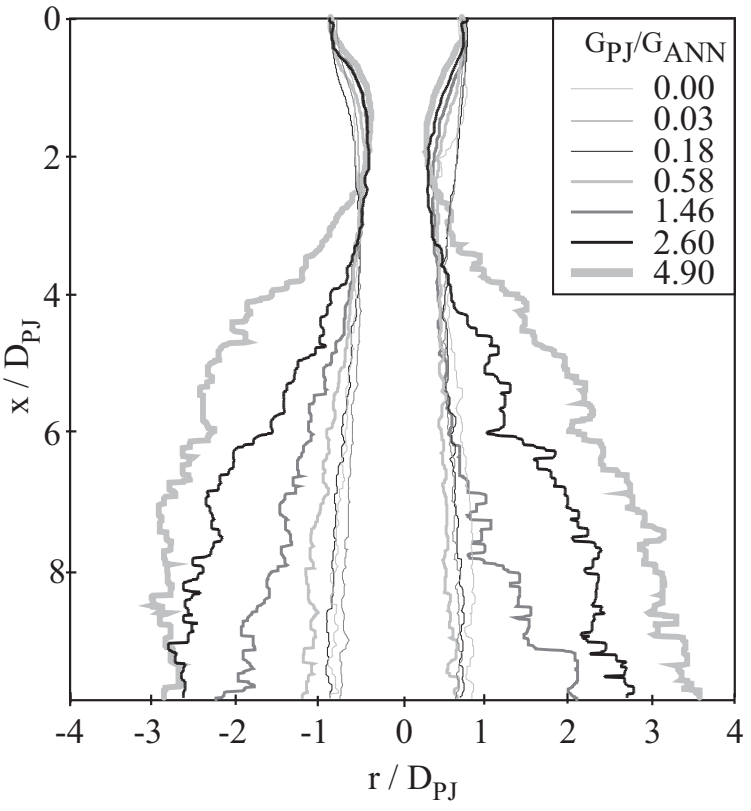

Figure 4.16: Mean particle concentration halfwidth profiles.

It can also be seen with further comparisons to Figures 4.14 and 4.15 that, while increasing G_{PJ} for $G_{PJ}/G_{ANN} \geq 0.18$ results in a narrower waist as measured by the halfwidth, from the relative fluctuating data it can be seen that this increase results in a wider spread of the absolute edge of the jet. This is also consistent with the particles responding well to the dominant large-scale oscillations. That is, the edge of the jet exhibits a different trend to the halfwidths in the necking region.

From these results it can be seen that jet precession has a very strong influence on mean and fluctuating component of the particle distributions. It is known that the instantaneous jet exiting from an unconfined PJ nozzle precesses about the nozzle axis with an initial deflection angle of approximately 45 degrees. It also emerges from one side of the nozzle and crosses the nozzle axis. Increasing G_{PJ}, while all other variables remain constant, increases the local radial momentum of the total jet. It also increases the entrainment of ambient fluid and particles towards, and across, the nozzle axis. This explains the strong necking for cases with high G_{PJ}/G_{ANN}. It also implies that the particles respond reasonably well to these large scale oscillations, as deduced from Sk being less than unity (see Section 2.2).

The case $G_{PJ}/G_{ANN} = 0.00$ corresponds to an annular jet with a bluff body. This configuration produces a central recirculation zone. With only a small flow through the central nozzle, the central PJ stream has insufficient momentum to have significant influence, but it does have sufficient flow to reduce, or even eliminate, the significance of the central recirculation zone (although the particle-devoid zone is still evident, it is a result of the flow from the particle-unladen central jet). This is a possible explanation for why in the mean distribution, a small increase in G_{PJ}/G_{ANN} from 0.00 to 0.03 results in a decrease in the initial convergence rates, pushes the location of the centreline concentration peak downstream, causes a widening of the waist, and decreases the rate of centreline and particle divergence.

For $G_{PJ}/G_{ANN} < 0.18$ the annular stream dominates the flow and distribution of

particles. For $0.18 \lesssim G_{PJ}/G_{ANN} \lesssim 1.46$ there appears to be a transition from a annular-dominated flow to PJ-dominated flow. This is seen with a narrowing of the waists of the halfwidths for increases in G_{PJ}/G_{ANN} above 0.18. Along the centreline, increasing G_{PJ} results in an increase in the initial particle convergence, a shift of centreline concentration peak closer to the nozzle exit, and an increase in the rate of particle divergence downstream from the centreline concentration peak. The greater the value of G_{PJ}/G_{ANN}, the more pronounced these effects.

4.3 Conclusions

Measurements have been performed on the influence of jet precession on the mean and fluctuating components of particle distributions in the near-field of a two-phase jet employing a Precessing Jet nozzle. The distribution of particles are found to be dominated by two separate modes; annular-, or PJ-dominated. The dominance of these modes depends on the relative momentum of the inner and outer streams. For $0.00 \leq G_{PJ}/G_{ANN} < 0.18$ the particle distributions are dominated by the influence of the annular stream. For $G_{PJ}/G_{ANN} \gtrsim 1.46$ the distributions of particles are dominated by the PJ stream. A transition from annular- to PJ-dominance occurs for $0.18 \lesssim G_{PJ}/G_{ANN} \lesssim 1.46$.

The case $G_{PJ}/G_{ANN} = 0.00$ corresponds to an annular jet, which produces a central recirculation zone. Small increases in G_{PJ}/G_{ANN}, while remaining in the regime that classifies annular-dominated mode, reduce, or even eliminate the significance of the central recirculation zone, causing an elongation of the overall jet. This results in the centreline concentration peak being translated further downstream, a widening of the waist, and a narrowing of the jet spread downstream from the centreline concentration peak.

For $G_{PJ}/G_{ANN} \gtrsim 0.18$ the PJ flow becomes influential. Increases in G_{PJ}/G_{ANN} increase the entrainment of particles across the face of the nozzle, translate the centreline concentration peak closer to the nozzle exit plane, produce a narrower waist and increase the jet spread downstream from the centreline concentration peak. However, it is not until $G_{PJ}/G_{ANN} \geq 0.58$ that the PJ momentum is sufficient to have translated the centreline concentration peak closer to the nozzle than for $G_{PJ}/G_{ANN} = 0.00$. Similarly it is only when $G_{PJ}/G_{ANN} \geq 0.58$ that the spread of the jet downstream from the centreline concentration peak is greater and the waist is narrower than for $G_{PJ}/G_{ANN} = 0.00$. Increasing G_{PJ}/G_{ANN} above 0.58 also causes an increase in fluctuations relative to the mean. This is consistent with the increased presence of clus-

tering observed by Smith et al. [1998a, 2002]. While the rate of spread has reduced by $x/D_{PJ} \approx 8$, the inverse centreline decay behaves differently, exhibiting increased inverse decay. This shows that the flow is still in transition to a far-field behaviour.

The particle bias emerging from the co-annulus will not propagate as strongly with sufficiently high G_{PJ}/G_{ANN}. For $G_{PJ}/G_{ANN} = 4.90$, the bias is 20% at $x/D_{PJ} = 0.1$ (as seen in Figure 4.2). However, at the location of the centreline concentration peak the bias is negligible. For $G_{PJ}/G_{ANN} = 4.90$, $x_p \approx 1.5D_{PJ}$. A uniform particle distribution in an annular nozzle is unlikely in an industrial situation. Hence, the effect on performance of any initial particle bias is likely to be less significant when sufficient PJ flows are used to mitigate these effects.

Chapter 5

Influences of particle mass loading on mean and fluctuating components of particle distributions

5.1 Introduction

The previous chapter provides results and discussion of the influence of the momentum ratio, G_{PJ}/G_{ANN}, on the mean and fluctuating components of the particle distributions. The value of particle mass loading for that data is $\beta = 0.14 \pm 0.021$. Although this variation is small and not expected to have a significant influence of the particle distributions [Fan et al., 1992], there is still a need to confirm this finding or, if necessary, estimate the associated errors. The current chapter examines the influence of variations of β on the flow, in order to assess the how significant variations in β are on the previous chapters' results.

The addition of particles to a stream with constant fluid momentum results in a varia-

tion in the total momentum of the stream. In order to maintain G_{PJ}/G_{ANN}, but vary β, the fluid flow rate needs to be changed for each case. As the influence of G_{PJ} has been shown in the previous chapter to have substantial effects to the distribution of particles, it is necessary to ensure G_{PJ} is held constant. However, adjusting the annular stream fluid flow rate to maintain G_{ANN} while varying β may introduce difficulties with comparing the actual mixing of the streams and phases. Hence, for the current chapter the fluid momentum of the annular stream, $G_{ANN(f)}$ is held constant, and thus $G_{PJ}/G_{ANN(f)} = 6.19$ for all cases presented in this chapter. A high value of G_{PJ} has been selected to reduce the effects of the initial particle bias, as shown in Chapter 4. The range of particle mass flow rates investigated is $0.041 \leq \beta \leq 0.461$. This range has been selected as it incorporates the values of β that approach the maximum and minimum limits at which the experimental configuration can record useable data. For the cases investigated, G_{PJ}/G_{ANN} varies from 3.02 ($\beta = 0.461$) to 5.95 ($\beta = 0.041$), as shown in Table 5.1. In comparison to the previous chapter, in the current chapter the case $\beta = 0.148$ corresponds to the case $G_{PJ}/G_{ANN} = 4.90$.

Table 5.1: Operating conditions -variable particle mass loading experiments.

	Experimental Run Number						
Parameter	1	2	3	4	5	6	7
PJ inlet jet velocity, $U_{PJ(inlet)}$ [ms^{-1}]	286	286	286	286	286	286	286
PJ inlet Reynolds number, $Re_{PJ(inlet)}$	188532	188532	188532	188532	188532	188532	188532
PJ momentum flux, G_{PJ}[N]	2.42	2.42	2.42	2.42	2.42	2.42	2.42
Annular jet velocity, U_{ANN} [ms^{-1}]	18.0	18.0	18.0	18.0	18.0	18.0	18.0
Annular Reynolds number, Re_{ANN}	5935	5935	5935	5935	5935	5935	5935
Annular momentum flux, $G_{ANN(f)}$ [N]	0.39	0.39	0.39	0.39	0.39	0.39	0.39
Annular momentum flux, G_{ANN}[N]	0.41	0.45	0.48	0.50	0.50	0.57	0.80
Momentum ratio, G_{PJ}/G_{ANN}	5.95	5.40	5.06	4.90	4.86	4.30	3.02
Momentum ratio, $G_{PJ}/G_{ANN(f)}$	6.19	6.19	6.19	6.19	6.19	6.19	6.19
Particle mass loading ratio, β	0.041	0.092	0.129	0.148	0.152	0.226	0.461

5.2 Results and discussion

Seven mean images for $G_{PJ}/G_{ANN(f)} = 6.19$ with $0.041 \leq \beta \leq 0.461$ are presented in Figure 5.1. The scales of the false-colour map are individually optimised for each case to highlight the flow features, which are quite similar. Notable differences may be attributed to the lower signal strength from lower values of β, and therefore fewer particles to scatter light.

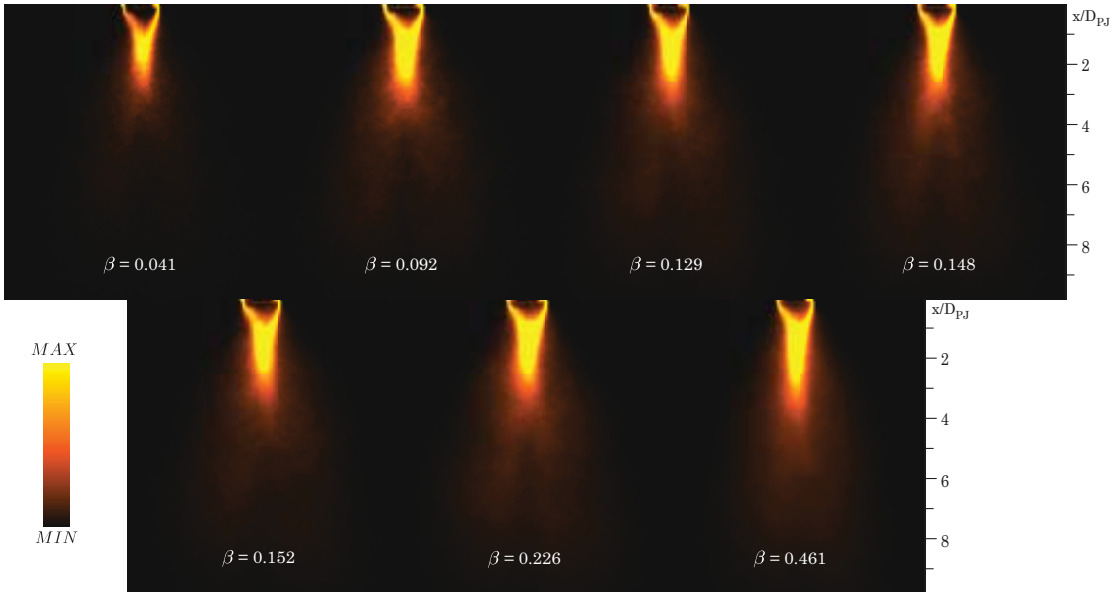

Figure 5.1: A set of images of the mean particle distributions for $G_{PJ}/G_{ANN(f)} = 6.19$ and varying β. The false colour map is optimised for each image to highlight variation in particle distributions.

Examples of instantaneous images that correspond to the mean images are presented in Figure 5.2. As per the previous figure, the false colour map is scaled for each case to highlight flow structures. Figure 5.3 presents the relative fluctuations, corresponding to cases shown in Figures 5.1 and 5.2. The main features in both figures are similar to each other. This is in contrast with results shown in Chapter 4 where it was evident that these structures varied considerably with variations in G_{PJ}/G_{ANN}. Other than the variations in recorded signal, which result from variations in β, there are no relevant discernible differences between the instantaneous images or the relative fluctuations.

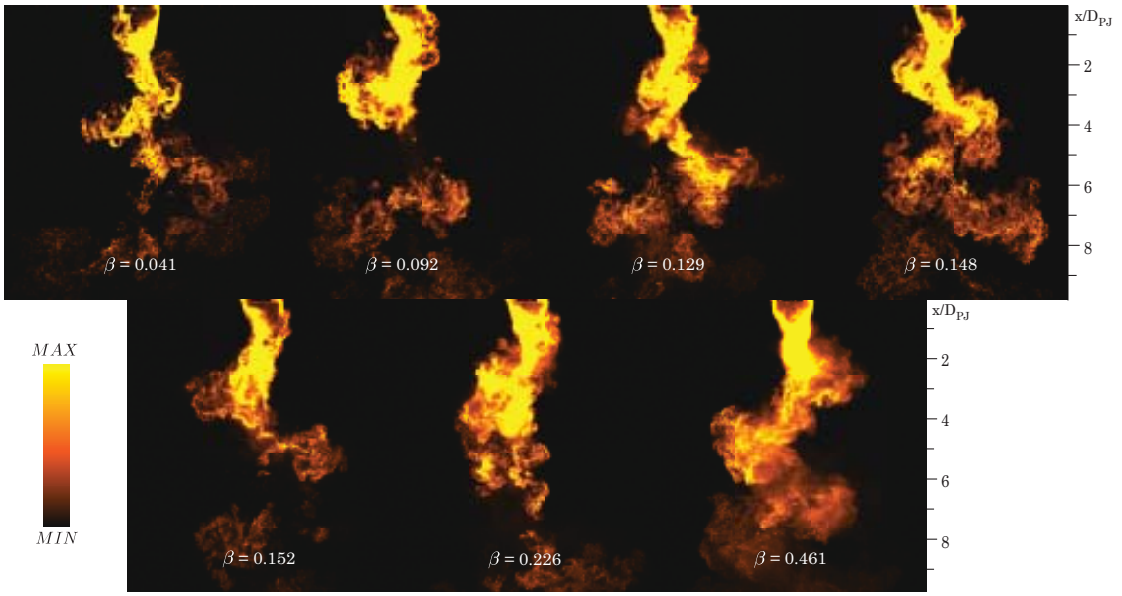

Figure 5.2: A set of images of the instantaneous particle distributions. The false colour map is optimised for each image to highlight variation in particle distributions.

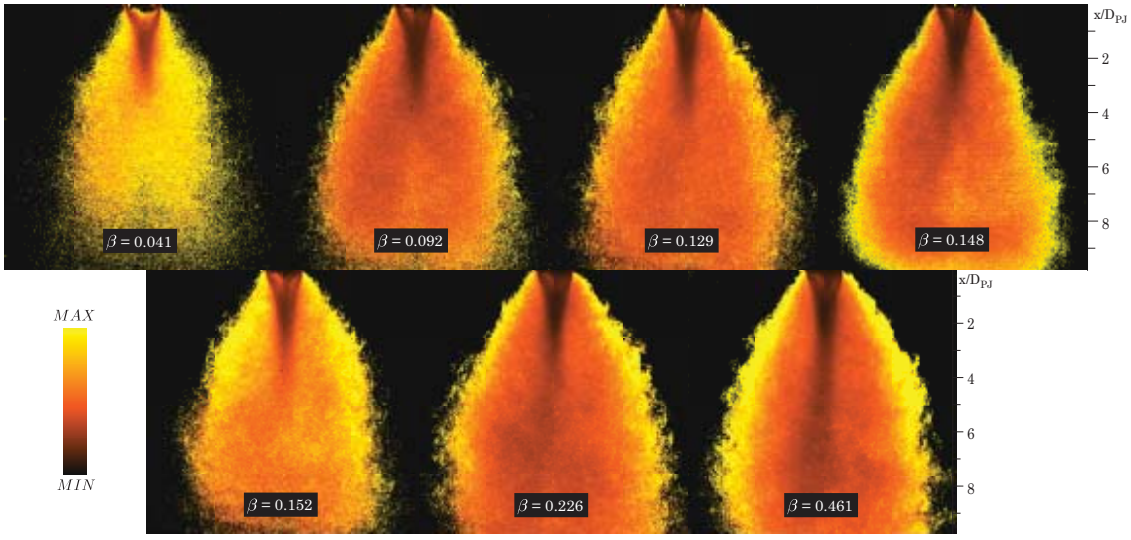

Figure 5.3: A set of images of the relative fluctuations, $S'/\overline{S}$. The false colour map is optimised for each image to highlight variation in particle distributions.

The radial profile at $x/D_{PJ} = 0.1$ for the seven different cases are shown in Figure 5.4. The particle bias at the nozzle exit is slightly stronger for lower values of β. However, these variations are small and, as shown in Section 4.2, the influence of jet precession mitigates the initial bias quickly. The relative signal strengths, $\overline{S}/\overline{S_E}$, for

$-0.5 \leq r/D_{PJ} \leq 0.5$ are also higher with increased β. As discussed in Section 4.2, the jet exiting the PJ entrains particles across the face of the jet, and also entrain some particles into the particle-devoid zone (see Figure 4.7). More particles entrained into the particle-devoid zone, while the mean signal is still low, results in higher values of $\overline{S}/\overline{S_E}$. It is suggested that, for the range investigated, the higher β, the greater the particle entrainment and therefore the higher the value of $\overline{S}/\overline{S_E}$.

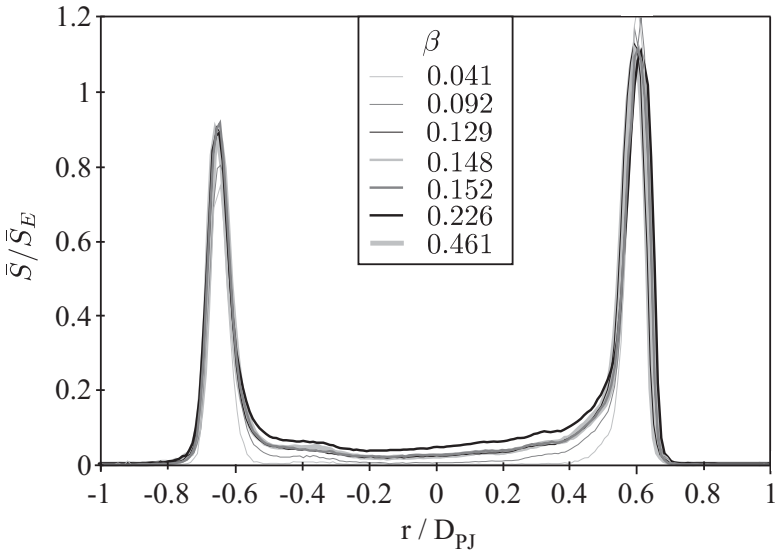

Figure 5.4: Radial profiles of normalised mean signals at $x/D_{PJ} = 0.1$ indicating bias due to asymmetry in the annulus.

Figure 5.5 presents the mean distributions of particles along the axis centreline for the seven different cases. The profiles are reasonably similar to each other. The initial convergence of particles and the location of the centreline concentration peak appear to be coincident. This supports previous findings by Fan et al. [1990] that the influence of β is almost negligible at the nozzle exit. However, there is a trend of a decreased decay rate downstream from the centreline concentration peak for increased β. This would then result in an elongation of the jet with increasing β, which supports previous finding from Wall et al. [1982], as discussed in Subsection 1.4.2. These results indicate that there is little influence from β on the particle distribution in the near-nozzle region. However, there is an elongation of the jet further downstream.

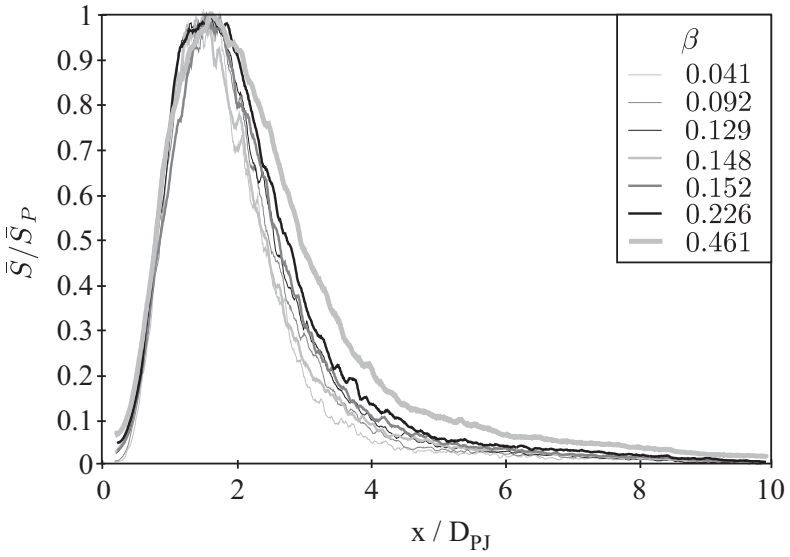

Figure 5.5: Normalised axial mean particle distributions along the nozzle axis for varying values of β and $G_{PJ}/G_{ANN(f)} = 6.19$.

As discussed in Subsection 1.4.2 due to particle inertia, the maximum obtainable particle velocity in a constant velocity particle laden nozzle will always be lower than the maximum fluid velocity. Exiting the nozzle both phases have similar velocities; however, momentum dissipation of the solid-phase is lower than the gas-phase. Therefore, downstream from the nozzle exit plane, the fluid-phase begins to lag the solid-phase and correspondingly there is a transfer of momentum from the solid-phase to the fluid-phase. The higher β, the higher the solid-phase momentum and therefore the lower the decrease in total momentum. This process can be used to explain the results in Figure 5.5 as well as previous findings from Fan et al. [1990] and Wall et al. [1982]. The lag between phases is negligible upstream from the centreline concentration peak; therefore negligible momentum transfer has occurred and all cases have similar profiles (supporting the findings of Fan et al. [1990]). However, downstream from the centreline concentration peak it can be seen that the cases with higher β are elongated. This may be because these cases have higher solid-phase momentum, leading to less flow retardation, thus the elongation of the jet further downstream (supporting the current findings and those of Wall et al. [1982]).

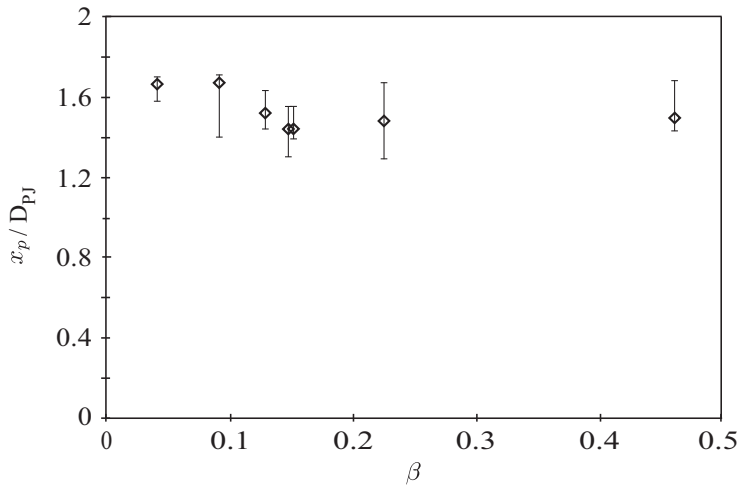

Figure 5.6: Normalised length to the centreline concentration peak (x_p/D_{PJ}) and normalised peak signal ($S'/\overline{S}$) for varying β and $G_{PJ}/G_{ANN(f)} = 6.19$.

The locations of the centreline concentration peaks for $G_{PJ}/G_{ANN(f)} = 6.19$ and varying β are shown in Figure 5.6. The error bars correspond to $\pm 3\%$ variation in signal. It can be seen that the variations in the location of the centreline concentration peak with increasing β are very small compared with the variations with increasing G_{PJ}/G_{ANN} (see Figure 4.9). In Figure 5.6 no distinct trend in the length x_p can be seen for increasing β, other than that the centreline concentration peak appears to be independent from β for the cases investigated where G_{PJ} is high. Again, these results support previous findings that there is little or no influence of β on the distribution of particles immediately downstream from the near-nozzle region [Fan et al., 1990].

The halfwidth profiles of particle concentrations for the range of β investigated are shown in Figure 5.7. The profiles have strong similarities, but it can be seen that increasing β results in a slight narrowing of the jet downstream from the centreline concentration peak. As discussed above, in reference to the normalised axial mean particle distributions (Figure 5.5), the higher β, the higher total momentum. This higher momentum results in less jet spread and thus a narrower jet. The narrowing of a jet with increasing β has previously be shown by Hedman and Smoot [1975] and Wall et al. [1982].

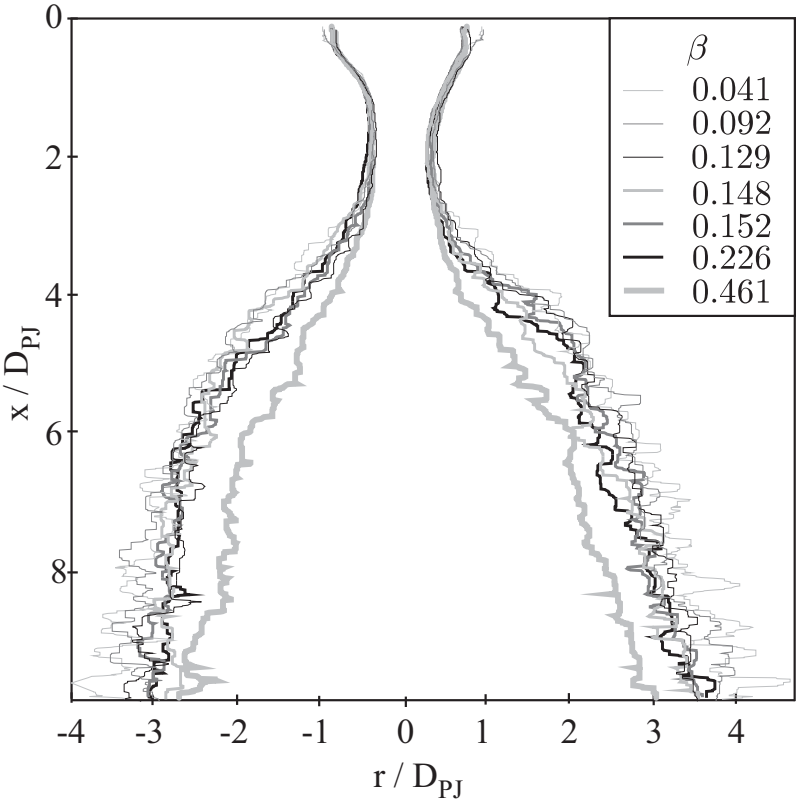

Figure 5.7: Concentration halfwidth profiles for $G_{PJ}/G_{ANN(f)} = 6.19$.

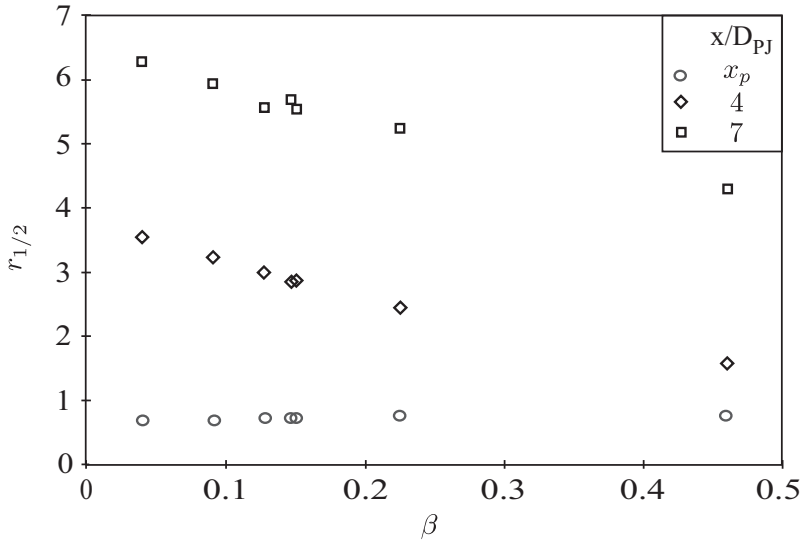

Figure 5.8: Halfwidth at $x/D_{PJ} = x_p$, 4 and 7 for $G_{PJ}/G_{ANN(f)} = 6.19$.

A better understanding of the influence of β on the profiles is given in Figure 5.8. Here the value of the halfwidth, $r_{1/2}$, at $x/D_{PJ} = x_p$, 4 and 7 are shown. Error bars have been omitted for clarity. Here, it is clear that increasing β causes a distinct decrease in $r_{1/2}$ for both $x/D_{PJ} = 4$ and 7, indicating that the jet is elongated with increasing β. At each radial location the relationship between $r_{1/2}$ appears linear for $0.041 \leq \beta \leq 0.461$.

Figure 5.8 also shows that increasing β causes no significant variation to $r_{1/2}$ at $x/D_{PJ} = x_p$. It is evident that β has little influence on the distribution of particles for $x/D_{PJ} \leq x_p$, whereas downstream from the centreline concentration peak, effects are clearly evident: increasing β results in an elongation of the jet.

As discussed above these data are performed for constant $G_{PJ}/G_{ANN(f)} = 6.19$, which implies that G_{PJ}/G_{ANN} varies considerably. To indicate the different roles of β and G_{PJ}/G_{ANN} the halfwidths at $x/D_{PJ} = x_p$, 4 and 7 are presented for varying G_{PJ}/G_{ANN} in Figure 5.9. This allows these data to be compared with those from Chapter 4 obtained at constant $\beta = 0.14 \pm 0.02$. Lines of best fit are used to highlight the major trends.

The results for $G_{PJ}/G_{ANN} \geq 0.18$ and $\beta = 0.14 \pm 0.02$ show an almost linear increase for $x/D_{PJ} = 4$ and 7. There is a corresponding linear decrease for the halfwidths at x_p. The results for $G_{PJ}/G_{ANN(f)} = 6.19$ and variable β at all three axial locations show a remarkable continuation of the existing trends.

Figure 5.10 presents the axial locations at which the centreline concentration downstream from the peak decreases to 90% and 50% of the peak signal. As was the case for the previous figure, the seven cases with $0.00 \leq G_{PJ}/G_{ANN} \leq 4.90$ and $\beta = 0.14 \pm 0.02$ are compared with the seven cases for $0.041 \leq \beta \leq 0.41$ and $G_{PJ}/G_{ANN(f)} = 6.19$. The selection of the concentration values 90% and 50% is arbitrary, but these values provide for a consistent comparison of the two data sets.

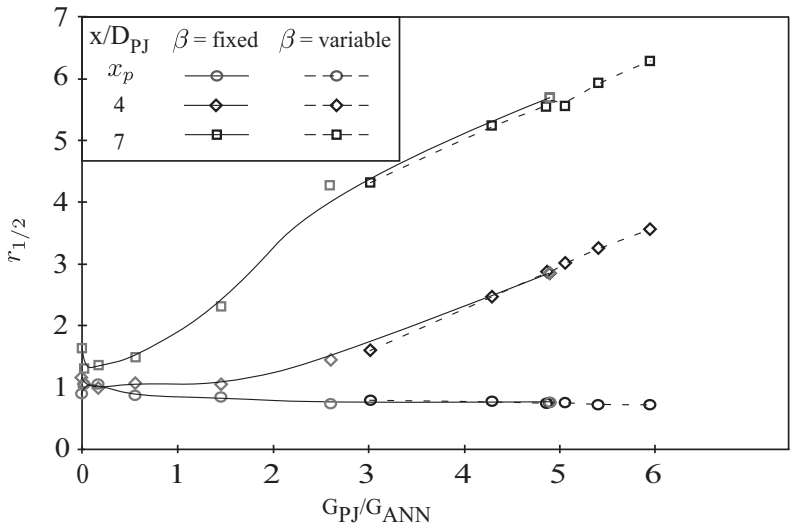

Figure 5.9: Halfwidth at $x/D_{PJ} = 4$ and 7 for β = fixed ($\beta = 0.14 \pm 0.02$) - solid lines, and β = variable ($G_{PJ}/G_{ANN(f)} = 6.19$) - dashed lines.

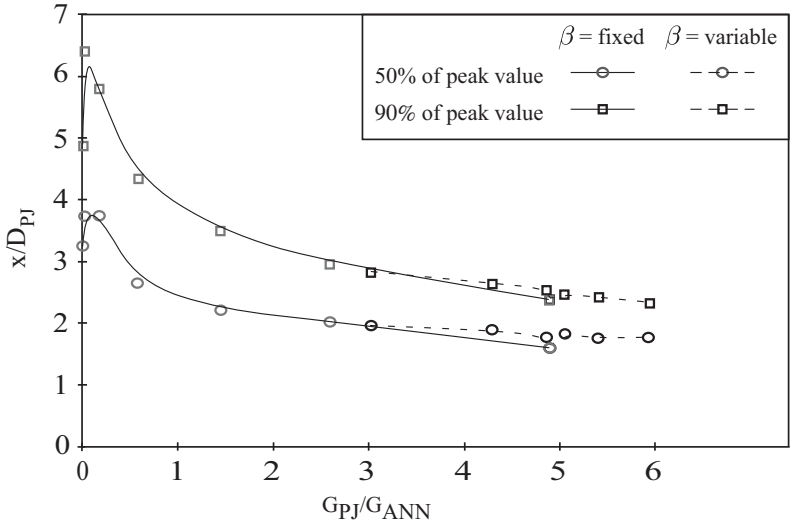

Figure 5.10: Axial locations of the 90% and 50% centreline peak concentration values, downstream from the centreline peak concentration location for β = fixed ($\beta = 0.14 \pm 0.02$) - solid lines, and β = variable ($G_{PJ}/G_{ANN(f)} = 6.19$) - dashed lines.

Assuming that the influence of jet precession on the halfwidths and centreline concentration for $G_{PJ}/G_{ANN} \geq 2.60$ continues in a linear fashion, then these results indicate that the influence of β shown in the current chapter is a result on the increase in the

G_{ANN} rather than the influence of an additional phase to the flow. There is a lot of overlap, and it is very clear that the influence of β is within measurement uncertainty. It is also clear that the influence of β is much less than the influence of G_{PJ}/G_{ANN} over the ranges investigated.

5.3 Conclusions

Measurements have been performed of the influence of β on the mean and fluctuating components of particle distributions in the near-field of a two-phase jet employing a Precessing Jet nozzle. The influence of β on the distribution of particles is small, but not negligible. Upstream from the centreline concentration peak there is little discernible influence of β. These results are supported by previous findings by Fan et al. [1990] that the influence of β is almost negligible at the nozzle exit, as discussed in Subsection 1.4.2. From the centerline profile (Figure 5.5) it can be seen that the decay rate downstream from the centreline concentration peak decreases with increasing β. There is also a narrowing of the jet halfwidth as seen in Figures 5.7 and 5.8. These results show that increasing β results in a narrowing and elongation of the jet downstream from the centreline concentration peak, a finding supported by Wall et al. [1982].

For the investigations into the influence of jet precession of the particle distribution, β varies from $0.120 \leq \beta \leq 0.152$. In this range, the influence of β on the flow in the first 10 nozzle diameters is expected to result in a narrowing and lengthening of the jet. However, compared to that of G_{PJ}/G_{ANN}, the influence of β is minor. It is clearly evident that G_{PJ}/G_{ANN} has a far greater influence on the distribution of particles compared to β.

It should be noted these result may be attributed to the variation in the annular stream momentum, rather than the addition of particles alone, as is indicated from Figures 5.9 and 5.10. However, this is based on the assumption that the variation in results for $G_{PJ}/G_{ANN} > 4.90$ are small, relative to $G_{PJ}/G_{ANN} \leq 4.90$ The implication of these findings is that the transfer of momentum between phases is not significant in the first 10 nozzle diameters downstream. Transfer of momentum between phases, which was explained as the mechanism in the work of Wall et al. [1982] and Fan et al. [1990], may still occur further downstream.

Chapter 6

Particle cluster determination

6.1 Introduction

As discussed in Section 1.3 and 1.5, the instantaneous distributions of particles in two-phase flows are typically non-uniform [Eaton and Fessler, 1994]. This non-uniformity is deduced to be of significance in pulverised fuel (PF) combustion and other processes [Smith et al., 2002]. The formation of regions with high particle concentrations (known as particle clusters) can result in different localised combustion environments, so that the combustion can differ significantly from that which would occur were the local and mean distributions the same [Winkler et al., 2004]. While this issue is well known, no generalised method to measure these effects seems to be available, especially under particle loadings of relevance to PF combustion. There is a need to develop a method to identify and quantify particle clusters, especially under particle loadings of relevance to practical systems.

Previous methods to identify particle clusters from instantaneous planar images comprise individual particle counting, and low-pass filtering. While both methods provide

a means to identify clusters, they are severely limited. For example, particle counting requires the ability to individually identify particles, so that images must be highly resolved. The probability of multiple particles being detected by the array also needs to be low. These requirements limit the total size of the image viewing region and limits particle seeding densities to values much lower than those that occur in practical PF systems. Furthermore, the subsequent determination of a particle cluster requires the use of a threshold to define the edge of a cluster. This threshold value is arbitrary. Particle counting was conducted by Longmire and Eaton [1992], Fessler et al. [1994] and Smith [2000]. While providing valuable information, none of these authors claim to quantify clusters or attempted to provide statistical data, such as cluster locations or size.

Determination of particle clusters by low-pass filtering involves the removal of a minimum particle concentration value from instantaneous concentration images. Individual particles do not need to be identified, and therefore image-viewing regions are not limited in the same way as particle counting. However, a simple low-pass filter also requires an arbitrary threshold to define the edge of a cluster. Unfortunately, such thresholds are rarely reported explicitly. This method was presented using Mie-scattering images of droplets by Zimmer et al. [2002a,b]. In their investigations, they removed the mean signal from the instantaneous image and then applied the threshold.

Figure 6.1 shows the results of cluster determination using a threshold method applied to the difference of the instantaneous image and the mean. Threshold values of 0%, 10%, 20% and 30% of the maximum signal are shown. The case of 0% threshold looks very similar to the instantaneous image. Although this may appear *correct*, statistics from this case show many smaller adjacent clusters rather than single large clusters. Increasing the threshold fails to merge the smaller clusters into large clusters and also fails to identify clusters in regions of low recorded signal strength. This is because the threshold is based on a fraction of the maximum signal. An alternative to a single threshold value is a variable threshold based on, for example, the mean. However, even

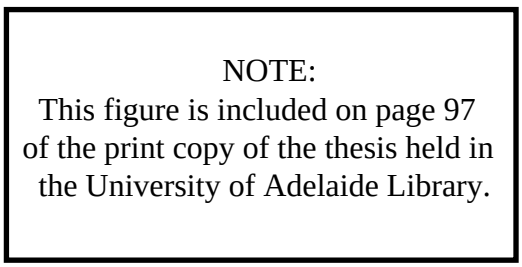

Figure 6.1: Identification of particle clusters for a range of threshold values using the threshold method, (adapted from Zimmer et al. [2002a]).

with this alternative method, the threshold is still arbitrary.

The above methods are hindered by the need to use arbitrary thresholds to determine particle clusters. In so doing, it is not possible to directly compare different research results without prior knowledge of the thresholds. The aim of the current chapter is to develop a more rigorous approach to define and measure particle clusters in jet flows.

6.2 Methodology

An appropriate consistent definition of what constitutes a cluster is required before any attempt to measure them can be attempted. A particle cluster is a region of high local particle concentration. This is relative to a theoretical environment that does not experience the effects of preferential concentration; i.e. a non-preferential distribution. To determine particle clusters, the regions of high local particle concentrations must be compared with the non-preferential distribution. As particle clusters are time dependent, they are not clearly evident in the mean of an ensemble collected over time. Therefore, the non-preferential distribution of particles is approximated as the mean distribution of particles, provided that it does not show physical bias, symmetry, or phase-average periodicity. In most randomly sampled turbulent flows, the mean particle distribution is the most justifiable definition of non-preferential distribution.

Prior to a direct comparison between the instantaneous image and the non-preferential distribution, the instantaneous image needs to be converted from an array of discrete quanta into a pseudo-scalar field. This array of discrete quanta stems from the pixels of the recording CCD and the fact that the flow of particles is not a continuum. A pseudo-scalar field is generated by smoothing the instantaneous image by an appropriate scale, L. The selection of L is very important and discussed in the next section.

The mean image (representing a non-preferential distribution) is subtracted from the pseudo-scalar field. This highlights the differences between instantaneous structures and the theoretical non-preferential distribution of particles. The positive values of the difference are converted to binary form to generate a *Cluster Mask*. The cluster mask is a representation of where the instantaneous image has higher concentrations than the mean. However, due to the smoothing applied to the instantaneous image to generate the pseudo-scalar field, it is possible that the cluster mask includes regions of the flow that in fact do not have particles. Therefore, the cluster mask is multiplied by the original instantaneous image to provide an image of particle clusters, known

as a *Cluster Map*. Although the process is not complex, it removes the need for an arbitrary value, as has been used previously to identify particle clusters [Longmire and Eaton, 1992, Zimmer et al., 2002a,b].

Figure 6.2 shows the stages of the methodology. Here an instantaneous image (A) is smoothed by L to form the pseudo-scalar field (B). (For this example the smoothing was by a Gaussian algorithm with a diameter equal to half the central jet diameter, as explained in Section 2.4). The mean image (C) represents the non-preferential distribution. The positive values of the difference between image B and image C are converted into a binary form to produce the cluster mask (D). A cluster map (E) is produced by multiplying the cluster mask (D) with the instantaneous image (A). Image (F) is the gradient of the cluster mask (E) superimposed over the instantaneous image (A).

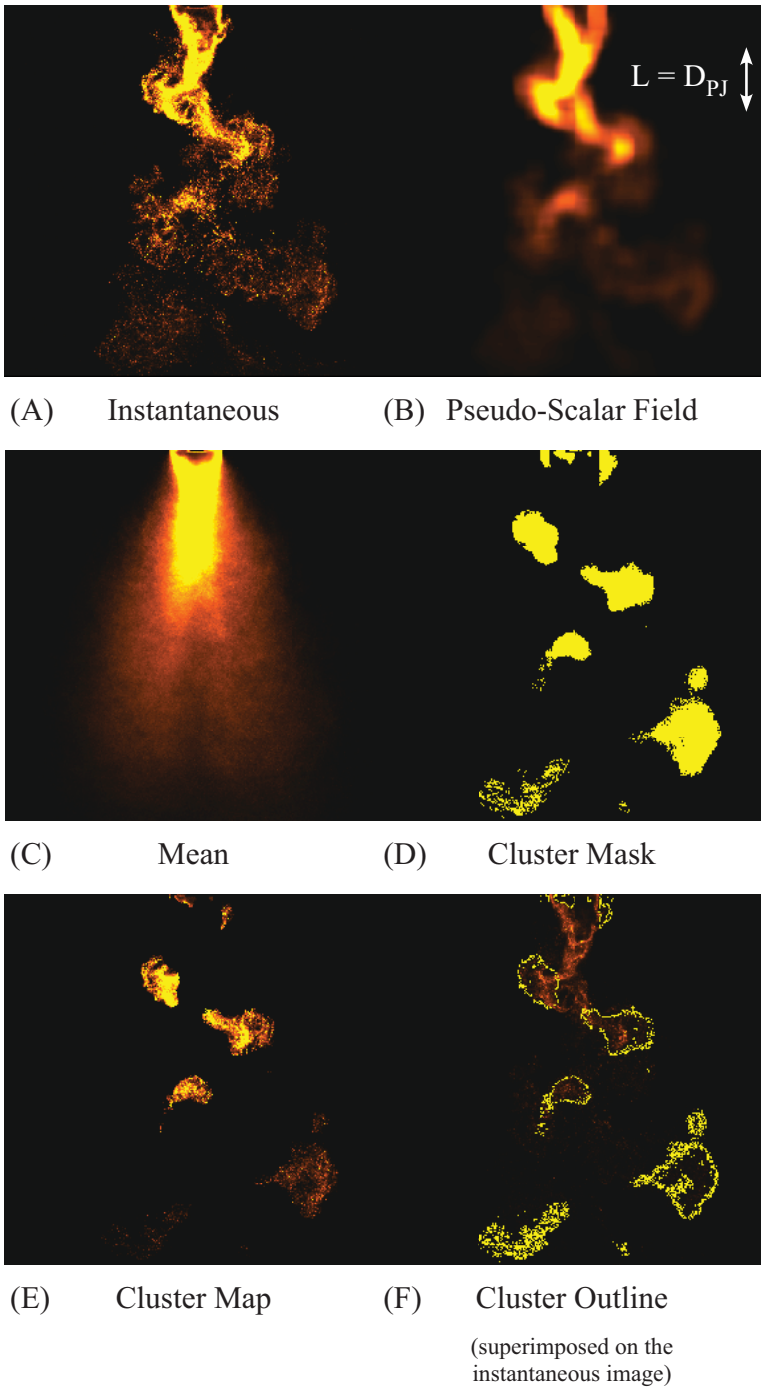

Figure 6.2: Stages of the methodology used to identify particle clusters.

6.3 Sensitivity of cluster identification to the smoothing value

The proposed method is subject to the amount of smoothing of the instantaneous image to generate the pseudo-scalar field. To achieve the aim of the current chapter, a sensitivity study of the smoothing value (L) on the methodology is presented. For the current work L has been selected to be a constant multiple of the central nozzle diameter, D_{PJ}, and a Gaussian smoothing algorithm has been used. Although the large-scale turbulent structures in a jet flow are not constant length, the selection of D_{PJ} as a base is used because D_{PJ} can characterises the large-scale turbulent structures within a jet flow, and therefore also the large-scale clusters. To assess a suitable value of L, both visual inspection and statistical analysis of the sensitivity of the results to a systematic variation in the value of L is performed. The methodology presented here is applied to images of particle distributions obtained by planar nephelometry, as described in Section 3.2. For the statistical analysis the data ensemble was made from 202 images with $\beta = 0.148$ and $G_{PJ}/G_{ANN} = 4.90$.

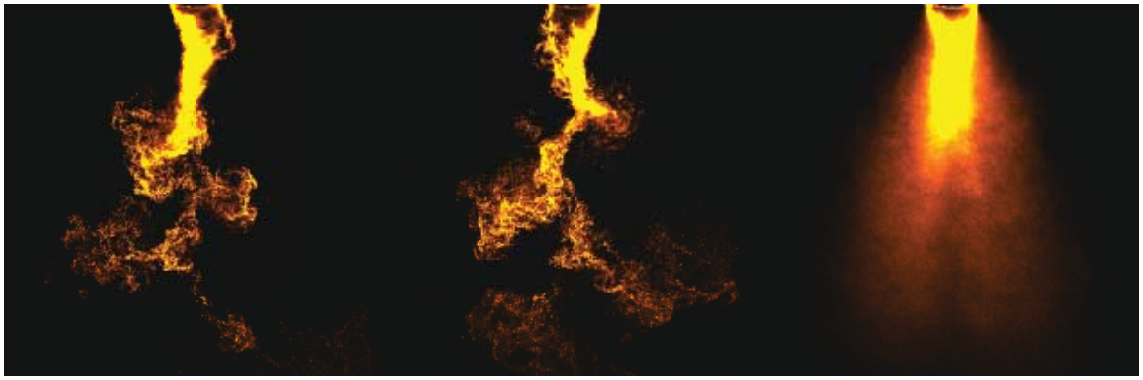

Figure 6.3: Two instantaneous and one mean image of particle distributions emerging from a Precessing Jet nozzle.

Figure 6.3 presents examples of instantaneous images and the corresponding mean image of the particle distributions emerging from a PJ nozzle. A false colour map is used with scales set to highlight the flow structures. The nozzle exit is at the top of

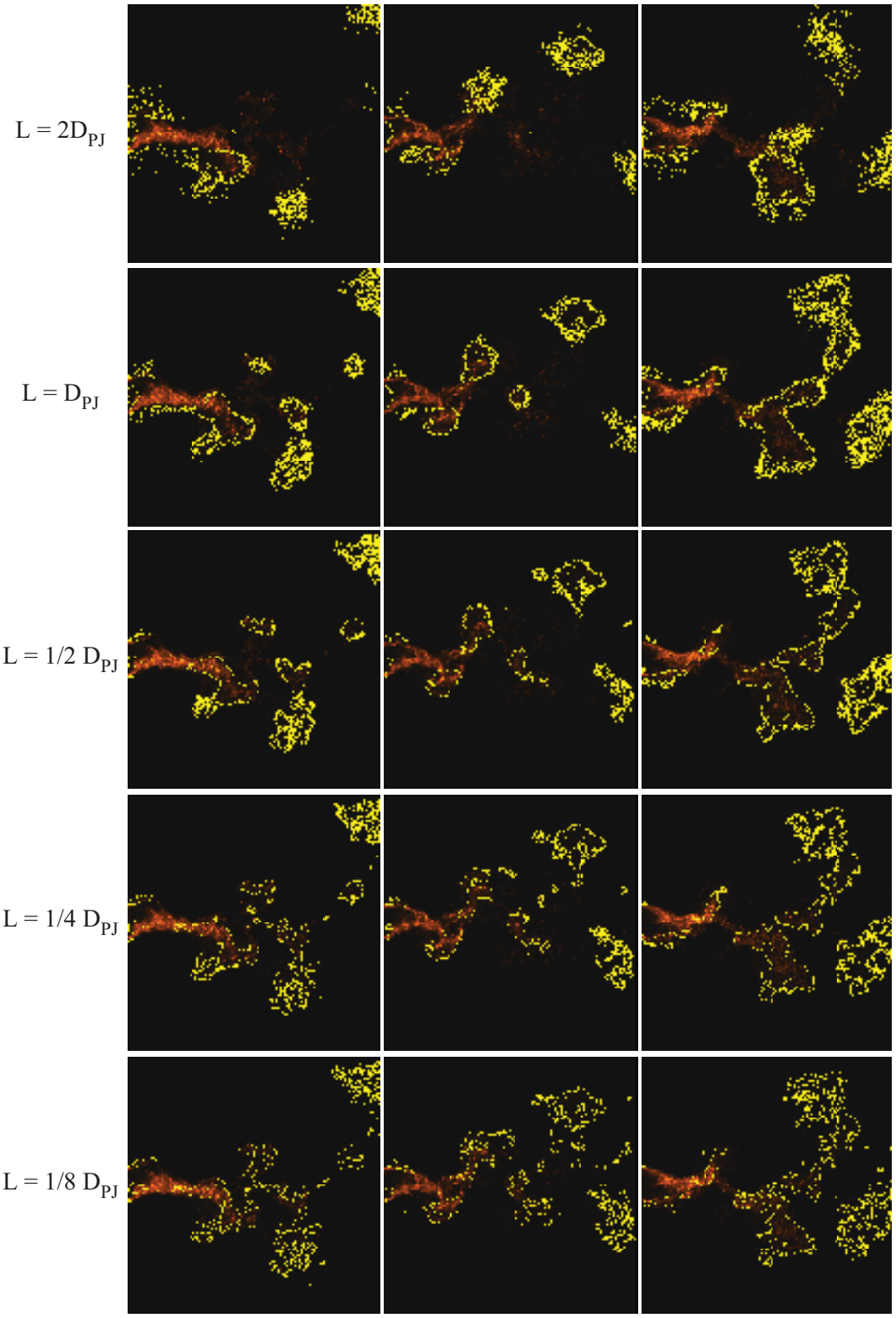

Figure 6.4: Identified clusters superimposed on three different instantaneous images of particle distributions. The value of the smoothing parameter, L, is indicated for each row.

the individual images, and the flow is moving downwards. It is clearly evident that the mean and instantaneous images are different. The mean and fluctuating flow fields produced by the PJ nozzle are discussed in detail in Chapter 4. The instantaneous flow field is discussed in Chapter 7.

Figure 6.4 shows the edges of clusters identified from cluster maps for five smoothing values ($\frac{1}{8}D_{PJ} \leqslant L \leqslant 2D_{PJ}$, ranging by factors of two) and three instantaneous images. The edges of the identified clusters are superimposed on the instantaneous images. In general, the identified clusters correspond reasonably well with visual inspection, and there are only small variations in the identified clusters for different values of L. The small values of L result in the identification of more small clusters and the boundaries of these clusters are distinct. With increasing values of L the identified clusters get smaller and the boundary of the clusters becomes less well defined. However, there are more identified clusters immediately downstream from the nozzle exit plane and along the jet boundary, and these clusters become larger with increasing L. For the highest value of L investigated, very few clusters are identified along the nozzle centreline and some of the more obvious clusters are not identified at all.

For $L = 2D_{PJ}$ there are a number of clusters that are not clearly identified. There are also clusters identified in the near field that do not appear to be clusters from visual inspection. It is apparent that there is an upper limit to the selection of L. When L is too small, many small clusters are identified and some single clusters are identified as smaller multiple clusters. Figure 6.5 shows some of the effects of L for regions from two separate instantaneous images. The region on the left hand side of the image is approximately $4D_{PJ}$ wide and $2.3D_{PJ}$ high. It is located approximately $5.4D_{PJ}$ downstream from the nozzle exit plane and the right edge of the region is near to the nozzle centreline. The other region is approximately $4D_{PJ}$ wide, $4.1D_{PJ}$ high, located approximately $3.3D_{PJ}$ downstream from the nozzle exit plane and the right edge is also near to the nozzle centreline. In the first instantaneous image (sequence on the left hand side of the figure) when $L = \frac{1}{8}D_{PJ}$, a single large cluster is clearly

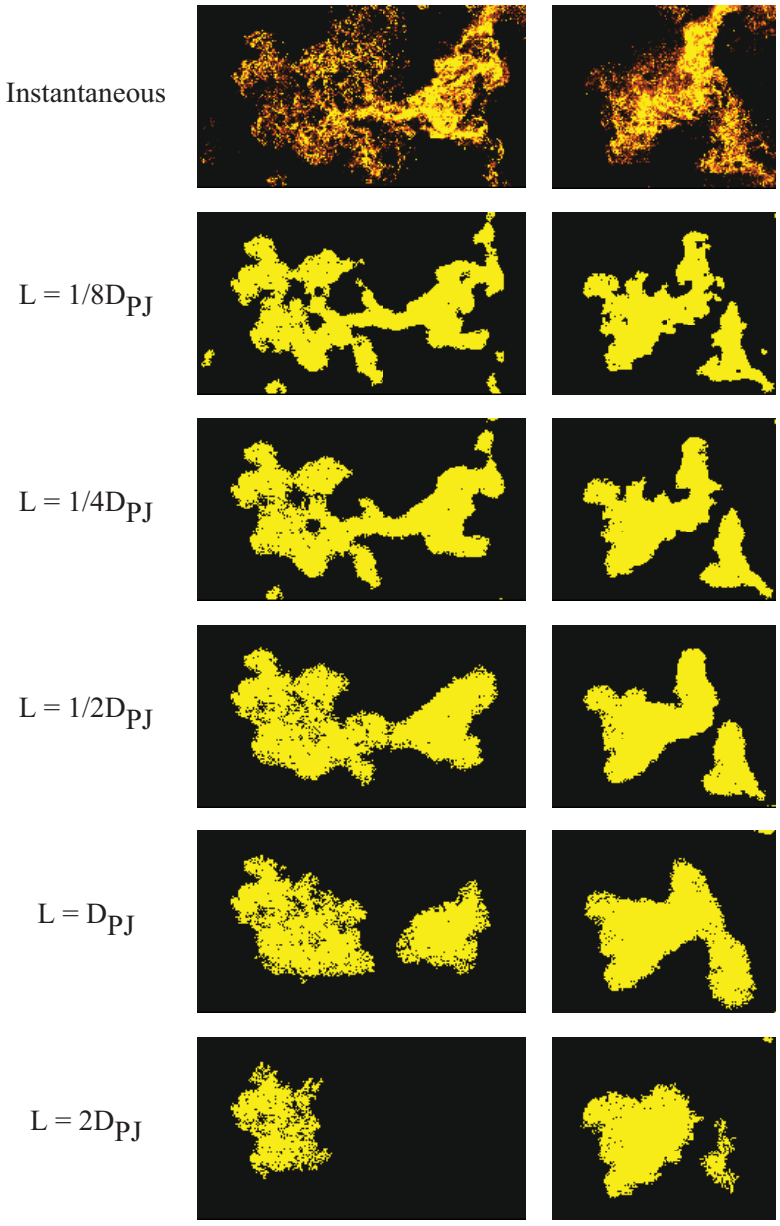

Figure 6.5: Typical examples of the influence of L on the shape of each cluster identified from two images.

identified, but there are also numerous smaller clusters surrounding it. Increasing L causes the surrounding clusters to either fade or merge; for this example, only the closest of surrounding smaller clusters merge, the remainder fade and are no longer identified. When $L = D_{PJ}$ it can be seen that the single cluster divides into two clusters. This is followed by a cluster not being identified at all when $L = 2D_{PJ}$. For $L = \frac{1}{8}D_{PJ}$ the second instantaneous image (right of the figure) shows two large clusters. With increasing L these two clusters merge (at $L = D_{PJ}$), but again divide with a further increase in L. From these two examples, it is evident that there is a strong variation in the shape of the identified clusters for the range of L investigated. These examples clearly highlight the sensitivity of the measured shape of a cluster to the upper limit of L and, to a lesser extent, the lower limit of L.

When L is large (e.g. $L = 2D_{PJ}$), the smoothed instantaneous image (pseudo-scalar field) becomes less distinct. This pseudo-scalar field becomes increasingly similar to the mean image, and consequently the difference between the two (on which clusters are defined) is very small. Near to the nozzle exit plane and for large L, interpixel noise is incorporated into the cluster identification, hence many small clusters are identified. Further downstream, the similarities between the pseudo-scalar field and the mean image result in the merging of clusters. However, for subsequent increases in L, the increasing similarities between the smoothed and mean results in clusters dividing and failure to identify clusters appropriately. When L is small, the pseudo-scalar field is similar to the instantaneous image. Interpixel noise and individual isolated particles can appear as clusters. Single large clusters can also appear as a collection of smaller adjacent objects.

A general understanding of the influence of L on the cluster identification can be obtained from an assessment of the average area ($\overline{A_c}$) and average number ($\overline{N_c}$) of clusters per instantaneous image for the entire ensemble. These results are shown in Figure 6.6. With an increase in $\frac{1}{8}D_{PJ} \leq L \leq \frac{1}{2}D_{PJ}$ there is a decrease in $\overline{N_c}$ per image, but a corresponding increase in $\overline{A_c}$. This results from the merging of adjacent clusters.

The product of $\overline{A_c}$ and N_c is the total area of clusters per image, A_{total}. This value also increases with $\frac{1}{8}D_{PJ} \leq L \leq \frac{1}{2}D_{PJ}$.

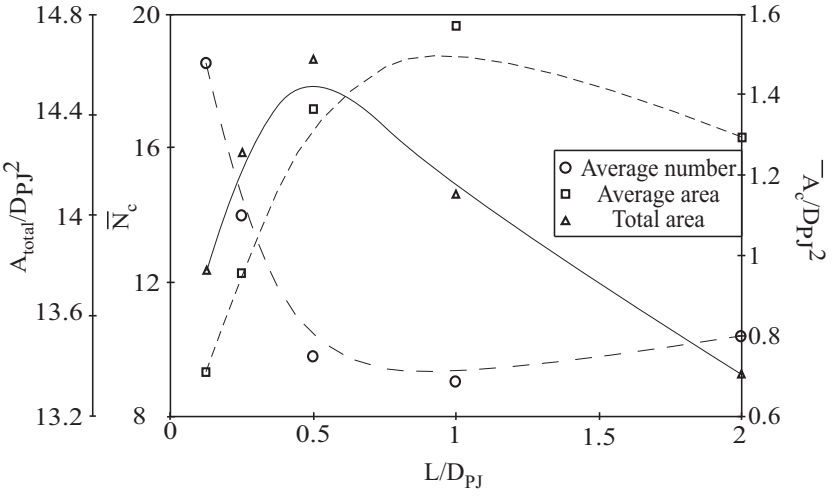

Figure 6.6: A plot of $\overline{A_c}$, $\overline{N_c}$ and A_{total} per image for varying L.

It is interesting that $\overline{A_c}$ and A_{total} both peak at $L \approx D_{PJ}$. For $L \geq D_{PJ}$, $\overline{N_c}$ increases slightly and both areas decrease. This may indicate that values of $L \geq D_{PJ}$ corresponds to too much smoothing of the clusters, causing a splitting of some clusters into smaller clusters. Over smoothing of data and failing to identify clusters provides a plausible explanation for why A_{total} in Figure 6.6 decreases at a very high rate, but $\overline{N_c}$ increases only slightly.

To quantitatively demonstrate the influence of L on the formation of clusters, probability density functions (PDFs) of both axial and radial locations of cluster centroids, number of clusters per image, the equivalent cluster diameter (d_{eq}) and cluster perimeter (P_c) have been analysed. The PDFs are based on varying L for each instantaneous image of an ensemble of 202 images. Spline curves are fitted to each case to identify the dominant trends.

The analysis is limited to clusters with area, A_c, greater than 100 pixels ($A_c > \frac{D_{PJ}}{10} \times \frac{D_{PJ}}{10}$ where A_c is determined using planar nephelometry). Objects smaller than 100 pixels approach the size of a single particle imaged on the CCD. These objects are excluded

as they are not the focus of the current investigation. In terms of the influence of particle clusters in PF fired systems, clusters with $A_c < \frac{D_{PJ}}{10} \times \frac{D_{PJ}}{10}$ contain little of the total available fuel and therefore their combustion influences are expected to be minor compared with that of larger sized clusters. Furthermore, computational time is also reduced by excluding these sized clusters.

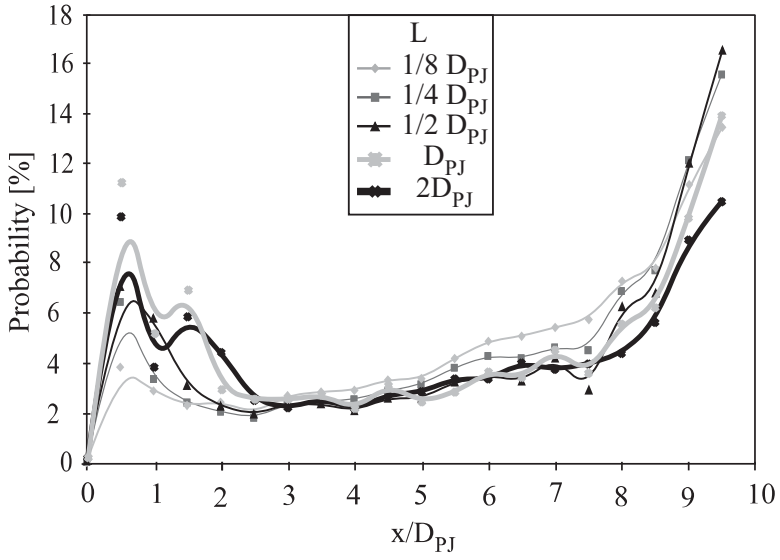

Figure 6.7: PDF of the axial location of clusters centroids identified for varying L.

The PDFs of the axial locations of cluster centroids are presented in Figure 6.7. They show sensitivity to the selection of L. Between $0 < x/D_{PJ} < 3$ all cases have a peak. In general this peak becomes higher and wider with increasing L. Between $3 \leq x/D_{PJ} \leq 8$ all cases show a gradual increase in probability with axial distance from the nozzle and this gradient is insensitive to L. For $8 < x/D_{PJ} < 10$ all cases show a rapid increase in gradient. Intermediate values of L have the largest peak.

It should be noted that statistics obtained from clusters near to the physical boundary of images will most likely contain the greatest errors. This results from clipping of clusters and thus identifying partial clusters. Identification of partial clusters results in lower average areas, diameters and perimeters, as well as incorrectly locating the cluster centroids, and increasing the number of cluster centroids identified in this region. This

can be seen in Figure 6.7 with the increase in the gradients for $x/D_{PJ} \geq 9$ for all values of L.

The peaks in the PDFs of the axial locations of cluster centroid in the range $0 < x/D_{PJ} \leq 3$ are a result of over smoothing, and thus identifying numerous small clusters near to the jet edge. This is clearly seen in Figure 6.4.

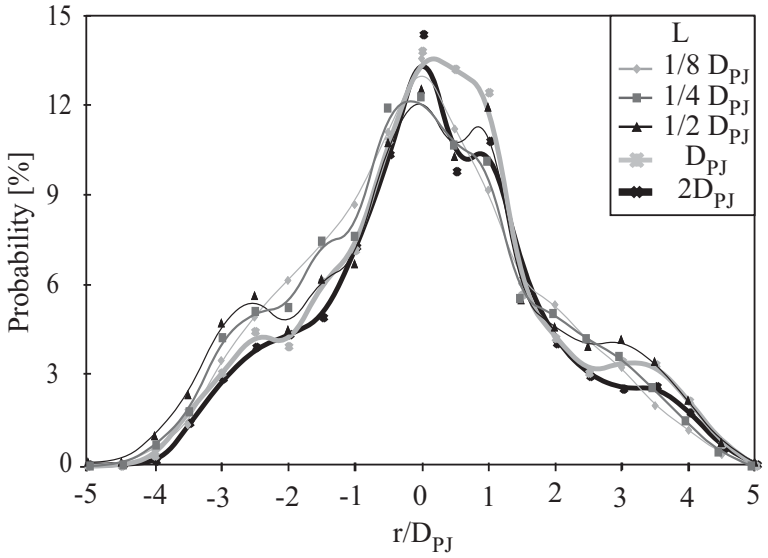

Figure 6.8: PDF of the radial location of clusters centroids identified for varying L.

The PDFs of the radial locations of the centroids of the identified clusters are shown in Figures 6.8 for $0 < x/D_{PJ} < 10$. The PDFs of the radial locations have an approximate Gaussian profile, centred on the jet axis. The deviations between profiles are less than 4% for the values of L investigated. These results indicate an independence from L.

Figure 6.9 shows the PDF of the radial locations of the centroids for cluster centroids located in the limited axial range ($3 \leq x/D_{PJ} \leq 7$). The results avoid over smoothing of all radial locations and therefore highlights possible influences of L on clusters near to the edge of the jet. Using this limited axial range also excludes possible erroneous data from clipping near to the downstream edge of the image and possible anomalies from particle cluster data near to the nozzle exit plane. Nonetheless, the radial locations of

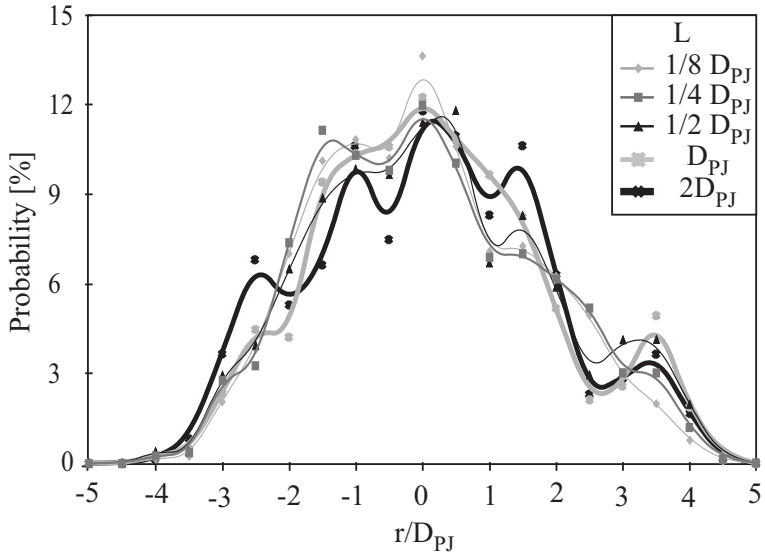

Figure 6.9: PDF of the radial location of clusters centroids identified in the limited axial range ($3 \leq x/D_{PJ} \leq 7$) for varying L.

the cluster centroids from the limited axial range show very similar trends as in Figure 6.8. The PDF profiles for the limited range show greater variations, but this results from the much smaller ensemble size (a reduction of over 50%).

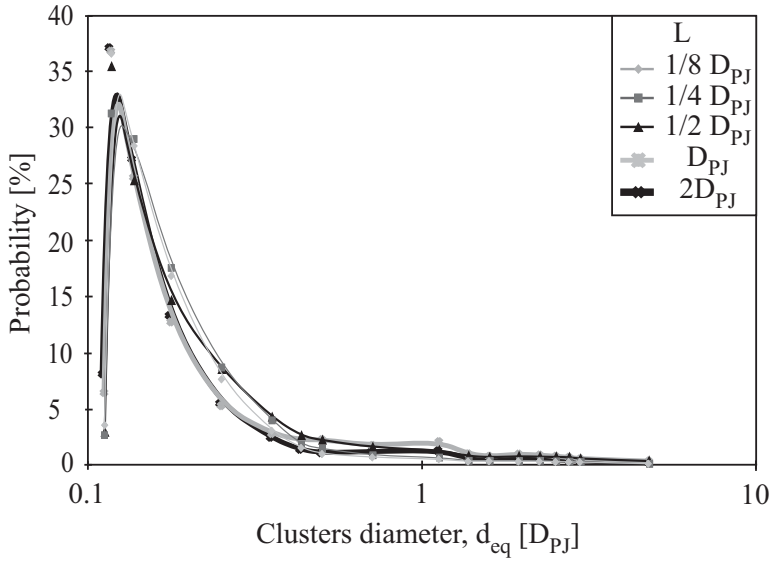

Figure 6.10: PDF of equivalent diameters, d_{eq}, for clusters identified for varying L.

Figure 6.10 shows the PDFs of d_{eq}, for varying L. Here, d_{eq} is the diameter of a circle of the same area as the cluster. This parameter is a function of cluster area, A_c. It can be seen that the profiles are very similar, with differences in the most probable value of d_{eq} varying by less than 5%. That is, the PDFs of d_{eq} are independent from L, indicating that the influence of L on d_{eq} is consistent for all d_{eq}.

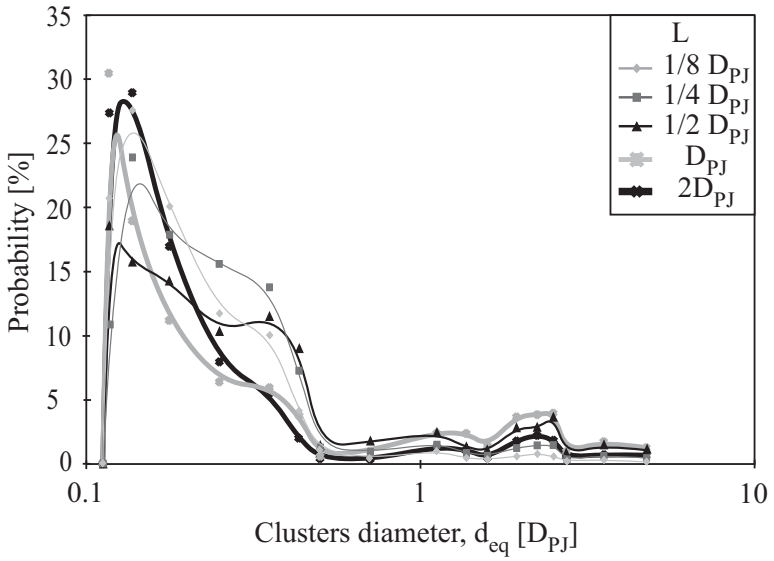

Figure 6.11: PDF of equivalent diameters, d_{eq}, for clusters identified in the limited axial range ($3 \leq x/D_{PJ} \leq 7$) for varying L.

Figure 6.11 shows the PDFs of d_{eq} in the limited axial range for varying L. There is greater variation in the profiles compared to the non-limited axial range, but this is due to the lower sample size. In general, the profiles all show strong similarity to each other

Figure 6.12 is a plot of the average value of d_{eq} ($\overline{d_{eq}}$) with varying L for the entire image as well as the limited axial range of $3 \leq x/D_{PJ} \leq 7$. Since $d_{eq}^2 \propto A_c$, it is not surprising that the profile of this plot is similar to the $\overline{A_c}$ shown in Figure 6.6. However, it is presented to show that d_{eq} is dependent on L. Combined with the information in Figure 6.10 it is suggested that for $\frac{1}{8}D_{PJ} \leq L \leq D_{PJ}$ increasing L increases d_{eq}, but at the similar rate for clusters of all sizes (and therefore all d_{eq}). It should be noted that

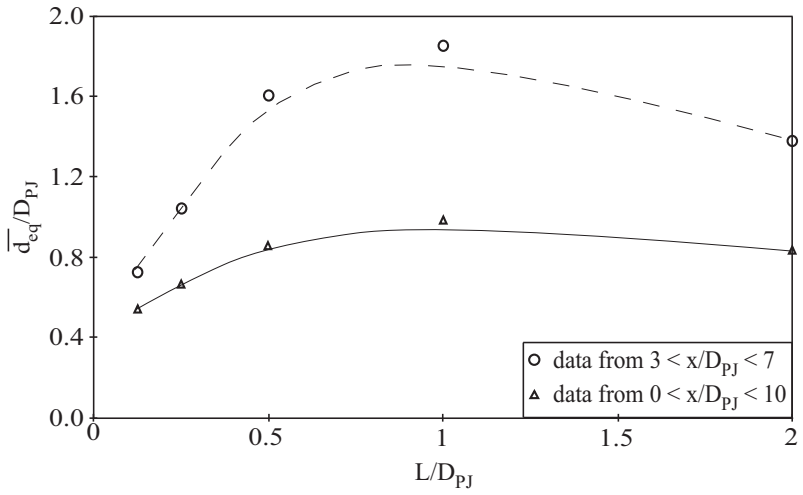

Figure 6.12: A plot of $\overline{d_{eq}}$ per image for varying L for clusters in the region $x/D_{PJ} < 10$ (solid lines) and $3 \leq x/D_{PJ} \leq 7$ (dashed lines).

the difference in profiles due to the limitation in axial range results in an increase in $\overline{d_{eq}}$ for all L. This increase is a result of removal of smaller clusters which, as seen in Figure 6.4, typically occur immediately downstream from the nozzle exit. The increase in $\overline{d_{eq}}$ is greatest for $\frac{1}{2}D_{PJ} \leq L \leq D_{PJ}$. For the case $L = \frac{1}{8}D_{PJ}$, the small increase in $\overline{d_{eq}}$ indicates that a large number of smaller clusters are still being identified.

Figure 6.13 shows the PDFs of P_c. The most probable value of P_c is generally independent of L, although the peak does become narrower with increased L. Nonetheless, the dominant peak for each case is reliably identified for variation in L over an order of magnitude. A secondary peak is also evident for $L = D_{PJ}$ and $2D_{PJ}$. For $L = 2D_{PJ}$ the peak is a singular point at $P_c \approx 5$ of unusually high probability. However, for $L = D_{PJ}$ there are four consecutive points that are approximately double the values determined for smaller L.

The profiles of the PDFs of P_c for the limited axial range of $3 \leq xD_{PJ} \leq 7$ are shown in Figure 6.14. The profiles all show maximum peaks in probability density. The secondary peak for the two highest cases of L are not present, although there is a weak trend that the peak probability occurs at higher P_c for increasing L.

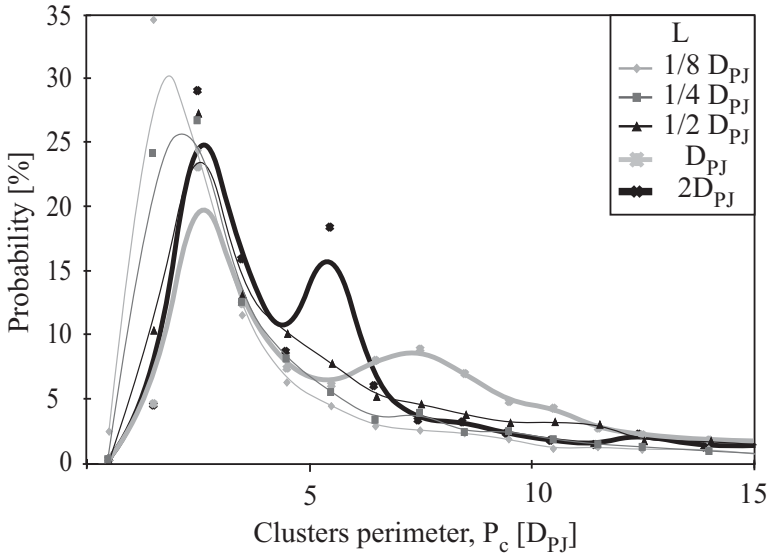

Figure 6.13: PDF of the perimeters of clusters, P_c, identified for varying L.

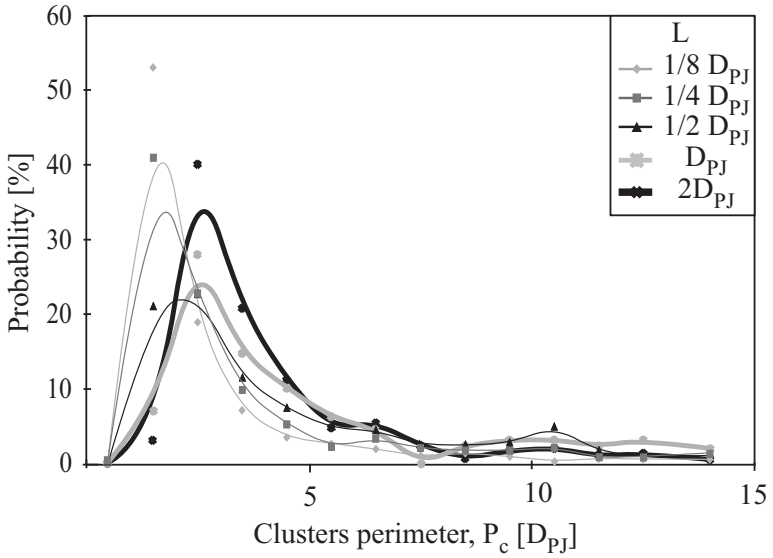

Figure 6.14: PDF of the perimeters of clusters, P_c, identified in limited axial range ($3 \leq x/D_{PJ} \leq 7$) for varying L.

The profiles of the PDFs of P_c for the range $0 < x/D_{PJ} \leq 3$ are shown in Figure 6.15. In this region of the flow it is evident that low values of L identify a greater proportion of clusters with $P_c \leq 3$ than clusters of any other P_c. For the higher values of L (i.e.

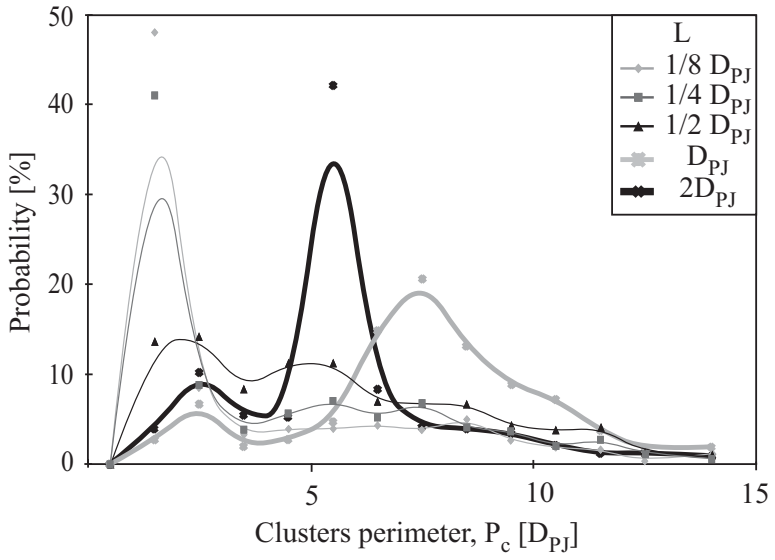

Figure 6.15: PDF of the perimeters of clusters, P_c, identified in the region $0 < x/D_{PJ} \leq 3$ for varying L.

$L \geq D_{PJ}$) there is a greater proportion of larger clusters identified. Consequently, in the superposition of the PDFs from the region $0 < x/D_{PJ} \leq 3$ with the remainder of the image, the secondary peak is generated.

Figure 6.16 presents PDFs of the number of clusters identified for varying L. This parameter is the most sensitive to variations in L. As expected, increasing L will reduce the number of clusters identified. As described by Birzer et al. [2008a,b], increasing the amount of smoothing causes adjacent clusters to merge more often than it causes single clusters to divide. Nevertheless, for $\frac{1}{2}D_{PJ} < L < 2D_{PJ}$, all identify the same dominant peak finding about eight clusters to be the most probable value. This is quite different to the cases $\frac{1}{8}D_{PJ} < L < \frac{1}{4}D_{PJ}$, which identify the dominant peak at about twice this value. Once again, the measured values are not particularly sensitive to$L$ over a reasonable range, and the case $L = \frac{1}{2}D_{PJ}$ is probably close to optimal.

The sensitivity of L on the cluster characteristics as assessed above indicates that there is a possibility that this method may enable preferential identification of clusters based

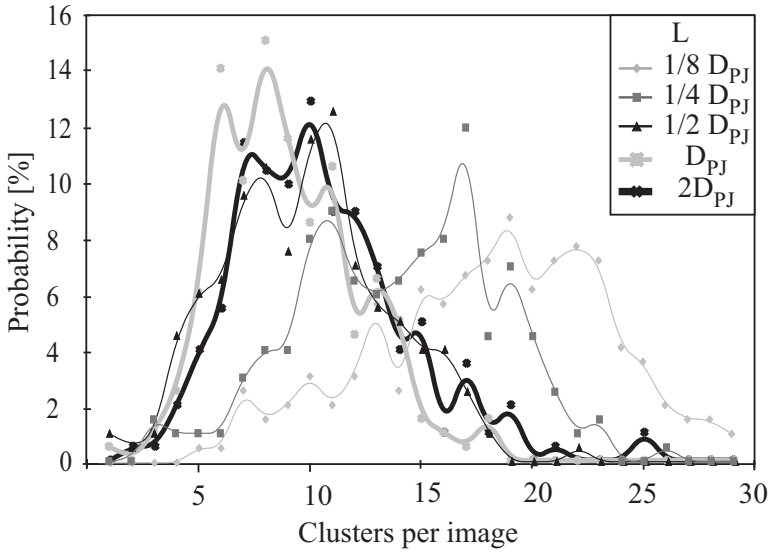

Figure 6.16: PDF of the number of clusters identified for varying L.

on size. It is clear that the higher values of L identify clusters with higher P_c (Figure 6.15). It is also clear from $\overline{A_c}$ and $\overline{N_c}$ per image that the lower values of L investigated identify more clusters, but these clusters have much smaller area (Figure 6.6). In Figure 6.4 for $L = 2D_{PJ}$ only the largest of the clusters are actually identified, whereas for $L = \frac{1}{8}D_{PJ}$ there are many more, but smaller clusters. These results indicate that larger values of L can be used to identify larger clusters and vice versa. However, a great deal more study is required to provide sufficient evidence that this possibility is probable. This undertaking is beyond the scope of the current work.

It should be noted for all the PDFs, the ensembles of each case only consisted of 202 images. This may be considered a low number for statistical analysis. To determine the statistical independence of the size of the ensembles used, a comparison of results from reduced ensemble sizes has been conducted. Figure 6.17 shows the PDFs of the number of clusters identified for $G_{PJ}/G_{ANN} = 4.90$ and $\beta = 0.148$, but for ensemble sizes of 50, 100, 150 and 200 images. The PDF of cluster numbers has been selected as this cluster characteristic typically shows the greatest sensitivity to L. Although the profiles are not identical, they do show strong similarities. The PDFs of the 200

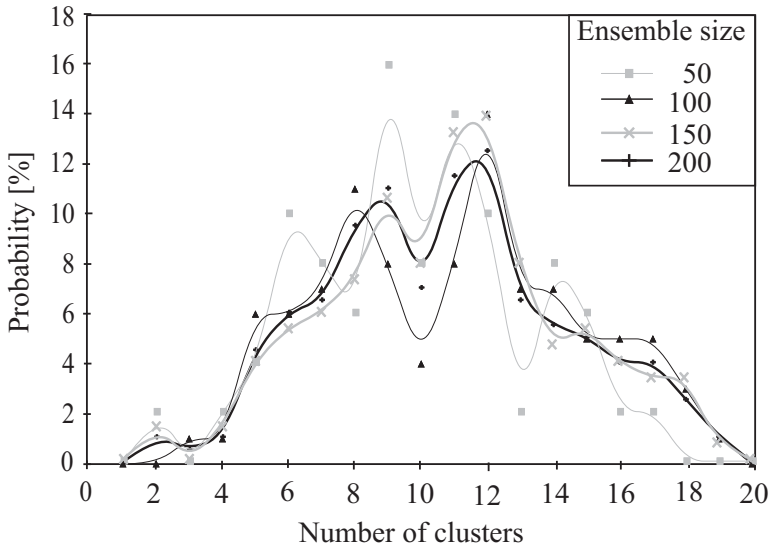

Figure 6.17: PDF of the number of clusters for varying ensemble size.

image case and the 150 image case are very strong. The maximum variance for these profiles is less than 1%. This small variation in results for the case of 150 images and the case of 200 images indicates that, although the sample size is too small to be fully converged, the expected errors due to the ensemble size of 202 images is less than 5%.

6.4 Conclusions

A method to identify particle clusters from planar images of instantaneous particle distributions in two-phase jet flows is presented. The method employs smoothing of instantaneous particle scatter images by a length-scale, L, to produce scalar fields of particle distributions. The scalar fields are compared with ensemble-averaged images to produce cluster masks that are then overlaid on the original instantaneous image to produce a map of the cluster locations. A rigorous assessment of the cluster determination methodology has been performed via a sensitivity study of the influence of choice of the smoothing value, L, on the identified clusters and their characteristics. These characteristics are the average area ($\overline{A_c}$) and average number ($\overline{N_c}$) of clusters per instantaneous image, the cluster perimeter (P_c), the equivalent cluster diameter (d_{eq}), the axial and radial locations of the cluster centroids, and the number of clusters identified.

For this assessment, L has been chosen to be constant throughout the image and to be typical of large-scale flow structures in the flow, so was varied from $\frac{1}{8}D_{PJ}$ to $2D_{PJ}$. From visual inspection it was found that there is a moderate degree of sensitivity to the selection of L. Increasing L leads to an increase in $\overline{N_c}$ and $\overline{A_c}$ for clusters identified in regions that correspond to high fluctuations in the particle distributions, notably at the jet edge. If L is too large, clusters in areas that correspond to low fluctuations in the particle distributions (i.e. jet centreline) are not well identified. The boundaries of identified clusters are also less distinct with large values of L. On the other hand, if L is too small, many small clusters are identified. These smaller features are not the subject of the present investigation as they are less likely to influence combustion compared with the larger clusters, as discussed previously in this Chapter.

From PDFs, it was found that none of the features are particularly sensitive to the choice of L, over the range $\frac{1}{2}D_{PJ}$ to D_{PJ}, which gives confidence in the approach when used for the current nozzle configurations investigated. The PDFs of cluster diameters

and radial location of centroids are particularly insensitive to the choice of L, whereas the number of clusters, cluster perimeters and the axial locations were found to be most sensitive to the choice of L. However, in all cases, $L = \frac{1}{2}D_{PJ}$ was found to avoid the problems of either over-smoothing or under-smoothing, suggesting that this is near to the optimal value for this investigation. The influence of the selection of L on the cluster determination results is as follows.

Very small values of L (e.g. $L \leq \frac{1}{8}D_{PJ}$) will:

- Split single clusters into many small objects.

Small values of L (e.g. $\frac{1}{8}D_{PJ} < L \leq \frac{1}{4}D_{PJ}$) will:

- Result in the identification of more small clusters; and
- Generate distinct boundaries around clusters.

Large values of L (e.g. $\frac{1}{2}D_{PJ} \leq L \leq D_{PJ}$) will:

- Cause identified clusters to become smaller;
- Fail to identify small clusters;
- Generate "fuzzy" boundaries around clusters;
- Identify more clusters at the exit; and
- Identify more clusters at the jet edge.

Very large values of L (e.g. $L > D_{PJ}$) will:

- Cause clusters identified near to the exit and jet edge to get larger;
- Identify less clusters along centerline;
- Fail to identify some obvious clusters; and
- Generate "fake" or "spurious" clusters near the nozzle exit plane.

For the current work, in the near-field and transition regions of the jet, the optimal value appears to be $L = \frac{1}{2}D_{PJ}$ based on results from both analysis techniques. There is a degree of tolerance in the selection of L such that small variations will not alter the results significantly. In the far-field, where large-scale flow structures increase in size, the value of L would need to be larger. For this reason, a variable value of L (e.g. a function of x/D_{PJ}, where x is the downstream distance) may be desirable for investigations further downstream.

The results indicate that the method can be used successfully to identify particle clusters in planar images of particle concentration or distributions. This will enable statistical analysis to be employed to assess particle clusters, e.g. size, location, general shape and orientation. These results give confidence that the method can be used successfully to identify large-scale particle clusters in planar images of particle concentration or distributions with this configuration. There is also potential that this methodology can be used in many different flow fields and for different scale clusters. However, this will need to be assessed. To enable statistical analysis to be employed to assess particle clusters, e.g. size, location, general shape and orientation a variety of jet flows, further investigations are still required. The method presented in this chapter is used in Chapters 7 and 8. These findings have also been reported by Birzer et al. [2008a,b].

Chapter 7

Influence of jet precession on particle clusters

7.1 Introduction

In Chapter 4 the influence of G_{PJ}/G_{ANN} on the mean and fluctuating components of the distribution of particles was presented. The results from that chapter show that small values of $G_{PJ}/G_{ANN} > 0$ result in an elongation of the mean particle distribution, but greater amounts of G_{PJ}/G_{ANN} result in a wider and shorter mean particle distribution. Increasing G_{PJ}/G_{ANN} also causes an increase in the relative fluctuations in the particle distributions.

These findings provide useful details of the time averaged distribution of particles emerging from a particle-laden Precessing Jet. It is hoped that these results will be used for improvements to PF combustion system designs. However, the instantaneous distribution of particles is also important to combustion systems and therefore must be explored to enable even further improvements to PF combustion system designs.

The aim of the current chapter is to ascertain how G_{PJ}/G_{ANN} influences the formation of particle clusters in the first 10 nozzle-diameters of the flow. Clusters are identified using the methodology outlined in Chapter 6, with smoothing value of $L = \frac{1}{2}D_{PJ}$. The clusters analysed have been classified as either *small-clusters* or *large-clusters* and these are based on cluster area, A_c (as determined using planar nephelometry). Small-clusters are defined to have A_c ranging from approximately $\frac{1}{10}D_{PJ} \times \frac{1}{10}D_{PJ} \lesssim A_c \lesssim D_{PJ} \times D_{PJ}$ (100 pixels $\leq A_c <$ 10,000 pixels). Large-clusters have $A_c \geq D_{PJ} \times D_{PJ}$ ($A_c \geq$10,000 pixels). As the size of particle clusters influences combustion in different ways [Zhang and Wall, 1993], assessing both small- and large-clusters separately is desirable. As explained in Chapter 6, objects smaller than 100 pixels are excluded as they are not the focus of the current investigation. In terms of the influence of particle clusters in PF fired systems, clusters with $A_c < \frac{1}{10}D_{PJ} \times \frac{1}{10}D_{PJ}$ contain little of the total available fuel and therefore their combustion influences are expected to be minor compared with that of larger sized clusters. Furthermore, computational time is also reduced by excluding these sized clusters.

The results shown in the current chapter are based on the cases previously analysed and discussed in Chapter 4; namely seven cases of momentum ratios ranging from $0.00 \leq G_{PJ}/G_{ANN} \leq 4.90$ with $\beta = 0.14 \pm 0.02$. These cases were classified into three flow regimes that were defined based on the influence of G_{PJ}/G_{ANN} on the mean distribution. These regimes are: Annular-dominated regime ($0.00 \leq G_{PJ}/G_{ANN} < 0.18$); transition regime ($0.18 \lesssim G_{PJ}/G_{ANN} \lesssim 1.46$); and PJ-dominated regime ($G_{PJ}/G_{ANN} \gtrsim 1.46$). These same regimes are applied to the results in the current chapter. The ensemble size for each case is 202 images. The instantaneous results are used to provide specific analysis on how jet precession influences the size, location and number of clusters (both large- and small-clusters) in the first 10 diameters of the jet flow. These results are obtained from average number ($\overline{N_c}$) and average area ($\overline{A_c}$) of particle clusters per image, as well as PDFs of particle cluster numbers, equivalent cluster diameters (d_{eq}), cluster perimeters (P_c), and both axial and radial locations of cluster centroids. Spline curves are fitted to PDFs to show any obvious trends.

7.2 Results and discussion

7.2.1 Small-Clusters

The PDFs of the axial location of the centroid of small-cluster ($\frac{1}{10}D_{PJ} \times \frac{1}{10}D_{PJ} \lesssim A_c \lesssim D_{PJ} \times D_{PJ}$) for varying G_{PJ}/G_{ANN} are shown in Figure 7.1. As discussed in Chapter 6, the axial location of the small-cluster centroids can be divided into three image regions; the near-region ($0 < x/D_{PJ} < 3$), the mid-region ($3 \leq x/D_{PJ} \leq 8$) and the downstream edge-region ($8 < x/D_{PJ} < 10$). There are peaks in the PDFs for the near-region and downstream edge-region, while the mid-region has a fairly flat profile. Although these regions are still clearly present for variations in G_{PJ}/G_{ANN}, it can be seen that jet precession has an influence on the axial locations of small-cluster centroids. In the near-region, the peak probability increases with increasing G_{PJ}/G_{ANN} for $G_{PJ}/G_{ANN} \leq 0.58$ and then decreases for $G_{PJ}/G_{ANN} \geq 1.46$. The increased probability at this location is discussed in conjunction with the radial locations of small-cluster centroids.

In the mid-region and for $G_{PJ}/G_{ANN} \leq 0.58$ (annular-dominated and transition regimes) the PDFs are similar and show a approximate linear decrease. For $G_{PJ}/G_{ANN} \geq 1.46$ (PJ dominated regime), the profiles also show similarities to each other, but there is an approximate linear increase. The gradients of these linear increases are greater for higher values of G_{PJ}/G_{ANN}. This indicates that, in this mid-region, is it expected that the location of small-cluster centroids are more likely to occur further from the nozzle for increasing G_{PJ}/G_{ANN}.

In the downstream edge-region all cases have a local maxima in probability. For both annular-dominated and transition regime cases the peak values are similar. The maximum value increases with G_{PJ}/G_{ANN} for PJ-dominated regime cases. In Chapter 6 it was shown that the statistics from clusters near the bottom of the image are subject

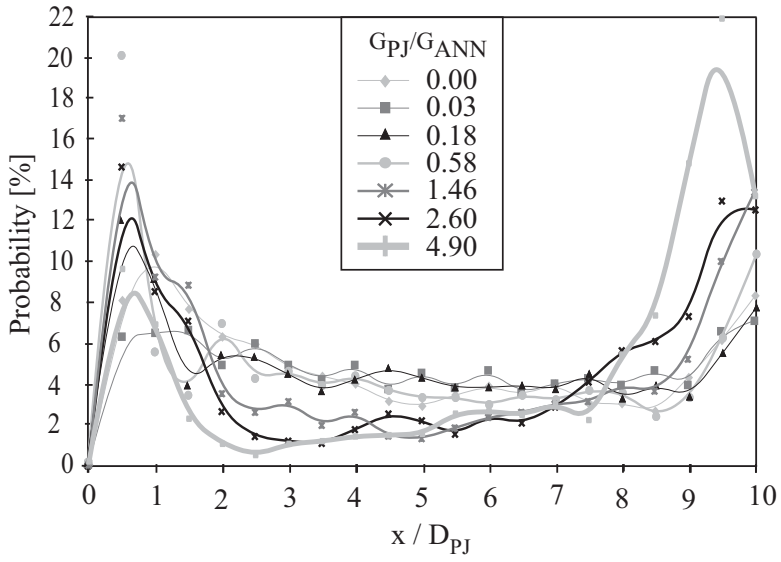

Figure 7.1: PDFs of the axial locations of small-cluster ($\frac{1}{10}D_{PJ} \times \frac{1}{10}D_{PJ} \lesssim A_c \lesssim D_{PJ} \times D_{PJ}$) centroids for varying G_{PJ}/G_{ANN}.

to greater errors because clusters may be clipped. As a result, the probabilities of small-cluster centroids being located in the downstream edge-region shown in Figure 7.1 are greater than what actually occurs. That is, the peak near to the downstream edge of the image results partially from the bounds of the statistical data set. It is expected that the trends evident in the mid-region generally continue for at least some distance further downstream. Nonetheless, the peaks in the downstream edge-region are not necessarily false. As shown in Figure 4.11 and discussed in Chapter 4, there is an elbow at $x/D_{PJ} = 8$ in the relative fluctuations along the centreline, for varying G_{PJ}/G_{ANN}. It is possible that there is a correlation between the two phenomena, but the signal-to-noise in this region for the current data set is too low to enable a strong argument as to the cause. As the downstream edge-region is influenced by clipping, the following analysis of cluster statistics assesses the three regions separately.

The PDFs of the radial location of the small-cluster centroids for three regions in the flow are shown in Figure 7.2. In the near-region, all the clusters have centroids close to the jet centreline. For annular-dominated and transition regime cases ($G_{PJ}/G_{ANN} \leq$

0.58), the PDFs exhibit a bimodal distribution, whereas for PJ-dominated regime cases, the profile approximates a Gaussian distribution. The narrow distributions of the radial locations of cluster centroids in this region are expected as the mean distribution of particles are similarly narrow (see Figures 4.10 and 4.16). The bimodal distribution is not surprising, again based on the mean results shown in Figure 4.2. However, it is interesting to see that the bimodal distribution is not present for the PJ-dominated regime cases. This is a result of the PJ entraining particles across the face of the jet.

The trends in the mid-region are similar to those discussed above. The annular-dominated and transition regime cases still show a bimodal distribution while the PJ-dominated regime cases do not. In all cases, the radial spread is wider than for the near-region. This is also expected due to the correspondingly wider mean spread of particles (see Figures 4.12, 4.13 and 4.16). In the PJ-dominated regime, as G_{PJ}/G_{ANN} increases, the profile of the PDF becomes flatter and wider, much like the mean particle spread. However, for $G_{PJ}/G_{ANN} = 4.90$, the profile is slightly different as it is tri-modal with a major peak near to the jet centreline and two smaller peaks near to the jet edge.

In the downstream edge-region, the bimodal distribution of cluster centroids is still present for annular-dominated and transition regime cases, although the width of the profiles is greater, which is again an expected result based on the mean results (see Figure 4.16). The cases in the PJ-dominated regime have profiles that are again similar to each other, showing no definite peaks in probability. Based on the mean distribution of particles in PJ-dominated regime cases in this region of the flow, it is expected that the distribution of small-clusters are also fairly uniform.

As shown for the PDFs of axial location of small-cluster centroids, the radial location of cluster centroids can be defined by the flow regimes. The annular-dominated and transition regime case show distinct bimodal distributions with peaks on either side of the jet centreline. These peaks correspond to the particle-laden annular nozzle. These

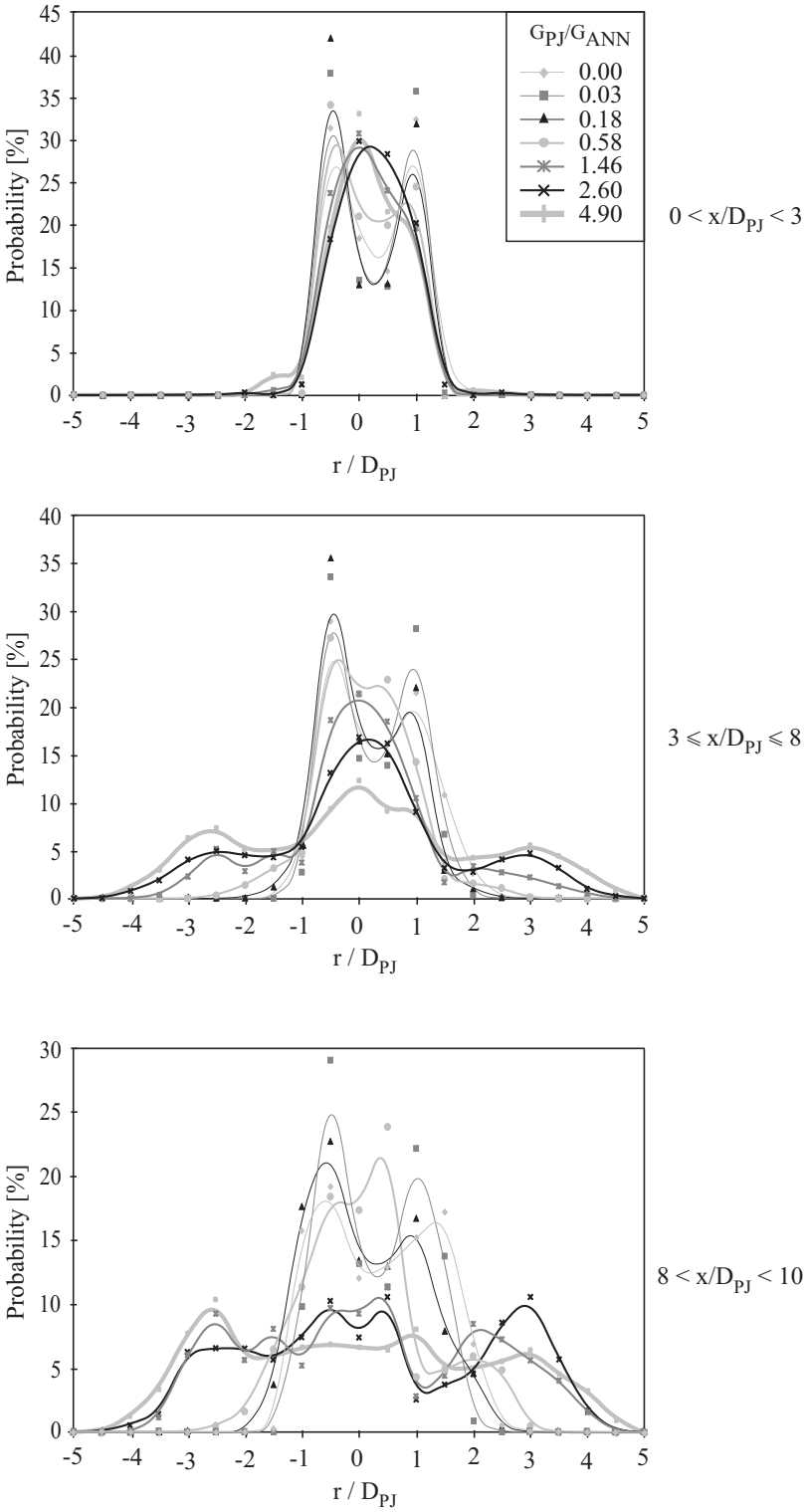

Figure 7.2: PDFs of the radial locations of small-cluster centroids located in the near-, mid- and downstream edge-regions for varying G_{PJ}/G_{ANN}.

bimodal profiles persist for all $0 < x/D_{PJ} < 10$, indicating that jet precession has little influence in the location of small-clusters when $G_{PJ}/G_{ANN} \leq 0.58$. For PJ-dominated regime cases, the PDF profiles initially approach Gaussian, but moving downstream, these profiles become wider and flatter. In both the near- and downstream edge-regions, the radial profiles for PJ-dominated regimes are very similar. However, in the mid-region, the profiles differ in magnitude, possibly indicating that G_{PJ}/G_{ANN} has a stronger influence on the radial distribution of small-clusters in this region than in either the upstream or downstream locations.

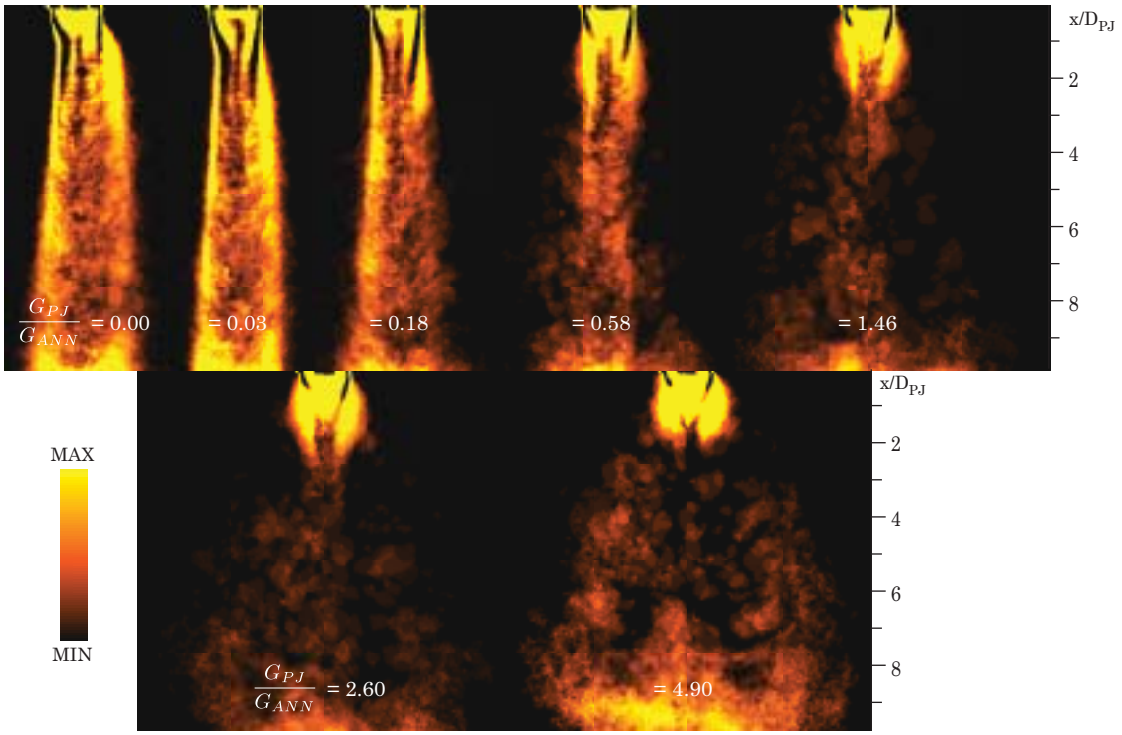

Figure 7.3: A planar PDF of the small-clusters for varying G_{PJ}/G_{ANN}.

Figure 7.3 is a series of images for varying G_{PJ}/G_{ANN}. These images are the summation of the cluster maps, but the maps have been converted to binary form and only the small-clusters are included. In essence, these images are PDFs of small-clusters (rather than small-cluster centroids) for the entire flow field recorded. The scale for each image is optimised separately. A much larger ensemble is required for these images to provide definite measurements, but the trends are still clear. For example, the bimodal distribution in the PDF of the radial small-cluster centroids in the near-region is a result

of the very low signal along the nozzle centreline. While the bimodal distribution in the mid-region for annular-dominated regime cases (Figure 7.2) corresponds to the greater likelihood that clusters be found near to the edge of the jet than other radial locations. The preference of small-clusters towards the jet edge is not clearly evident in the transition regime or PJ-dominated regime, but a void in the centre of the jet for $G_{PJ}/G_{ANN} = 4.90$ provides some indication that it may still exist. However, the ensemble size is far too small to be definitive.

A plot of the average number of small-clusters ($\overline{N_{c,s}}$) identified per image for the three axial regions and varying G_{PJ}/G_{ANN} is shown in Figure 7.4 (note the two scales). The value of $\overline{N_{c,s}}$ decreases with increasing G_{PJ}/G_{ANN} in the near-region and then becomes fairly constant. In this region the average area of small-clusters ($\overline{A_{c,s}}$) varies only slightly for annular-dominated and transition regimes cases ($G_{PJ}/G_{ANN} \lesssim 1.46$), but in the PJ-dominated regime, $\overline{A_{c,s}}$ increases significantly.

As shown in Chapter 6, due to merging and dividing of clusters in the cluster determination method, the statistics of individual clusters are more sensitive to the selection of L compared with A_{total} per image. The influence of G_{PJ}/G_{ANN} may have similar effects. Therefore, $A_{total,s}$ per image is also assessed and shown in Figure 7.4 as well. In the near-region $A_{total,s}$ shows a minimum for cases in the transition regime and peaks in both annular- and PJ-dominated regimes. This does not indicate a inverse proportional relationship between $\overline{N_{c,s}}$ and $\overline{A_{c,s}}$, hence there is no indication that the changes in $\overline{N_{c,s}}$ or $\overline{A_{c,s}}$ result from the simple merging or dividing of clusters. Instead, the change in $A_{total,s}$ indicates that jet precession can result in either a reduction or increase in the amount of small-clusters in this region, depending on the value of G_{PJ}.

In the mid-region, $\overline{N_{c,s}}$ decreases with increasing G_{PJ}/G_{ANN} in both annular-dominated and transition regimes, but increases slightly for the PJ-dominated regime. However, $\overline{A_{c,s}}$ has a very slight, almost negligible decrease. Correspondingly, $A_{total,s}$ has a similar trend to $\overline{N_{c,s}}$; a initial decrease in the annular-dominated and transition regimes and

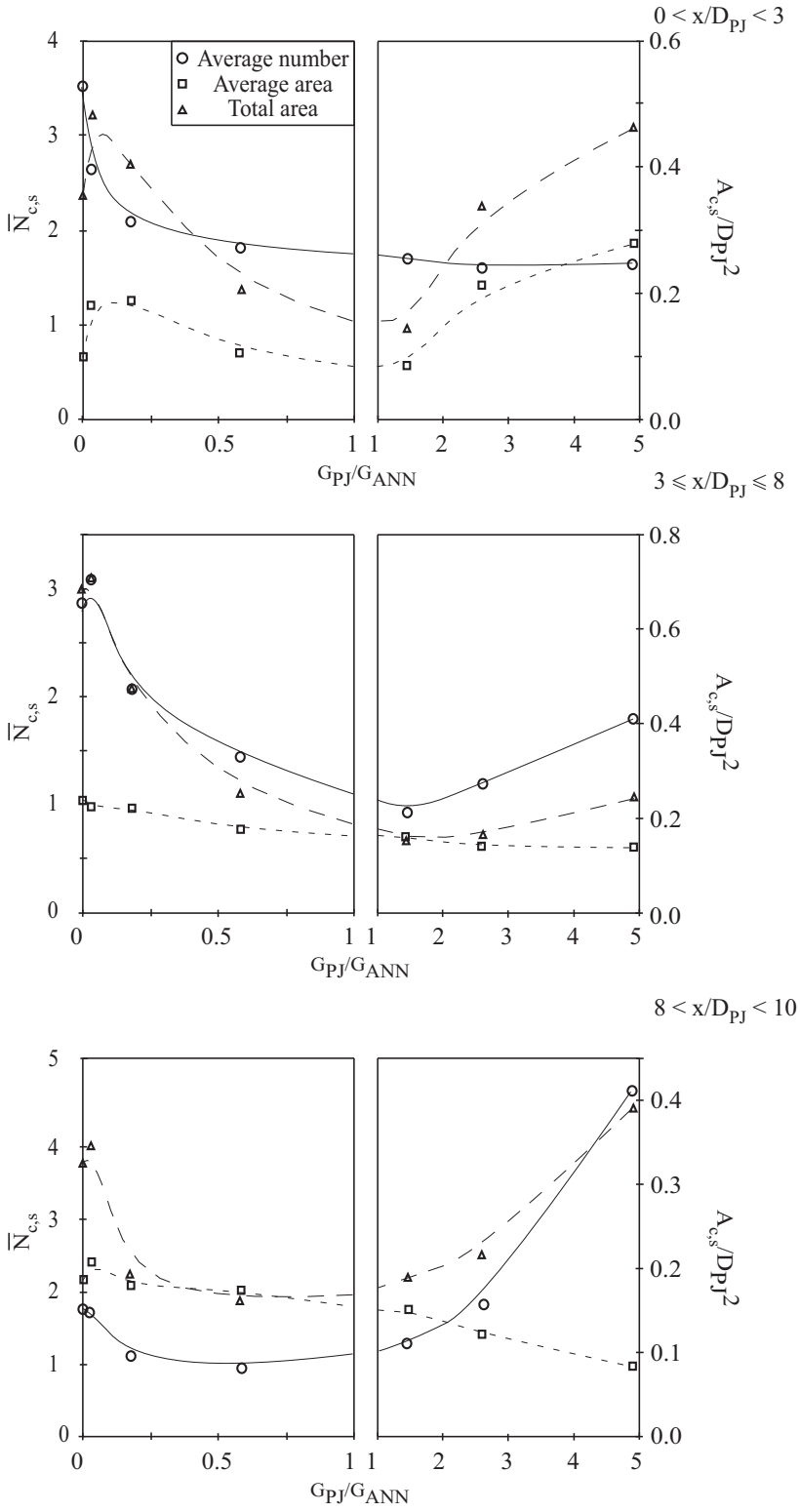

Figure 7.4: Plots of $\overline{N_{c,s}}$, $\overline{A_{c,s}}$ and $A_{total,s}$ of small-clusters located in the near-, mid- and downstream edge-regions for varying G_{PJ}/G_{ANN}.

a slight increase in the PJ-dominated regime.

The measurements from the downstream edge-region are consistent with those in the mid-region, but biased by clipping. The effect of clipping is to artificially increase the number of smaller clusters. Nonetheless, in the PJ-dominated regime, $\overline{N_{c,s}}$ almost quadruples compared with annular-dominated and transition regime cases. There is a slight decrease in $\overline{A_{c,s}}$ with this increase in $\overline{N_{c,s}}$. This result, although emphasised by clipping, is still a genuine trend that increasing G_{PJ}/G_{ANN} in the PJ-dominated regime results in an increase in $\overline{N_{c,s}}$.

Over the three regions, a general overview of the influence of jet precession on the average small-cluster characteristics is that there is a decrease in both number and area with increasing G_{PJ}/G_{ANN} in the annular-dominated and transition regimes. For the PJ-dominated regime there is an increase in $\overline{N_{c,s}}$ and a slight decrease in $\overline{A_{c,s}}$ in the mid- and downstream edge-regions, while there is a slight increase in $\overline{A_{c,s}}$ for near-region.

The PDFs of number of small-clusters per instantaneous image for the three regions in the flow are presented in Figure 7.5. In the near-region, the PJ-dominated and transition regime cases are very similar, with a peak at approximately two clusters per region. This value corresponds with $\overline{N_{c,s}}$ in this region shown in Figure 7.4. The two annular-dominated cases show a flatter profile.

In the mid- and downstream edge-regions, there are some slight changes compared with the near-region. It can be seen that the transition regime cases maintain a similar profile in all regions investigated; a dominant peak for approximately two small-clusters. The annular-dominated regime cases develop stronger peaks with increased distance downstream. However, the PJ-dominated regime cases become wider and flatter further downstream. In terms of influencing the number of small-clusters in a jet flow, these results indicate that there is a high probability of a greater number of small-clusters

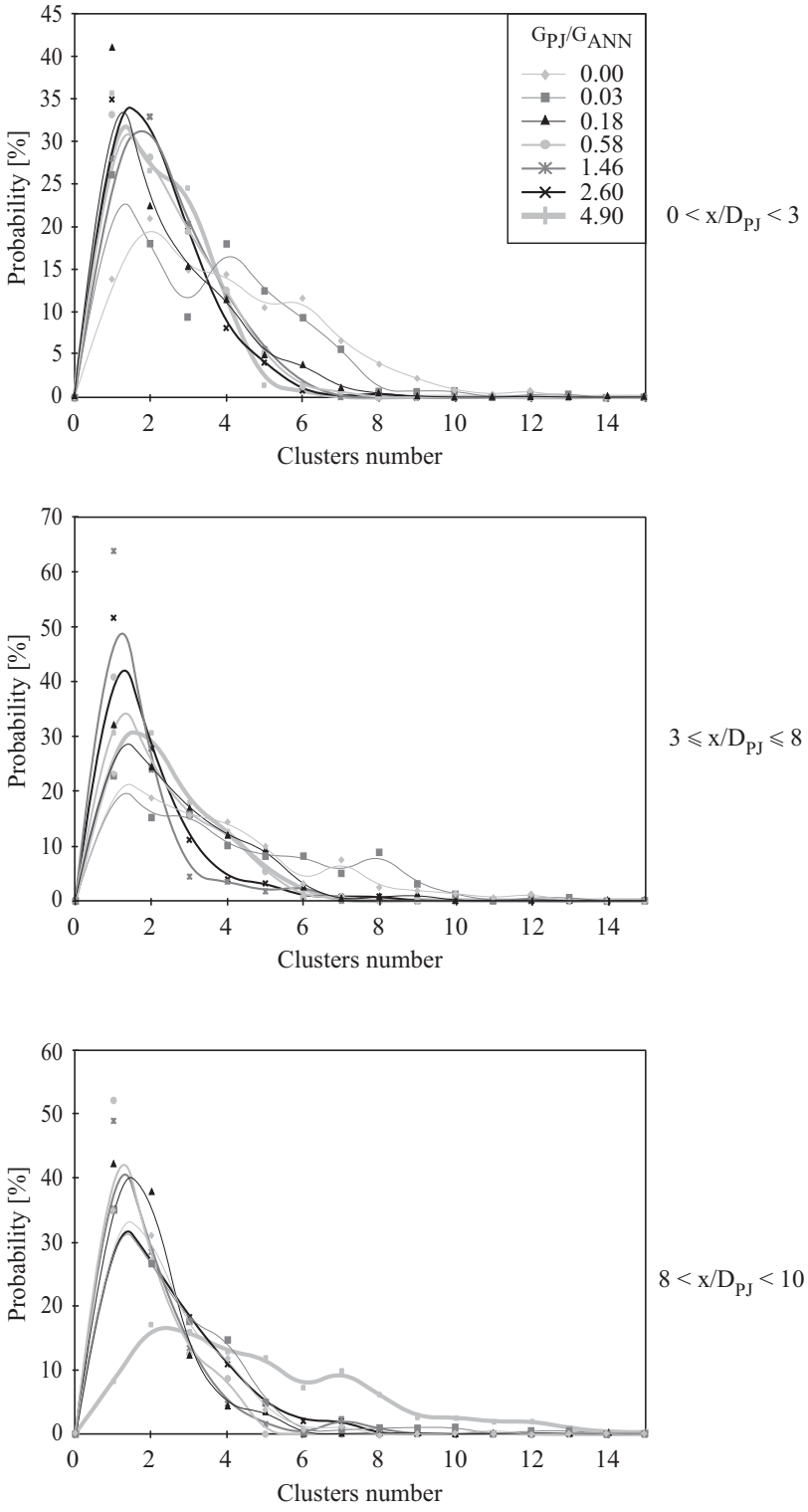

Figure 7.5: PDFs of the number of small-clusters located in the near-, mid- and downstream edge-regions for varying G_{PJ}/G_{ANN}.

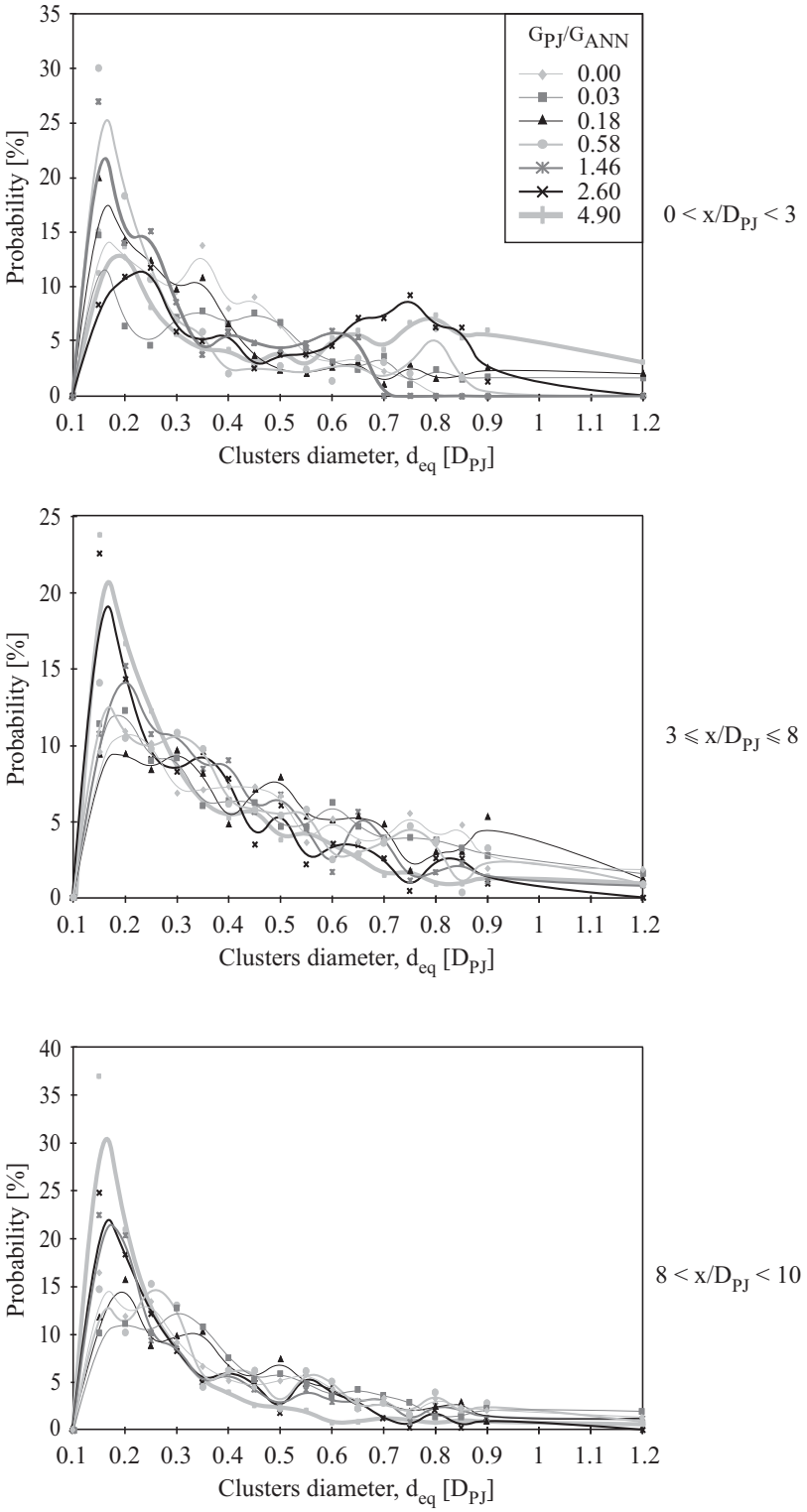

Figure 7.6: PDFs of d_{eq} for small-clusters located in the near-, mid- and downstream edge-regions for varying G_{PJ}/G_{ANN}.

with increasing jet precession.

Figure 7.6 shows the PDFs of d_{eq} for small-clusters for the three regions in the flow and varying G_{PJ}/G_{ANN}. As explained in Chapter 6, d_{eq} is the diameter of a circle with the same area, A_c, as the cluster in question. The major finding from these three images in Figure 7.6 is that the peak in probability for the PJ-dominated regime cases increase for $x/D_{PJ} \leq 3$. This corresponds with the decrease in $\overline{A_c}$ as shown in Figure 7.4. Combining these finding with the corresponding increase in $\overline{N_{c,s}}$ (Figure 7.4) at these downstream locations, it can be concluded that PJ-dominated regime flows will have more small small-clusters than other cases with $G_{PJ}/G_{ANN} > 0.00$ and there will be more of these clusters for higher values of G_{PJ}/G_{ANN}.

Figure 7.7 shows the PDFs of P_c for small-clusters in the three regions of the flow. The results show little variation with changes to G_{PJ}/G_{ANN} for all $0 < x/D_{PJ} < 10$. From the PDFs of both d_{eq} and P_c it is evident that in the mid- and downstream edge-regions, the influence of jet precession is not preferential to any specific size range of small-clusters. Increasing G_{PJ}/G_{ANN} may increase or decrease average areas, but the relative distributions of d_{eq} and P_c for all small-clusters are almost constant.

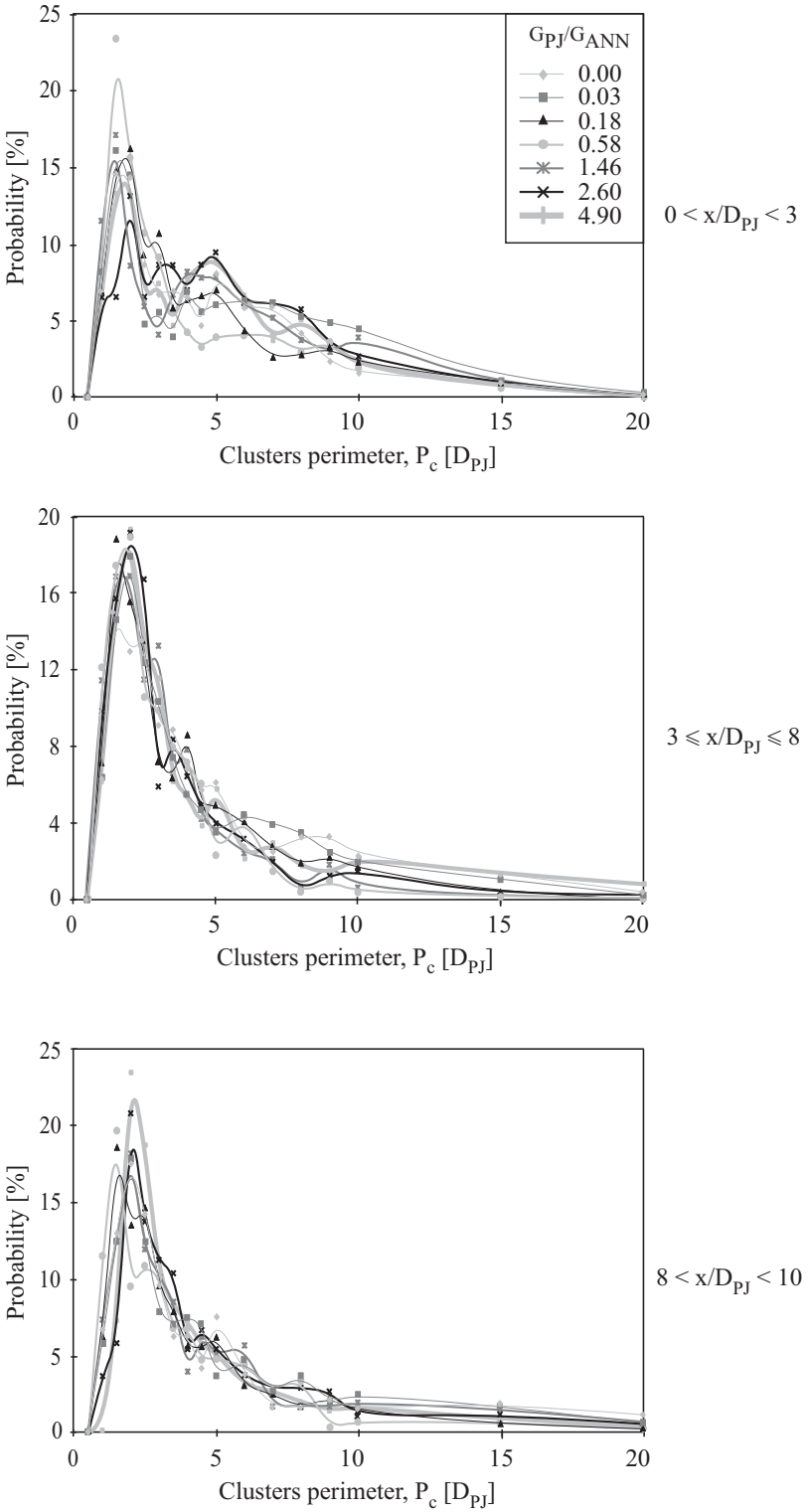

Figure 7.7: PDFs of P_c for small-clusters located in the near-, mid- and downstream edge-regions for varying G_{PJ}/G_{ANN}

7.2.2 Large-Clusters

The influence of G_{PJ}/G_{ANN} on the characteristics of large-clusters is different to that of small-clusters and is shown below. Large-clusters are defined here as clusters with $A_c \geq D_{PJ} \times D_{PJ}$ ($A_c \geq$ 10,000 pixels). It should be noted that there are significantly fewer large-clusters in the flow than small-clusters. As a result, the statistics presented are subject to greater variance than seen with the small-clusters above. The three regions of the flow used in the discussion for small-clusters are also applied here to discuss the influence of jet precession on large-clusters. These regions are the near-region ($0 < x/D_{PJ} < 3$), the mid-region ($3 \leq x/D_{PJ} \leq 8$) and the downstream edge-region ($8 < x/D_{PJ} < 10$).

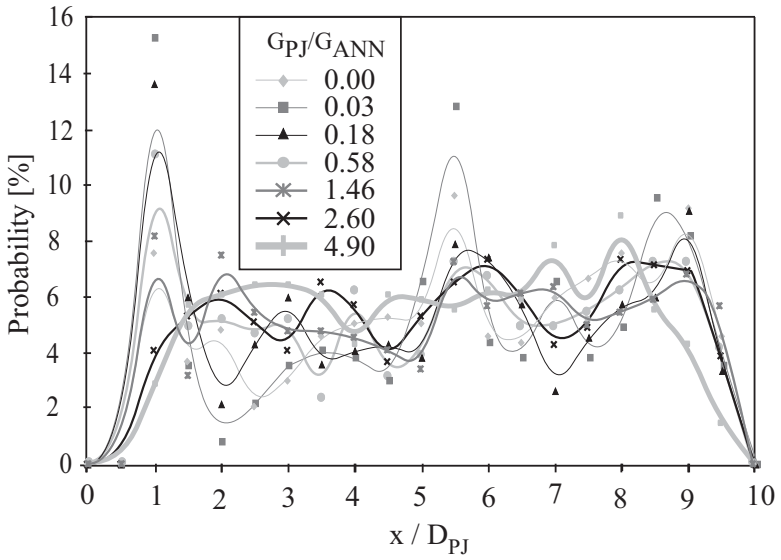

Figure 7.8: PDFs of the axial locations of large-cluster centroids for varying G_{PJ}/G_{ANN}.

Figure 7.8 shows the PDFs of axial locations of the large-cluster. There is significant scatter in the data, which is caused by the low numbers of large-clusters identified in the flows. Nevertheless, some trends are evident. There are no large-clusters for $x/D_{PJ} < 1$. This is consistent with the definition of the size of a large-cluster and with the observation of particle devoid region immediately downstream from the nozzle exit

plane in the mean particle distribution profile (see Figure 4.1). The probability is also very low for large-clusters in the downstream edge-region. This is due to clipping causing an artificially low probability of large-clusters.

The general trend shown in Figure 7.8 is that there is a steady increase in the probability of large clusters with increased axial distance in the mid-region, and this is for all cases. There are two peaks for $G_{PJ}/G_{ANN} \leq 1.46$ at $x/D_{PJ} \approx 1$ and 5.5. These peaks are highest for the jets with the narrowest mean spread (i.e. $G_{PJ}/G_{ANN} = 0.03$ and 0.18). On inspection of the results shown in Chapter 4, there are no corresponding anomalies at these location that exist for varying G_{PJ}/G_{ANN}. The results for small-clusters also do not present any similar anomalies, nor do the following results on large-cluster. It is therefore unknown if these peaks in probability for large-clusters are real, or artifacts of either the measurements or methodology used to identify clusters.

The PDFs of the radial location of the large-cluster centroids for the three axial regions are shown in Figure 7.9. In the near-region all cases show a bias towards the side of the nozzle with the initial particle bias. This bias is much greater than expected based on the mean particle distribution and not present for the small-clusters. In Chapter 4 is was shown that there is a $30 \pm 3\%$ bias for $G_{PJ}/G_{ANN} \leq 2.60$ in the mean particle distribution at $x/D_{PJ} = 0.1$, but this bias is almost negligible at the centreline concentration peak locations ($x/D_{PJ} = x_p$) and measured locations further downstream (Figures 4.12 and 4.13). The bias in the location of large-cluster centroids is much more evident than the bias in mean particle distributions. This indicates that the initial bias may have a stronger influence of the large-scale instantaneous flow structures, than on the mean distribution. As combustion relates to the instantaneous distribution of particles, this finding may have significant implications for PF fired systems, in relation to the uniformity of PF at the nozzle exit.

For the PJ-dominated regime, the PDF profiles of the radial locations of large-clusters in the near-region are bimodal. A similar bimodal behaviour is present in the cor-

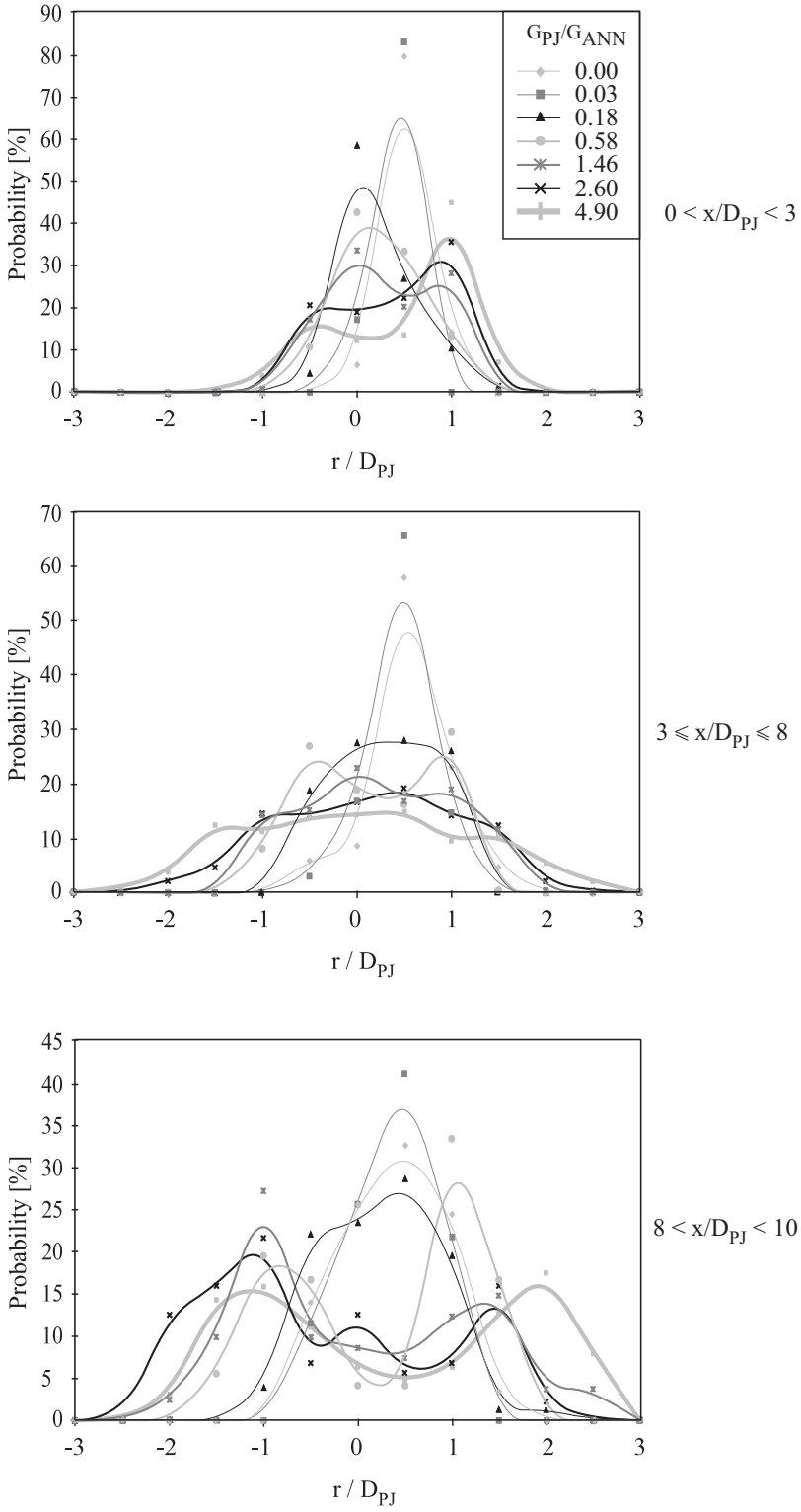

Figure 7.9: PDFs of the radial locations of large-cluster centroids located in the near-, mid- and downstream edge-regions for varying G_{PJ}/G_{ANN}.

responding PDFs for small-clusters (Figure 7.2). There, the bimodal behaviour is deduced to result from the initial annular distribution of particles, but the bimodal distribution of small-cluster centroids decreases with increase G_{PJ}/G_{ANN}. As the bimodal profile for large-clusters is not present for annular-dominated and transition regime cases, and it has already be shown that jet precession reduces the initial mean particle bias (Chapter 4), it is unlikely that this bimodal behaviour is a result of the initial biased particle distribution in the annular nozzle. Rather, this trend corresponds with the entrainment of particle across the face of the nozzle. In a planar view, the jet appears to bifurcate, which provides a plausible explanation for the bimodal distribution of large-cluster centroids.

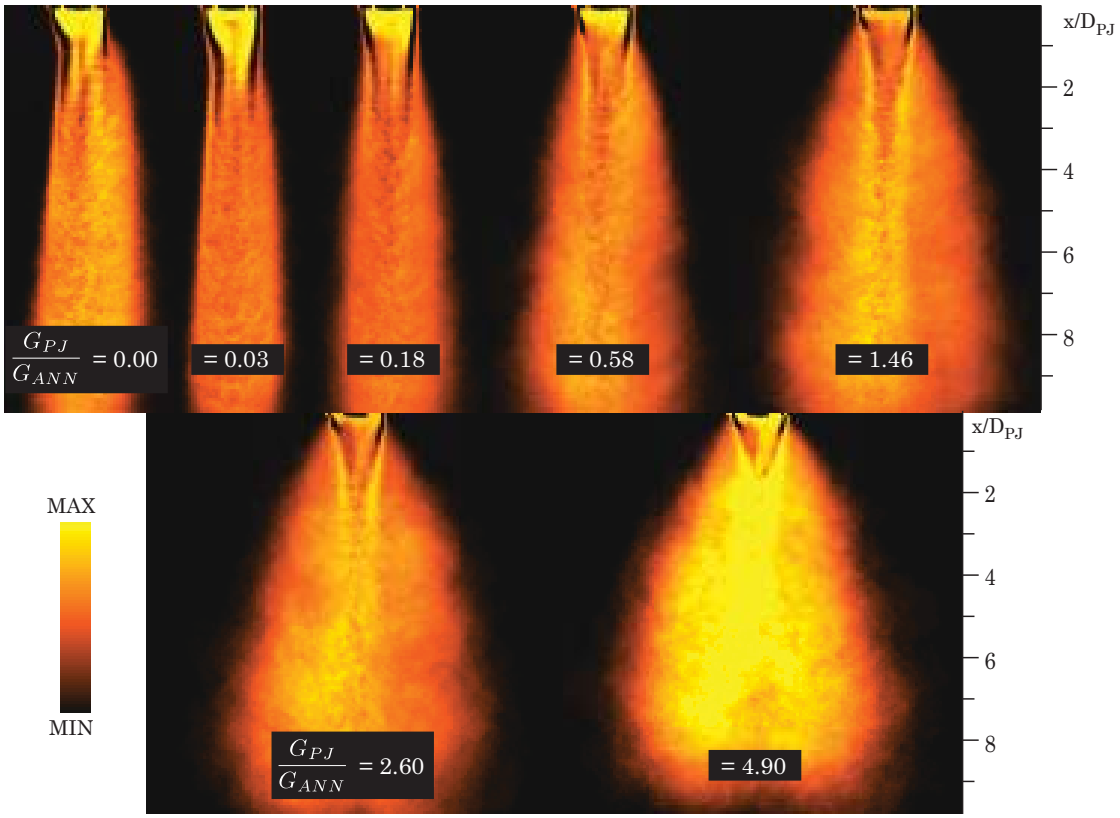

Figure 7.10: A planar PDF of the large-clusters for varying G_{PJ}/G_{ANN}.

The planar images of the large-clusters from the ensemble are shown in Figure 7.10. These images are scaled individually. Like the corresponding images for small-clusters, these images are subject to low ensemble size, but because the large-clusters have a larger planar area compared with small-clusters, the images have a smoother distribu-

tion. Unlike the small-clusters, large-clusters do not show the same preference to form near to the jet edge. Rather, there is a preference for large-clusters to form on either side of the jet centreline.

A plot of the average number of large-clusters ($\overline{N_{c,l}}$) identified per image for the three regions and varying G_{PJ}/G_{ANN} is shown in Figure 7.11. Compared with $\overline{N_{c,s}}$ shown in Figure 7.4, there are significantly less large-clusters for all regions in the flow analysed. (This was previously used to explain the greater scatter in data for large-clusters).

In the near-region, there is a general increase in $\overline{A_{c,l}}$ and $\overline{N_{c,l}}$ for all regions with increasing G_{PJ}/G_{ANN}. This trend is also present in the mid-region, but there is a decrease in $\overline{A_{c,l}}$ in the PJ-dominated regime. It is interesting to see that increasing $\overline{N_{c,l}}$ and decreasing $\overline{A_{c,l}}$ for PJ-dominated regime cases results in an almost constant $A_{total,l}$ per image.

In the downstream edge-region, $\overline{N_{c,l}}$ varies only slightly, but again there is a decrease in the PJ-dominated regime. The value of $\overline{A_{c,l}}$ is a maximum in the transition regime before decreasing in the PJ-dominated regime. Based on the decreasing $\overline{A_{c,l}}$ in the PJ-dominated regime case in both the mid- and downstream edge-regions, it may be possible that $G_{PJ}/G_{ANN} \geq 4.90$ results in the break up of large-clusters, although the issue of clipping artificially increasing the number of clusters needs to be considered.

The PDFs of the number of large-clusters per image are not shown. The maximum recorded number of large-clusters per image was only five. The corresponding PDFs do not show results of significant meaning, other than the PDF profiles are all very similar.

The PDFs of d_{eq} for large-clusters for the three regions in the flow are presented in Figure 7.12. In the near-region the profiles indicate that transition regime cases have the highest probability of smaller sized large-clusters. In the mid-region, the profiles for

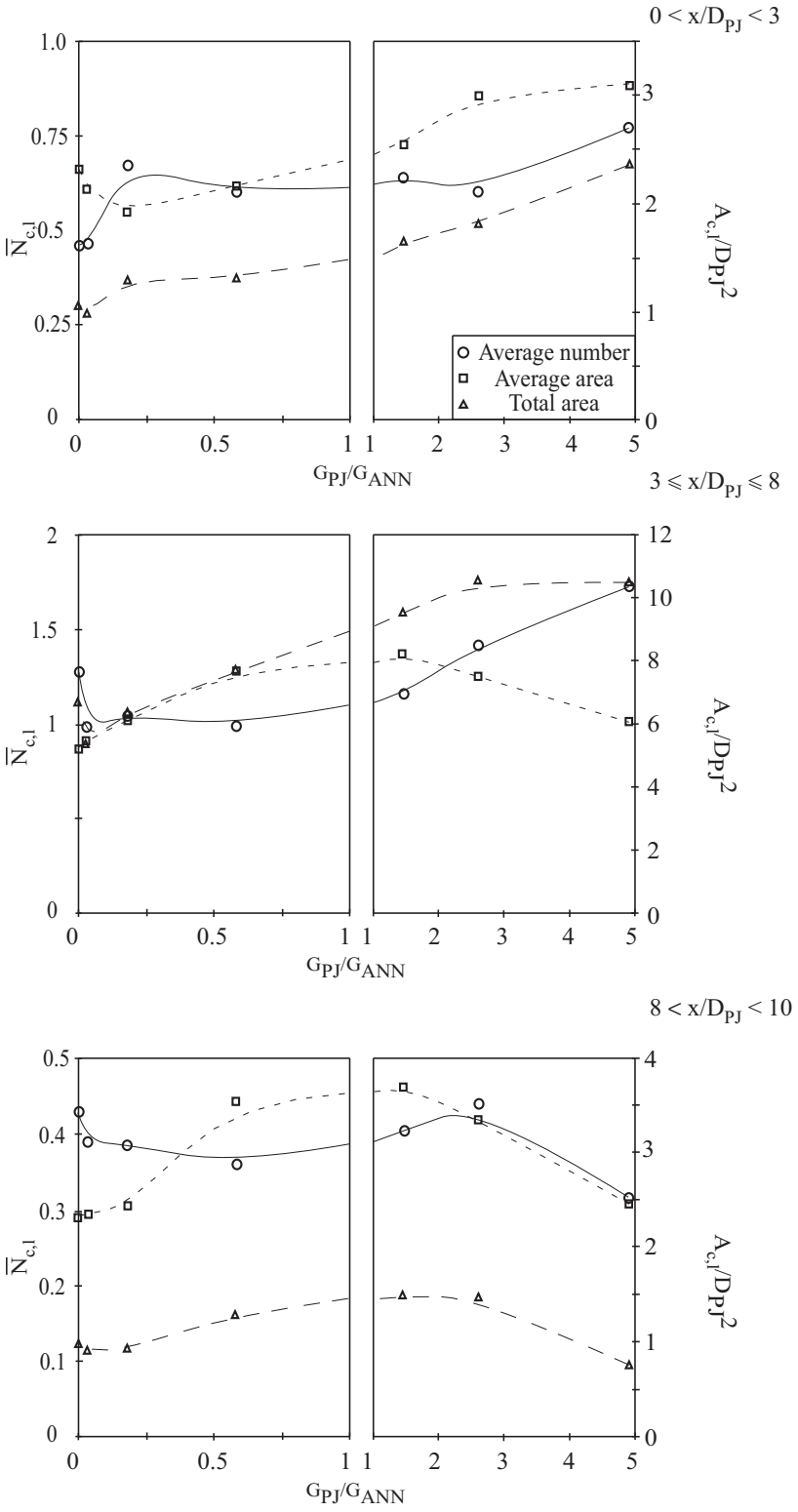

Figure 7.11: Plots of $\overline{N_{c,l}}$, $\overline{A_{c,l}}$ and $A_{total,l}$ of large-clusters in the near-, mid- and downstream edge-regions for varying G_{PJ}/G_{ANN}.

varying G_{PJ}/G_{ANN} are similar to each other, although annular-dominated regime cases show higher probability of smaller sized large-clusters. In the downstream edge-region, the profiles are similar. It is unusual that the profiles in the near- and downstream edge-regions are similar, while those in the mid-region are not. In the mid-region, there is a much higher probability that $d_{eq} \geq 3$. However, these findings support those of $\overline{A_{c,l}}$ (Figure 7.11). These results indicate either the axial distance from the nozzle in the range $0 < x/D_{PJ} < 10$, may have more influence on large-cluster characteristics than G_{PJ}/G_{ANN}, or that the clipping of clusters in the downstream edge-region distorts cluster statistics such that the results are incorrect.

Figure 7.13 shows the PDFs of P_c for large-cluster in the three regions of the flow. In the near-region the profiles are very similar, although the peak in probability is lower for PJ-dominated regime cases. In this region there is a slightly higher probability that the large-clusters generated in PJ-dominated flows will have a higher value of P_c. The profiles are also very similar in the mid-region. The PJ-dominated regime cases have lower peaks and wider profiles, again indicating a slightly higher probability of higher values of P_c for the large-clusters generated by these flows. From a comparison of the scales in these two regions it is evident that the near-region has much smaller values of P_c.

The PDF profiles for the downstream edge-region can be classified into two, based on G_{PJ}/G_{ANN}. For annular-dominated and transition regime cases, the profiles have a distinct peak in probability. In this region, and for these cases, $P_c \leq 100D_{PJ}$. For PJ-dominated regime cases the PDF profiles are much lower and wider. These cases show a very low probability that $P_c \leq 50D_{PJ}$. As G_{PJ}/G_{ANN} increases, so does the likelihood that P_c will also increase.

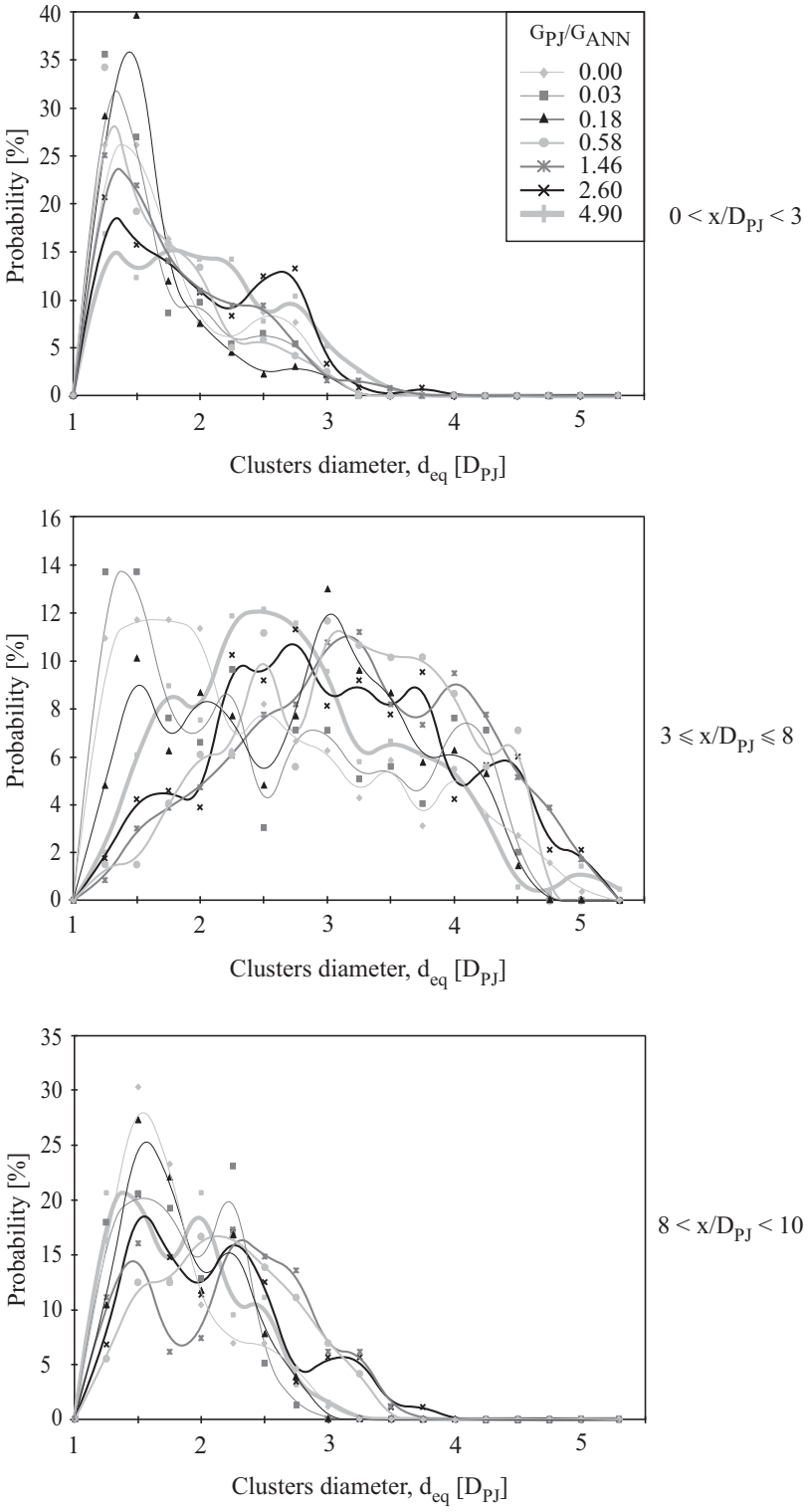

Figure 7.12: PDFs of d_{eq} for large-clusters located region in the near-, mid- and downstream edge-regions for varying G_{PJ}/G_{ANN}.

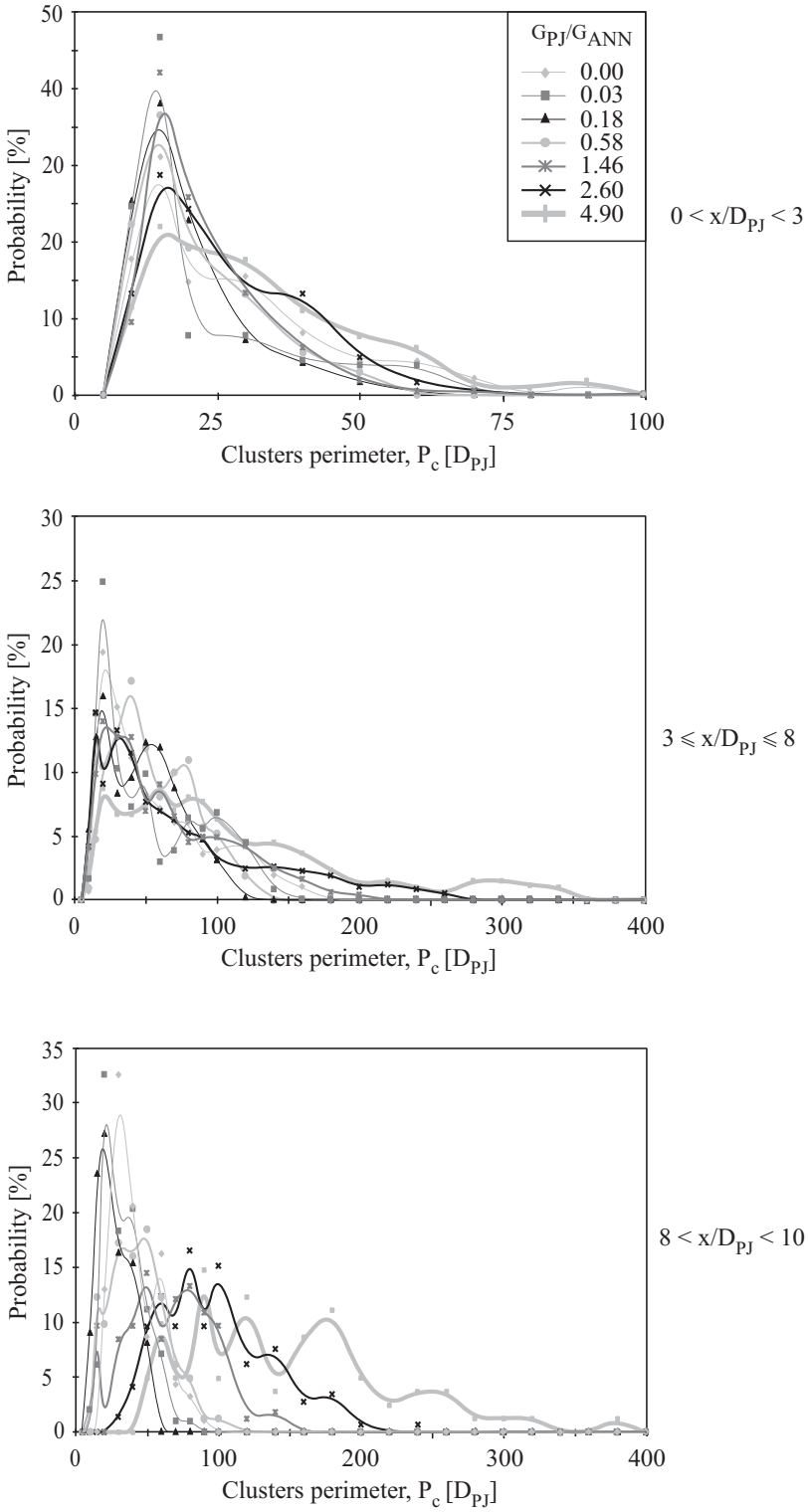

Figure 7.13: PDFs of P_c for large-clusters located in the near-, mid- and downstream edge-regions for varying G_{PJ}/G_{ANN}.

7.3 Conclusions

The influence of jet precession on the characteristics of particle clusters in the first 10 jet diameters of a particle-laden jet has been investigated. Particle clusters have been separated into two groups: small-clusters, with $\frac{1}{10}D_{PJ} \times \frac{1}{10}D_{PJ} \lesssim A_c < D_{PJ} \times D_{PJ}$ (100 pixels $\leq A_c \leq$ 10,000 pixels); and large-clusters, with $A_c \geq D_{PJ} \times D_{PJ}$ ($A_c \geq 10,000$ pixels). The analysis of these statistics was conducted over three axial regions; the near-region ($0 < x/D_{PJ} < 3$), the mid-region ($3 \leq x/D_{PJ} \leq 8$) and the downstream edge-region ($8 < x/D_{PJ} < 10$). The results are based on an ensemble of 202 images for each case. The statistics have been obtained using the cluster determination methodology outlined in Chapter 6 using $L = \frac{1}{2}D_{PJ}$. Measurements are presented for $\overline{N_c}$, $\overline{A_c}$, and A_{total}, as well as PDFs of both radial and axial locations of cluster centroids, the number of clusters occurring, d_{eq} and P_c.

The results for both small- and large-clusters can be classified into annular-dominated ($0.00 \geq G_{PJ}/G_{ANN} < 0.18$), transition ($0.18 \lesssim G_{PJ}/G_{ANN} \lesssim 1.46$) and PJ-dominated regimes ($G_{PJ}/G_{ANN} \gtrsim 1.46$), as is the case for the mean distribution. For the annular-dominated regime cases there is little variation in the results for either small- or large-clusters. From the PDF of axial locations of small-cluster centroids (Figure 7.1) and the plot of $\overline{N_{c,s}}$ (Figure 7.4), it can be seen that number of small-clusters decreases further downstream, but $\overline{A_{c,s}}$ will actually increase. Small-cluster centroids are more likely to be located near to the jet edge, thus producing a bimodal distribution in probability. There is almost an order of magnitude fewer large-clusters than small-clusters. With increasing axial distance from the nozzle for $0 < x/D_{PJ} \leq 8$, the number of large-clusters does not increase significantly, but $\overline{A_{c,l}}$ does. Unlike small-clusters, the radial locations of large-cluster centroids have Gaussian distributions, but centred on the side with the higher initial particle distribution (see Figure 4.2). These large-clusters are strongly influenced by the annular jet.

In the transition regime cases, the PDFs of small-cluster centroids located in both

axial and radial directions are similar to those for the annular-dominated regime, although there are still some minor differences. The value of $\overline{A_{c,s}}$ for all regions in the flow investigated are also similar to the annular-dominated regime cases. Between $G_{PJ}/G_{ANN} = 0.03$ and $G_{PJ}/G_{ANN} = 0.18$, $\overline{A_{c,s}}$ per image decreases in all regions of the flow. However, in the near- and downstream edge-regions, $\overline{A_{c,s}}$ for cases in the transition regime remains constant. In the mid-region, $\overline{A_{c,s}}$ decreases for increasing G_{PJ}/G_{ANN} in the transition regime. The PDFs of cluster number, d_{eq} and P_c do not vary significantly in the transition regime. The influence of jet precession on large-clusters in the transition regime has very little influence, except with the radial location in the downstream edge-region, which becomes wider and flatter. It is interesting that the PDF of the radial locations of large-cluster centroids are sensitive to jet precession in the transition regime, whereas the small-clusters are not. In this regime, large-clusters are thrust outwards, whereas small-clusters remain distributed near to the jet axis, as was the case for annular-dominated regime cases. The value of $\overline{A_{c,l}}$ in the downstream edge-region increases dramatically.

In the PJ-dominated regime, the influence of jet precession on particle clusters is significant. Increasing G_{PJ}/G_{ANN} in this regime from 1.46 to 4.90 results in almost twice as many small-clusters in the mid-region and almost four-times as many in the downstream-edge region. The remarkable increase in the downstream edge-region arises partially from clipping, but based on what happens in the mid-region, still indicates many more small-clusters for increasing G_{PJ}/G_{ANN}. The PDFs indicate that the small-clusters are also smaller for increasing G_{PJ}/G_{ANN}. Therefore, it is clear that jet precession increases the number of small-clusters, but also results in a reduction in the size of these clusters.

Unlike small-clusters generated in annular-dominated and transition regime cases, small-clusters generated in PJ-dominated regime cases do not exhibit any bimodal distribution in the PDFs of the radial location of small-cluster centroids. Rather, they are Gaussian and centred near to the jet centreline. This results from the mixing of

the phases and jets, as well as the entrainment of particles across the face of the nozzle and subsequently small-clusters occur along the jet centreline.

The large-clusters are also strongly influenced by jet precession in the PJ-dominated regime. In the near-region, $\overline{N_{c,l}}$ and $\overline{A_{c,l}}$ increase with increasing G_{PJ}/G_{ANN}. However, in both mid- and downstream edge-regions $\overline{A_{c,l}}$ decreases. The radial distribution of large-cluster centroids becomes wider with increasing G_{PJ}/G_{ANN} in the PJ-dominated regime, which is analogous to the mean particle distribution (see Chapter 4). There are little variations in the PDFs of d_{eq} for varying G_{PJ}/G_{ANN}, but the PDFs of P_c in the downstream edge-region for PJ-dominated regimes cases have marked differences to the other cases. The profile becomes flatter and wider and shows that there is a very high probability that P_c for large-clusters in this regime will be much greater than that for large-clusters generated in other cases.

These results show that jet precession has a strong influence on both small- and large-clusters, as presented with the current flow configurations. Characteristics of particle clusters can be manipulated using jet precession. However, the trends are not consistent throughout the flow investigated. The influence of jet precession on large- and small-clusters in the near-, mid- and downstream edge-regions are different. Nonetheless, there are some overarching findings. Jet precession can increase the number, but reduce the area, while increasing the radial spread of both small- and large-clusters centroids. Manipulation of these characteristics can result in the augmentation of the combustion environment resulting in possible reductions in NO_X emissions and ignition temperatures.

Chapter 8

Influences of particle mass loading on particle clusters

8.1 Introduction

In Chapter 5, the influence of particle mass loading (β) on the mean and fluctuating components of the distribution of particles was presented. Relative to the influence of G_{PJ}/G_{ANN} as shown in Chapter 4, the influence of β is minor. Nonetheless, there is an elongation of the jet with increased β, which was also found by Hedman and Smoot [1975], Wall et al. [1982] and Fan et al. [1992]. However, findings from Chapter 5 indicate that the variation in the flow attributed to influence of β may stem from the increase in G_{ANN} rather than an interplay between the two phases.

The aim of the current chapter is to assess the influence of β on the distribution of particle clusters. The experimental cases shown in Chapter 5 are used; specifically, $G_{PJ}/G_{ANN(f)} = 6.19$ with seven cases in the range of $0.041 \leq \beta \leq 0.461$. The identification and characterisation of clusters is as per the previous chapter. The

ensemble size for each case is 202 images. The results presented include ensembles of modified cluster maps and plots of the average number ($\overline{N_c}$), average area ($\overline{A_c}$), and total area (A_{total}) for small- and large- clusters separately. To isolate the influence of β from that of G_{PJ}/G_{ANN}, comparisons of some cluster statistics for cases with $\beta = 0.14 \pm 0.02$ are also provided. The PDFs of cluster characteristics are provided in Appendix A.

8.2 Results and discussion

8.2.1 Small-Clusters

Figure 8.1 shows a series of images for varying β. These images are the summation of the cluster maps, but the maps have been converted to binary form and only the small-clusters are included. In essence, these images are PDFs of small-clusters (rather than small-cluster centroids) for the entire flow field recorded. The scale for each image is optimised separately. With the exception of $\beta = 0.041$, the six cases show strong similarities. There is a tendency that small-clusters are located towards the edge of the jet and along the jet centreline. The jet centreline is biased towards the left hand side of the image, resulting from the particle bias in the nozzle. There are high numbers of clusters in the near-region, as well as at the bottom of the image. The important feature from this figure is that variations in $\beta > 0.041$ have little influence on location of small-clusters.

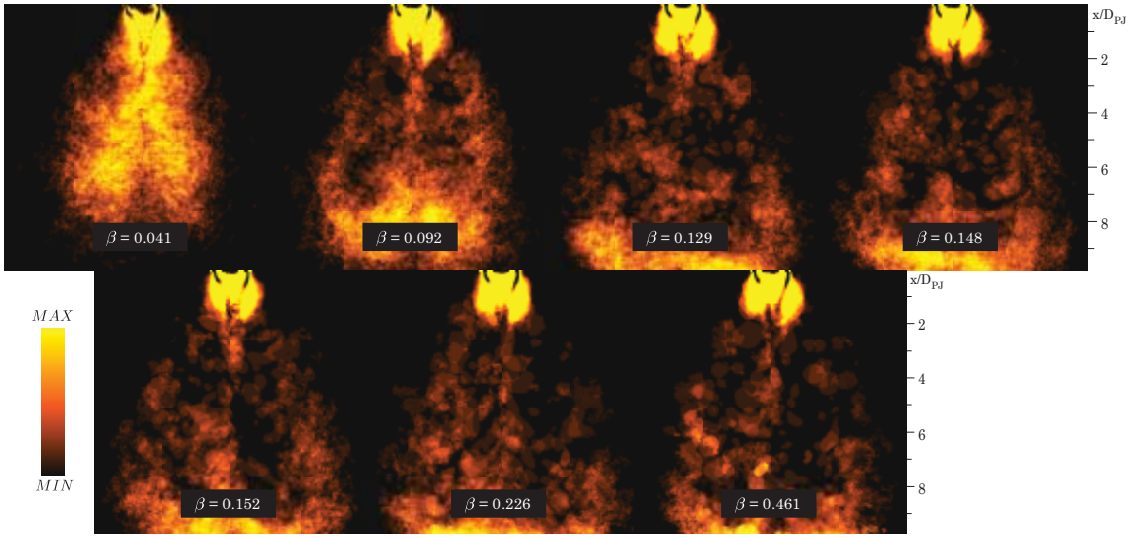

Figure 8.1: A planar PDF of the small-clusters for varying β.

The PDF of the small-cluster centroids in the axial direction are shown in Figure 8.2. It is clear from this figure that the three regions (near-region, $0 < x/D_{PJ} < 3$; mid-region, $3 \leq x/D_{PJ} \leq 8$; and downstream edge-region, $8 < x/D_{PJ} < 10$) are well

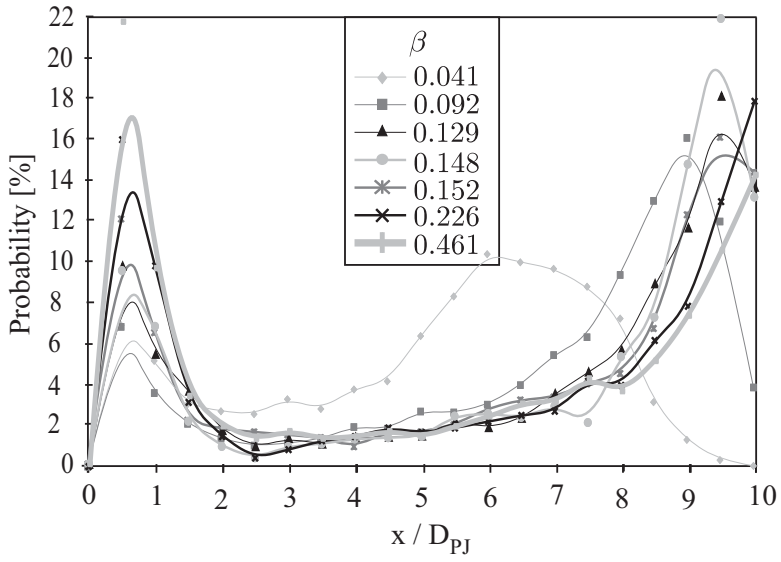

Figure 8.2: PDF of the axial location of small-cluster centroids for varying β.

defined and therefore used for the assessment. In general, these results highlight some of the trends seen in Figure 8.1. Clearly, the peaks in the near- and downstream edge-regions correspond to the large number of small-clusters immediately downstream from the nozzle and also at the bottom edge of the image (seen in Figure 8.1). It is also clear that the probabilities in the mid-region are independent from $\beta \geq 0.092$. For the case $\beta = 0.041$, the signal-to-noise towards the downstream edge-region is insufficient for the cluster determination methodology to work suitably. This is important, as it indicates that the cluster determination methodology has a lower limit of signal strength at which it will work, rather than an influence of β on the formation of particle clusters. The PDFs of the radial location of small-clusters, number of small-clusters, d_{eq} and P_c also show little variation in profiles, except for $\beta = 0.041$. Consequently, they provide little further information and therefore presented in Appendix A, rather than in the current chapter.

Figure 8.3 presents the average number of small-clusters ($\overline{N_{c,s}}$), average area of small-clusters ($\overline{A_{c,s}}$) and total area of small-clusters ($A_{total,s}$) located in the three regions in the flow for varying β and $G_{PJ}/G_{ANN(f)} = 6.19$. In the near-region, $\overline{N_{c,s}}$ can be

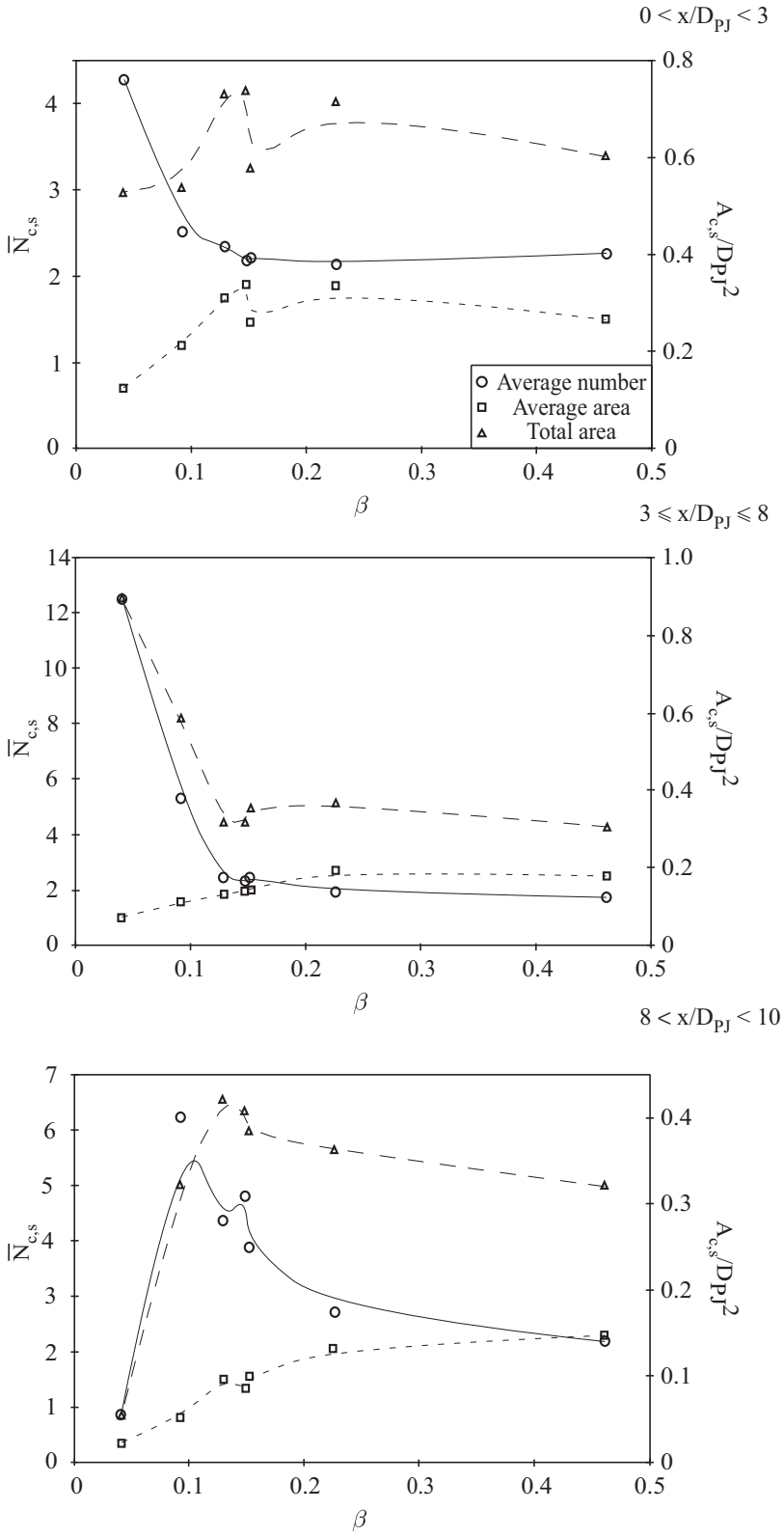

Figure 8.3: Plots of $\overline{N_{c,s}}$, $\overline{A_{c,s}}$ and $A_{total,s}$ located in the near-, mid- and downstream edge-regions for varying β.

approximated as a constant for $\beta \geq 0.092$. The areas for these cases also show little variation. However, for $\beta = 0.041$, $\overline{N_{c,s}}$ is significantly higher. Similar trends are seen in the mid-region, except for $\beta = 0.041$ and 0.092, which both have significantly higher values of $\overline{N_{c,s}}$. These results support previous findings that $\beta \geq 0.092$ has little influence on small-clusters, and the methodology has a minimum signal at which it will work. In the near-region, this threshold signal corresponds to $\beta \approx 0.041$. In the mid-region, the minimum signal has increased and corresponds to $\beta \approx 0.092$. The increase in minimum signal results from the spread of the jet and therefore the local reduction in light-scattering particles. In the downstream edge-region, the trend continues and the minimum signal at which the cluster determination methodology works successfully corresponds to $\beta \geq 0.226$. The low values for $\beta = 0.041$ result from the corresponding low signal strength influencing the planar nephelometry technique, as well as the cluster determination methodology.

The above results show β has little influence on small-cluster statistics if the initial value of β is above the minimum threshold for the methodology to work. However, these results are not isolated from the influence of G_{PJ}/G_{ANN}. Therefore the data presented in the current chapter are compared with those from Chapter 7. Figure 8.4 is a series of plots of $\overline{N_{c,s}}$ and $\overline{N_{c,s}}$ in the three regions of the flow. The data from the current chapter and Chapter 7 are presented in terms of changing G_{PJ}/G_{ANN}. The continuation of trends between constant β cases and constant $G_{PJ}/G_{ANN(f)}$ are not as clear as was shown in the similar comparisons in Chapter 5. However, the trends are still present, and with the exception of the cases with $\beta \leq 0.129$ ($G_{PJ}/G_{ANN} \geq 5.00$), show that the influence of β on small-clusters corresponds with the influence of G_{PJ}/G_{ANN}.

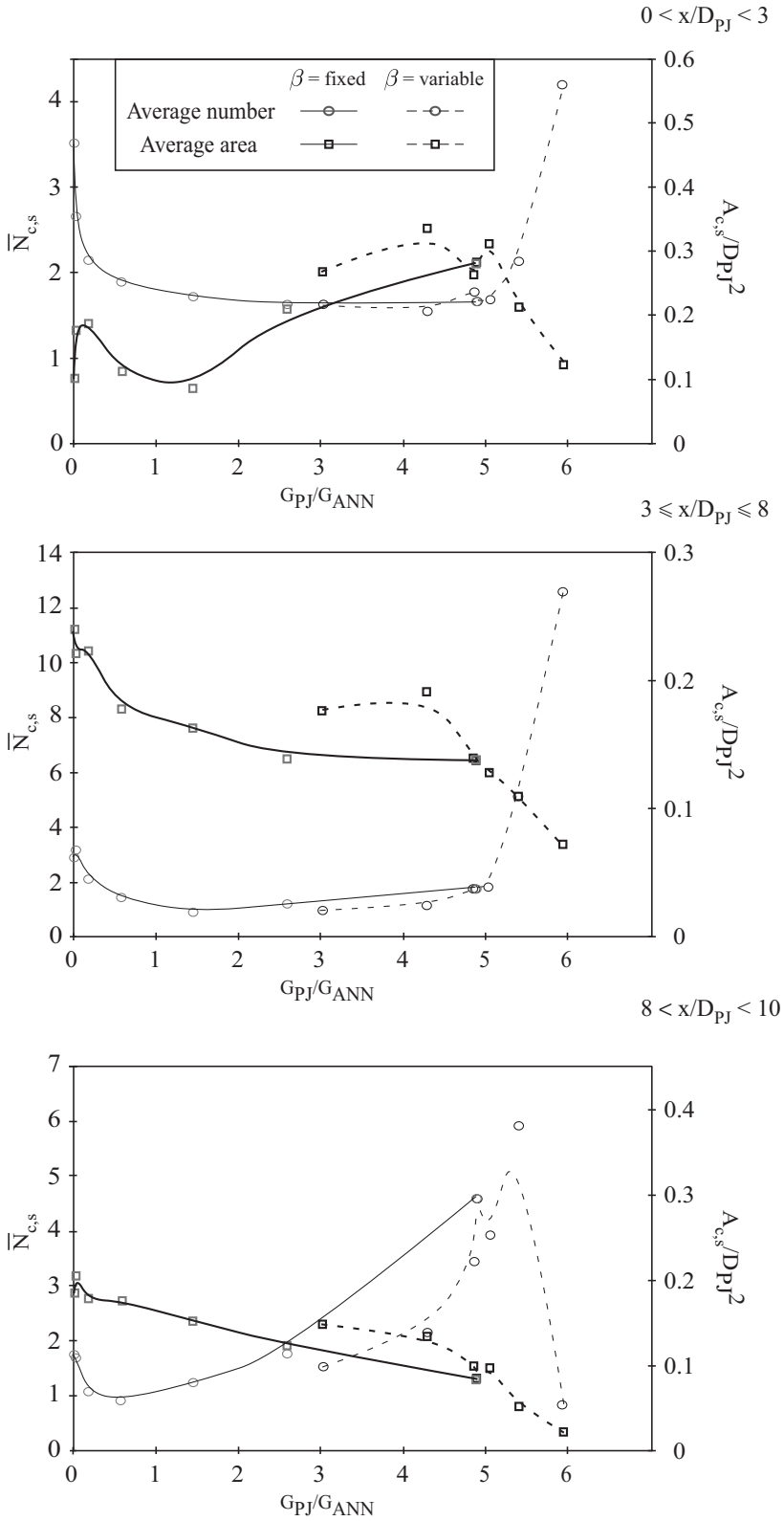

Figure 8.4: Plots of $\overline{N_{c,s}}$ and $\overline{A_{c,s}}$ located in the near-, mid- and downstream edge-regions for constant β (solid lines) and $G_{PJ}/G_{ANN(f)} = 6.19$ (dashed lines).

8.2.2 Large-Clusters

Figure 8.5 shows a series of images for varying β. This figure is similar to that of Figure 8.1, but for large-clusters. Again, the scale for each image is optimised separately. It can be seen that for $\beta \geq 0.129$, the distribution of large-clusters does not appear to change significantly. The variations in images for $\beta < 0.129$ result from the insufficient signal strength.

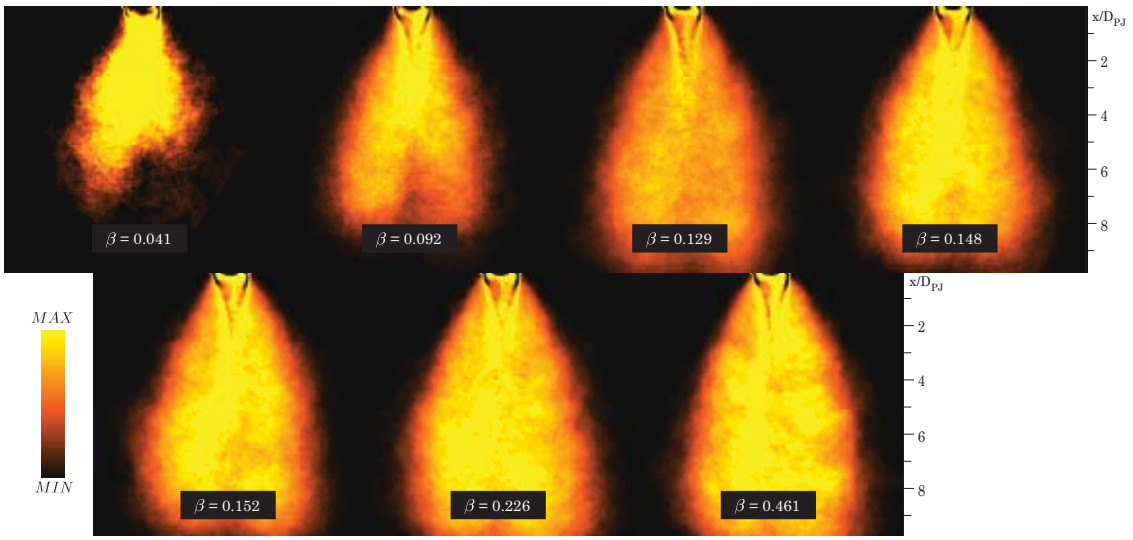

Figure 8.5: A planar PDF of the large-clusters for varying β.

The PDF of the cluster centroids in the axial direction are shown in Figure 8.6. This plot further supports finding that there is a minimum signal strength for the cluster determination methodology to work successfully. Excluding $\beta = 0.041$ and in part $\beta = 0.091$, the axial locations of large-cluster centroids are independent from β. Due to the low number of large-clusters per image, the PDFs of large-cluster numbers do not provide any new information. Therefore not included or discussed further. The remaining PDFs are presented in Appendix A.

The plots of $\overline{N_{c,l}}$, $\overline{A_{c,l}}$ and $A_{total,l}$ for the three regions in the flow are presented in Figure 8.7. These plots show similar trends to those for small-clusters; β has little influence on large-clusters if the signal strength is sufficiently high.

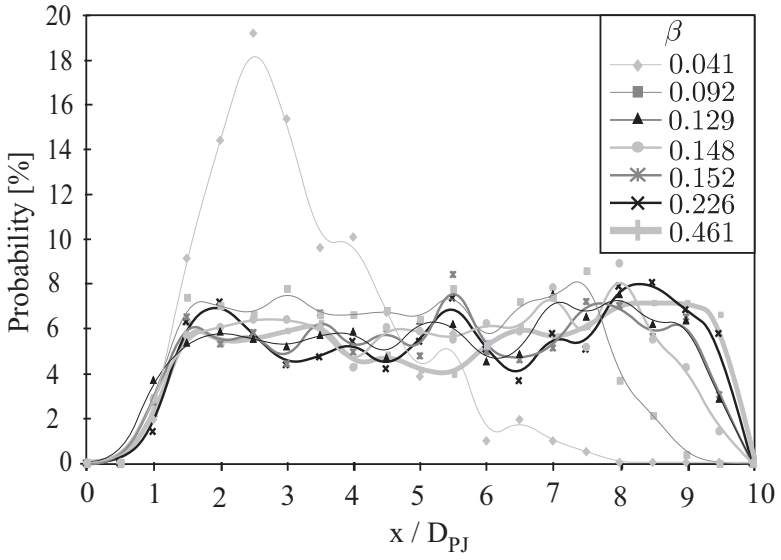

Figure 8.6: PDF of the axial location of large-cluster centroids for varying β.

The comparison of results for fixed and variable β for $\overline{N_{c,l}}$ and $\overline{A_{c,l}}$ are shown in Figure 8.8. Once again, it can be seen that there is a continuation of trends when β is sufficiently high. This is clearly evident in the mid-region, but in the near- and downstream edge-regions there is greater divergence in trends. These divergences indicate that the influence of β may not result just from variations in momentum, but actually from the interplay between the particles and the fluid. Nonetheless, any interplay between phases would be small, if it exists, in the region $0 < x/D_{PJ} < 10$.

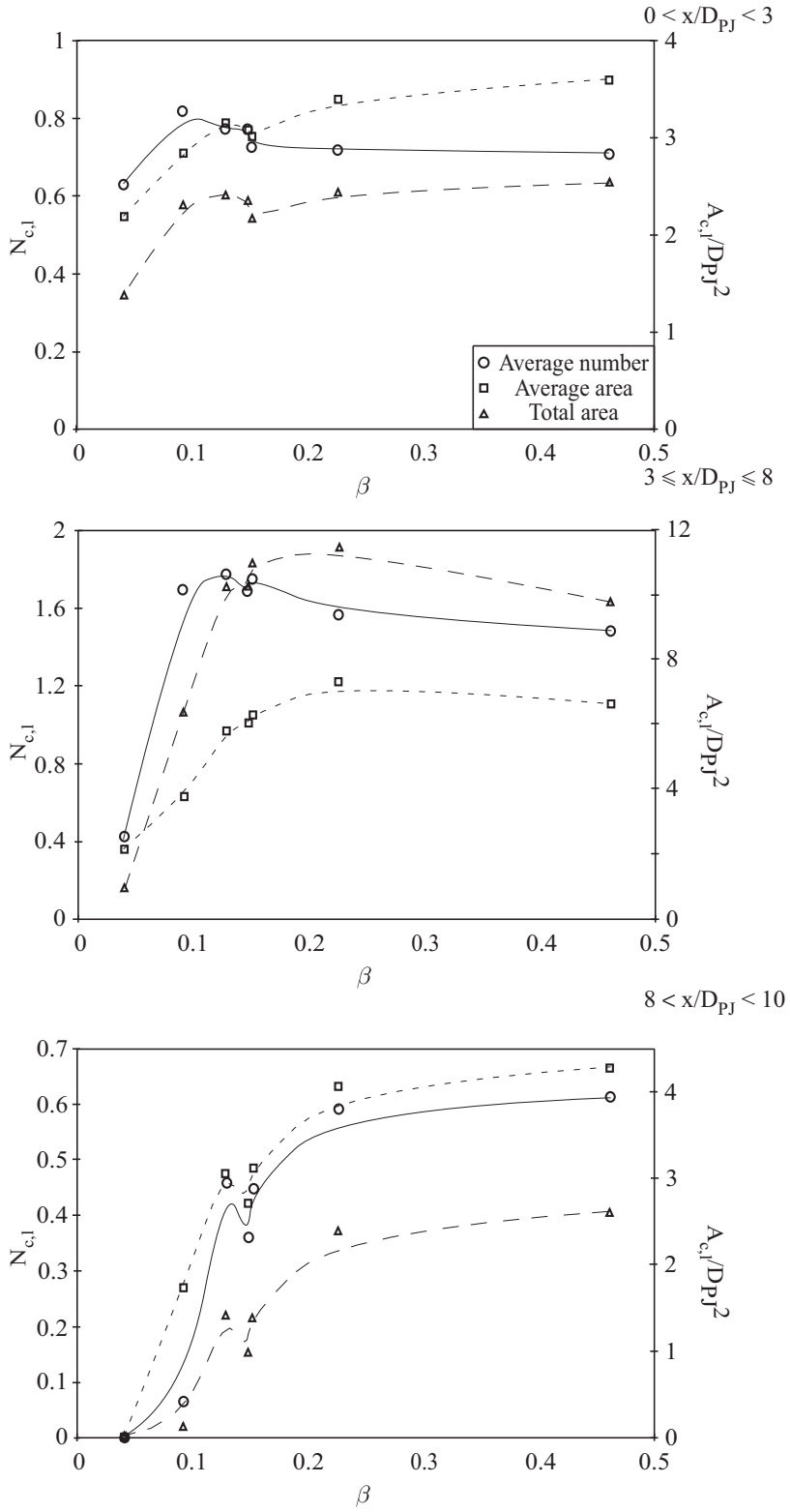

Figure 8.7: Plots of $\overline{N_{c,l}}$, $\overline{A_{c,l}}$ and $A_{total,l}$ located in the near-, mid- and downstream edge-regions for varying β.

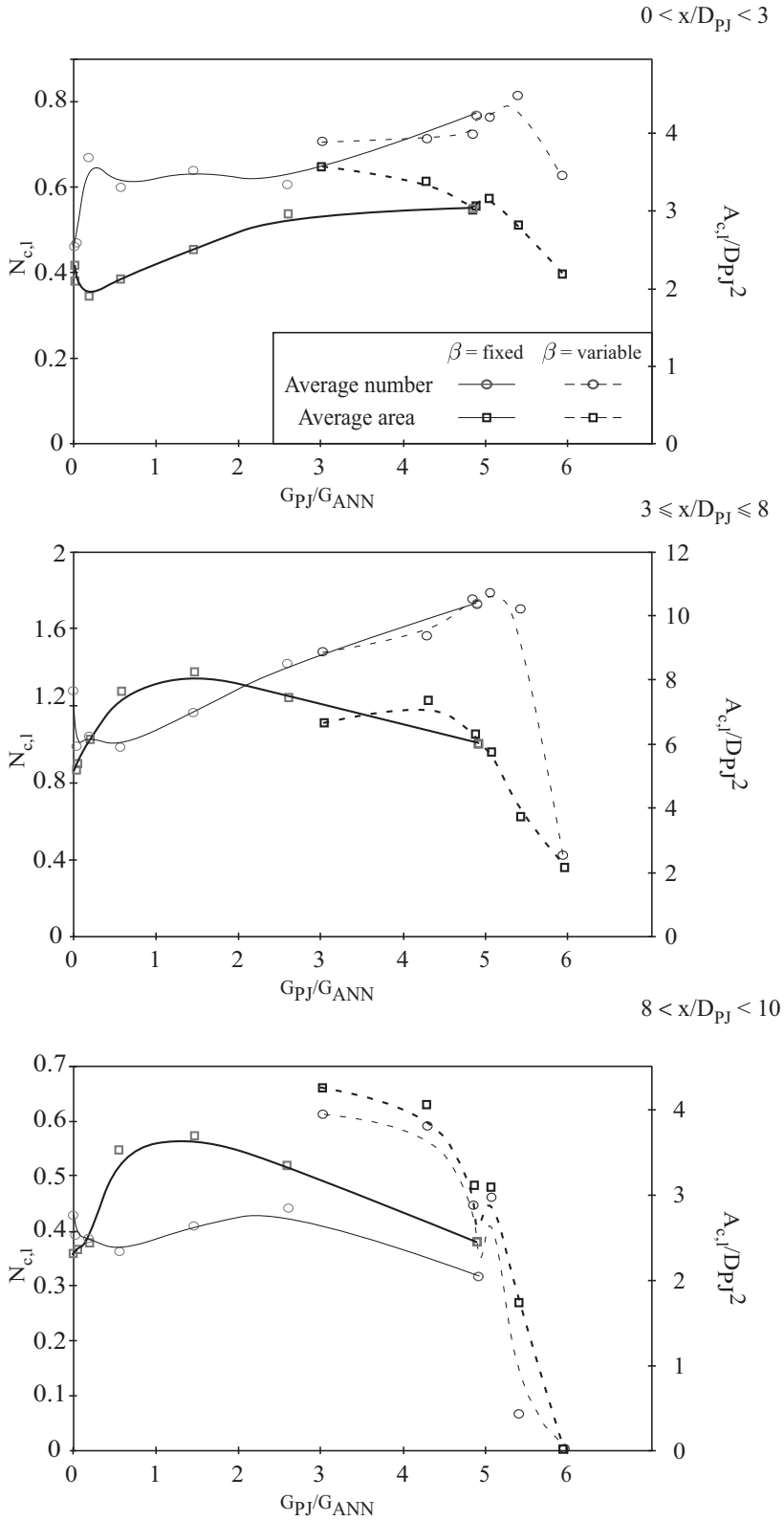

Figure 8.8: Plots of $\overline{N_{c,l}}$ and $\overline{A_{c,l}}$ located in the near-, mid- and downstream edge-regions for constant β (solid lines) and $G_{PJ}/G_{ANN(f)} = 6.19$ (dashed lines).

8.3 Conclusions

The influences of β on the characteristics of particle clusters in the first 10 nozzle diameters of a particle-laden jet employing a Precessing Jet nozzle has been investigated. Plots of $\overline{N_c}$ and $\overline{A_c}$, as well as probability density functions (PDFs) of cluster locations, are presented for both small- and large-clusters.

In Chapter 5 it was found that the influence of β on the mean distribution of particles corresponds with a variation in G_{PJ}/G_{ANN}. In the current chapter, the results show that the influence of β on both small- and large-clusters is very small, and these variations also correspond primarily from variations in G_{PJ}/G_{ANN}, rather than increasing the loading of a second phase. However, these results are limited to $0 < x/D_{PJ} < 10$. It is still possible that the transfer of momentum between phases becomes a stronger influence on mean and instantaneous particle distributions further downstream.

The other major finding from the current chapter is that there exists a minimum signal strength required for the cluster determination methodology to work successfully. Low signal strength corresponds to a low dynamic range on the CCD. Consequently, the difference in signal magnitude between the instantaneous image and the mean is less than for cases with higher initial signal strength. As the methodology to identify clusters is based on a comparison of the instantaneous image (smoothed) and the mean, when the signal strength is low, and therefore the difference is low, the methodology fails to correctly identify clusters. For the current configuration, $\beta = 0.041$ in the near-region corresponds to the minimum signal strength. Further downstream, β must be higher to ensure the local signal strength is sufficient for the methodology.

Chapter 9

Conclusions

It was discussed in Chapter 1 that jet precession can be used in gas-fired rotary cement kilns to improve product quality, reduce fuel consumption and reduce production of harmful emissions (specifically NO_X). However, due to the differences between the combustion and fluid mechanics of single-phase flows and particle-laden flows, the improvements resulting from jet precession in gas-fired systems may not necessarily extend to particle-laden flows. Since most rotary fired cement kilns are pulversied fuel (PF) fired, and there is a need to reduce the harmful emissions produced from combustion, there is a desire to apply the benefits of jet precession seen in gas-fired rotary cement kilns to PF fired kilns.

The aim of the current research project is to increase the body of knowledge relating to the influence of jet precession on the distribution of particles. Specifically, this thesis assesses the extent to which jet precession can be used to control the mean and instantaneous particle distributions in particle-laden jet flows.

From the literature review presented in Chapter 1, the following four specific questions were identified:

- How does the ratio G_{PJ}/G_{ANN} influence the mean and fluctuating distributions of particles?
- How does the ratio G_{PJ}/G_{ANN} influence the characteristics of particle clusters?
- How does β influence the mean and fluctuating distributions of particles?
- How does β influence the characteristics of particle clusters?

In order to answer these questions, experimental equipment was designed, and both diagnostic techniques and processing methodologies were developed. Experiments were conducted in a windtunnel designed to simulate a PF fired rotary cement kiln. A technique called planar nephelometry was developed in parallel with this research, and use to obtain planar instantaneous measurements of particle surface areas. These particles simulate the PF (coal). A method to identify and quantify large-scale particle clusters from planar images has been developed and used to provide statistical data on the particle clusters formed in the jet flows in the first 10 nozzle diameters.

A series of objectives were presented in Chapter 1, and have been used to answer the research questions. These objectives are as follows:

- To quantify the influence G_{PJ}/G_{ANN} on the mean and fluctuating distributions of particles.
- To quantify the effect of β on the mean and fluctuating distributions of particles.
- To develop a method of identifying and quantifying particle clusters.
- To quantify the influence of G_{PJ}/G_{ANN} on the characteristics of particle clusters.
- To quantify the effect of β on the characteristics of particle clusters in Precessing Jet flows.

The current chapter provides a summary of the work in relation to addressing the aforementioned objectives.

Objective 1

To quantify the influence of G_{PJ}/G_{ANN} on the mean and fluctuating distributions of particles

Chapter 4 presents mean and fluctuating components of the particle distributions in the first 10 nozzle diameters of a particle-laden PJ nozzle, for $0.00 \leq G_{PJ}/G_{ANN} \leq 4.90$. These results indicate a particle-laden Precessing Jet flow has three regimes, based on the momentum ratio G_{PJ}/G_{ANN}. These regimes can be classified as follows:

- Annular-dominated regime, $G_{PJ}/G_{ANN} < 0.18$;
- transition, $0.18 \lesssim G_{PJ}/G_{ANN} \lesssim 1.46$; and,
- PJ-dominated regime, $G_{PJ}/G_{ANN} \gtrsim 1.46$.

The reference annular flow case occurs for $G_{PJ}/G_{ANN} = 0.00$. This case is simply a particle-laden annular jet with a bluff body flow. There is very little spread in the flow, such that the concentration halfwidth at $x/D_{PJ} \approx 10$ is no greater than immediately downstream from the nozzle exit. At $x/D_{PJ} = 7$ the halfwidth is $1.62D_{PJ}$. The centreline concentration peak is located at $x/D_{PJ} \approx 2.66$, and downstream from this location the radial profiles approach Gaussian. The relative fluctuations, $S'/\overline{S}$, measured along the nozzle centreline steadily increase downstream from the peak, and at $x/D_{PJ} = 9$, $S'/\overline{S} \approx 0.83$, compared with $S'/\overline{S} \approx 0.50$ at the peak.

Small increases in the momentum ratio for $G_{PJ}/G_{ANN} < 0.18$ results in the bluff body effect being reduced significantly, if not completely. Compared with the reference case, the centreline concentration peak is shifted further downstream to $x/D_{PJ} = 3.37$ and the jet is narrower, but by less than 20%. This indicates that the mean particle distribution is elongated. The fluctuations have also reduced, such that at $x/D_{PJ} = 9$, $S'/\overline{S} \approx 0.72$ compared with $S'/\overline{S} \approx 0.48$ at the peak.

In the transition regime, the influence of jet precession is no longer negligible, but the annular jet still has a strong influence on the particle distributions. The centreline concentration peak is shifted towards the nozzle exit plane and the halfwidths downstream from the peak increase, indicating that the jet becomes wider and shorter with increasing G_{PJ}/G_{ANN}. However, the jet only becomes wider and shorter than $G_{PJ}/G_{ANN} = 0.00$ for $G_{PJ}/G_{ANN} \gtrsim 0.58$. For the case $G_{PJ}/G_{ANN} = 0.58$ the peak is located at $x/D_{PJ} = 2.44$ and the halfwidth at $x/D_{PJ} = 7$ is $1.48D_{PJ}$. Increasing G_{PJ}/G_{ANN} in the transition regime also results in an increase in the relative fluctuations of the mean particle distributions, but again, it is only for $G_{PJ}/G_{ANN} \geq 0.58$ that the relative fluctuations are greater than the reference case. For $G_{PJ}/G_{ANN} = 0.56$ and at $x/D_{PJ} = 9$, $S'/\overline{S} \approx 0.93$.

In the PJ-dominated regime, the jet continues to become shorter and wider and the fluctuations also increase. For $G_{PJ}/G_{ANN} = 4.90$, the centreline concentration peak is located at $x/D_{PJ} = 1.43$, the halfwidth at $x/D_{PJ} = 7$ is $5.68D_{PJ}$, and at $x/D_{PJ} = 9$, $S'/\overline{S} \approx 3.86$.

Objective 2

To quantify the effect of β on the mean and fluctuating distribution of particles

The influence of β on the mean and fluctuating component of the distributions of particles is presented in Chapter 5. Experiments were conducted with fixed $G_{PJ}/G_{ANN(f)} = 6.19$ and therefore G_{PJ}/G_{ANN} varied. The general findings from this chapter indicate that increasing β has little influence on the jet distribution upstream from the centreline concentration peak. Downstream from the peak, increasing β results in an elongation of the jet. However, the results also indicate that the influence of β correlates with the variations in G_{PJ}/G_{ANN} Therefore, β has very little influence on the mean distribution of particles in the first 10 nozzle diameters, except through the addition of jet momentum.

Objective 3

To develop a method of identifying and quantifying particle clusters

A methodology to identify and quantify large-scale particle clusters is presented in Chapter 6. The methodology uses a comparison of the mean image with an instantaneous planar image that has been smoothed by some value L. This method is subject to the amount of smoothing to the instantaneous image and therefore a sensitivity study on the influence of L was conducted. Results from the sensitivity study were limited to constant values of L ranging from $\frac{1}{8}D_{PJ} \leq L \leq 2D_{PJ}$. The value D_{PJ} was used as a base for L as D_{PJ} can be used as an approximation of the large-scale structures in the flow, which correspond to the size of the clusters that are the focus of the current work.

From the sensitivity study it was determined that there is a moderate sensitivity to L. A list of the findings is clearly presented in Section 6.4 and therefore not reproduced here. For the current research and in the range $0 \leq x/D_{PJ} \leq 10$, the optimal value appears to be $L = \frac{1}{2}D_{PJ}$. The application of this methodology has enabled statistical analysis of clusters to address objectives 4 and 5.

It was shown in Chapter 8 that there is a minimum signal strength at which the methodology will work successfully. For the current work the minimum signal strength corresponds to $\beta = 0.041$ in the near-region and $\beta = 0.092$ in the mid-region. The results from the methodology are subject to greater error near to the edges of the image due to clipping.

Objective 4

To quantify the influence of G_{PJ}/G_{ANN} on the characteristics of particle clusters

Chapter 7 presents particle cluster data, in the first 10 nozzle diameters of a particle-laden PJ nozzle, for $0.00 \leq G_{PJ}/G_{ANN} \leq 4.90$. Particle clusters have been separated into two groups: small-clusters, with $\frac{1}{10}D_{PJ} \times \frac{1}{10}D_{PJ} \lesssim A_c \lesssim D_{PJ} \times D_{PJ}$ (100 pixels $\leq A_c \leq$ 10,000 pixels); and large-clusters, with $A_c \geq D_{PJ} \times D_{PJ}$ ($A_c \geq 10,000$ pixels). The analysis of these statistics was conducted over three axial regions; the near-region ($0 < x/D_{PJ} < 3$), the mid-region ($3 \leq x/D_{PJ} \leq 8$) and the downstream edge-region ($8 < x/D_{PJ} < 10$). As described for Objective 1, the results can be classified into annular-dominated ($0.00 \geq G_{PJ}/G_{ANN} < 0.18$), transition ($0.18 \lesssim G_{PJ}/G_{ANN} \lesssim 1.46$) and PJ-dominated regimes ($G_{PJ}/G_{ANN} \gtrsim 1.46$).

Throughout the annular-dominated regime cases there is little variation in the results for either small- or large-clusters. The number of small-clusters decreases downstream, but $\overline{A_{c,s}}$ does not vary greatly. For the reference annular flow case of $G_{PJ}/G_{ANN} = 0.00$, $\overline{N_{c,s}} = 3.52$, 2.87 and 1.75, for the near-, mid- and downstream edge-regions respectively. Small-cluster centroids are more likely to be located near to the jet edge. There is almost an order of magnitude fewer large-clusters than small-clusters throughout the flow. Unlike small-clusters, the radial locations of large-cluster centroids have Gaussian distributions, but centred on the side with the higher initial particle distribution. These large-clusters are strongly influenced by the annular jet.

For the transition regime cases, relative to the annular-dominated regime cases, there are fewer small-clusters and $\overline{A_{c,s}}$ is typically smaller too. The value of $\overline{A_{c,s}}$ for all regions in the flow investigated decrease with increasing G_{PJ}/G_{ANN} by approximately 25% compared to the reference case, while the values of $\overline{N_{c,s}}$ decreases by approximately 50%. In the transition regime cases, small-cluster centroids have similar locations to those for the annular-dominated regime, although there are still some minor differences.

The PDFs of cluster number, d_{eq} and P_c for both small- and large-clusters do not vary significantly in the transition regime.

The influence of jet precession on large-clusters in the transition regime has very little influence, except the radial location in the downstream edge-region becomes wider and flatter than for annular-dominated regime cases. The radial locations of large-cluster centroids are sensitive to jet precession in the transition regime, whereas the small-clusters are not. There are also fewer large-clusters in the mid- and downstream edge-regions, although this reduction is typically less than 15%. However, throughout the transition regime, $\overline{N_{c,l}}$ does not vary significantly. The value of $\overline{A_{c,l}}$ increases with G_{PJ}/G_{ANN} in both annular-dominated and transition regimes.

In the PJ-dominated regime, the influence of jet precession on particle clusters is significant. Compared with $G_{PJ}/G_{ANN} = 0.00$, there are fewer small-clusters in the near- and mid-regions. In the mid- and downstream edge-regions, $\overline{A_{c,s}}$ decreases with increasing G_{PJ}/G_{ANN} by approximately 50% for $G_{PJ}/G_{ANN} = 4.90$ compared with the reference case, whereas there is a 100% increase in $\overline{A_{c,s}}$ in the near-region for the same cases. The location of small-clusters generated in PJ-dominated regime exhibit a Gaussian distribution, centred near to the jet centreline.

The large-clusters are also strongly influenced by jet precession in the PJ-dominated regime. In the near-region, $\overline{N_{c,l}}$ and $\overline{A_{c,l}}$ increase with increasing G_{PJ}/G_{ANN}. However, in both mid- and downstream edge-regions $\overline{A_{c,l}}$ decreases. Therefore, compared with the reference case, there are more large-clusters, but these clusters have smaller average areas. The radial distribution of large-cluster centroids becomes wider with increasing G_{PJ}/G_{ANN} in the PJ-dominated regime, which is analogous to the mean particle distribution.

Objective 5

To quantify the effect of β on the characteristics of particle clusters in Precession Jet flows

The influence of β on particle cluster characteristics is presented in Chapter 8. As discussed above with Objective 2, β has very little influence on the mean distribution of particles in the first 10 nozzle diameters, except through the addition of jet momentum. The results in Chapter 8 present similar findings for both small- and large-clusters.

Chapter 10

Future work

The planar nephelometry technique used in this research is the subject of ongoing research. Specifically, improving the accuracy and quality of the data by the use of shot-to-shot correction is being assessed. There are also plans to further the technique to differentiate between large and small particles. Further developments towards providing a technique that produces absolute instantaneous planar concentration measurement are still possible.

The cluster determination methodology has demonstrated sufficient usefulness to warrant further work. It is suggested that either post-processing of existing data from, for example, Longmire and Eaton [1992] or Zimmer et al. [2002a,b] may provide further validation of the technique. As flow length-scales are not necessarily constant through a jet flow, neither are the sizes of clusters. Therefore, variation to the current technique may include using a smoothing value that varies with axial location. The suitability of the methodology to preferentially identify clusters based on size should also be assessed, as this may indicate a more advanced application of the methodology, or a limiting restriction.

The shape of clusters is likely to be an important characteristics for combustion. However, cluster shape was not investigated in the current work. It is suggested that determination of a suitable means to quantify and analysis cluster shape is needed. Furthermore, assessing the influence of cluster shape on combustion performance is also a field of research with great potential.

The motivation of the current work was to further enable improved designs of PJ nozzles for PF fired rotary cement kilns. A comparison of the existing work with combustion data would be greatly beneficial. Similarly, as there is a greater body of knowledge relating to the understanding of single-phase PJ flows, a direct comparison of single-phase and particle-laden flows should be conducted. This may require an additional technique to accurately measure both phases. It is suggested that additional assessment of length-scales and velocity profiles should be conducted.

The experiments conducted for the current research were limited to $G_{PJ}/G_{ANN} \leq 4.90$ and a single range of particles with $0.03 \geq Sk \geq 0.51$. Further analysis with a larger range of G_{PJ}/G_{ANN}, including variations to G_{ANN} would further the understanding of jet precession on particle distributions. In addition, investigating the influence of Sk is suggested, but would require particles with a much narrower size distribution.

It was suggested in Chapter 5 that an investigation into the influence of β with G_{PJ}/G_{ANN} constant, and thus $G_{PJ}/G_{ANN(f)}$ varying be conducted. This would assess whether the small variations that are found with increasing β result from the addition of particle mass loading, or an increase in total momentum. Such an investigation should incorporate data from beyond $x/D_{PJ} = 10$ as well.

Finally, it is suggested that understanding the influence of two-phase flows on the length-scale in the flow is important. In a precessing flow, there are numerous length scales that could be used to determine Sk. However, which length scales are appropriate for certain applications are not yet known.

Appendix A

Further results of the influence of particle mass loading on particle clusters

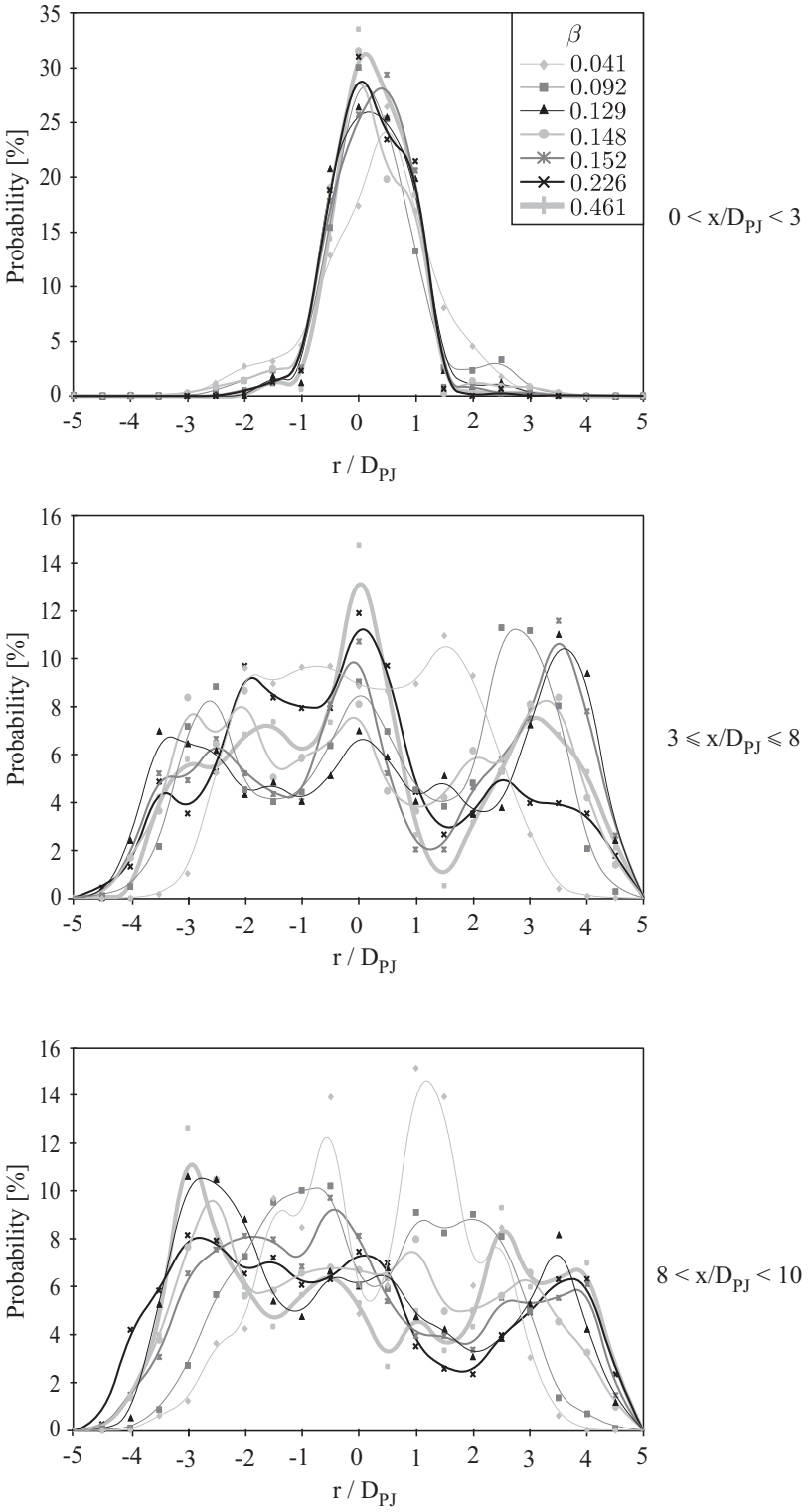

Figure A.1: PDFs of the radial location of small-cluster centroids located in the near-, mid- and downstream edge-regions for varying β.

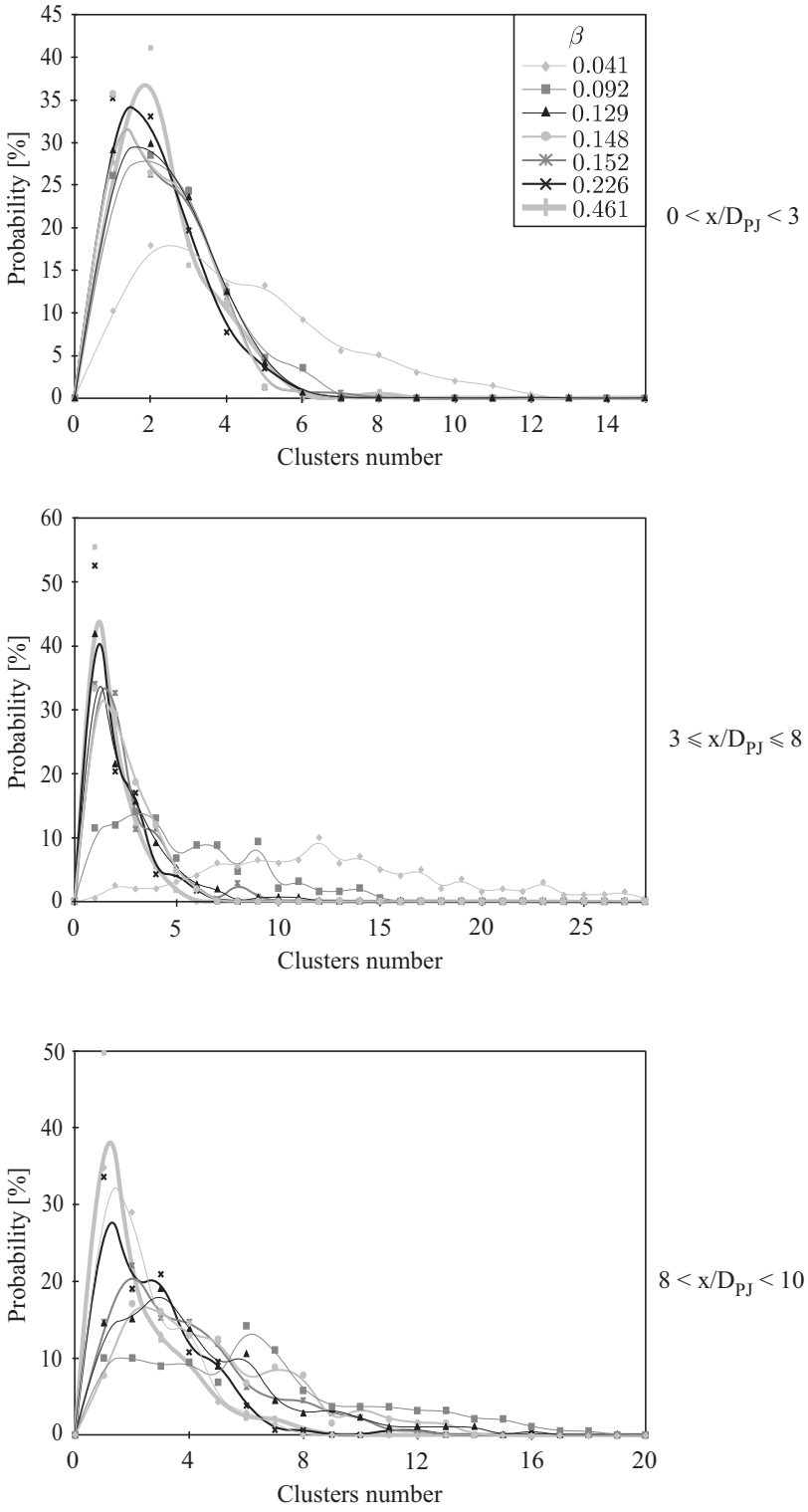

Figure A.2: PDFs of the number of small-clusters located in the near-, mid- and downstream edge-regions for varying β.

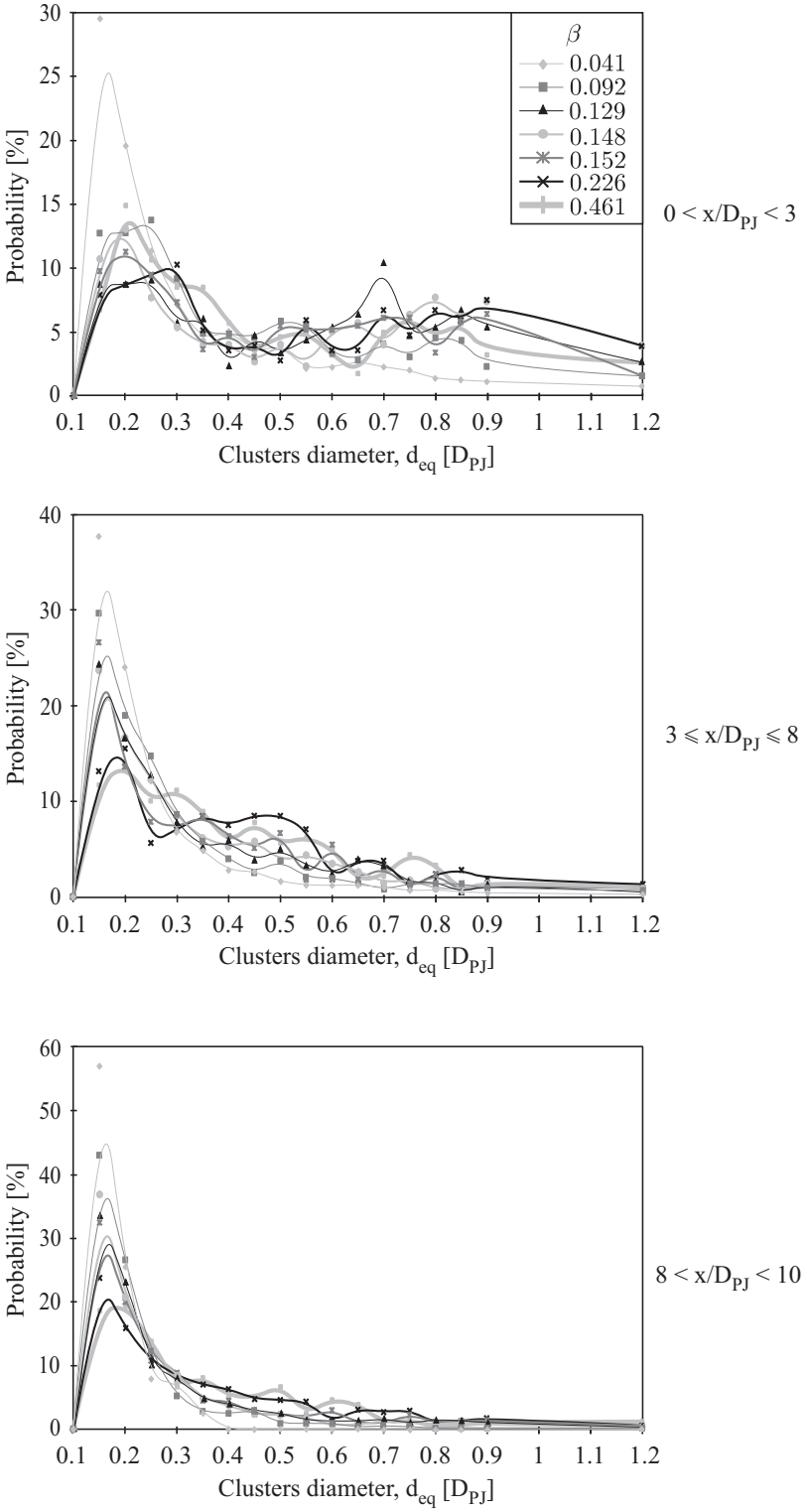

Figure A.3: PDFs of d_{eq} for small-clusters located in the near-, mid- and downstream edge-regions for varying β.

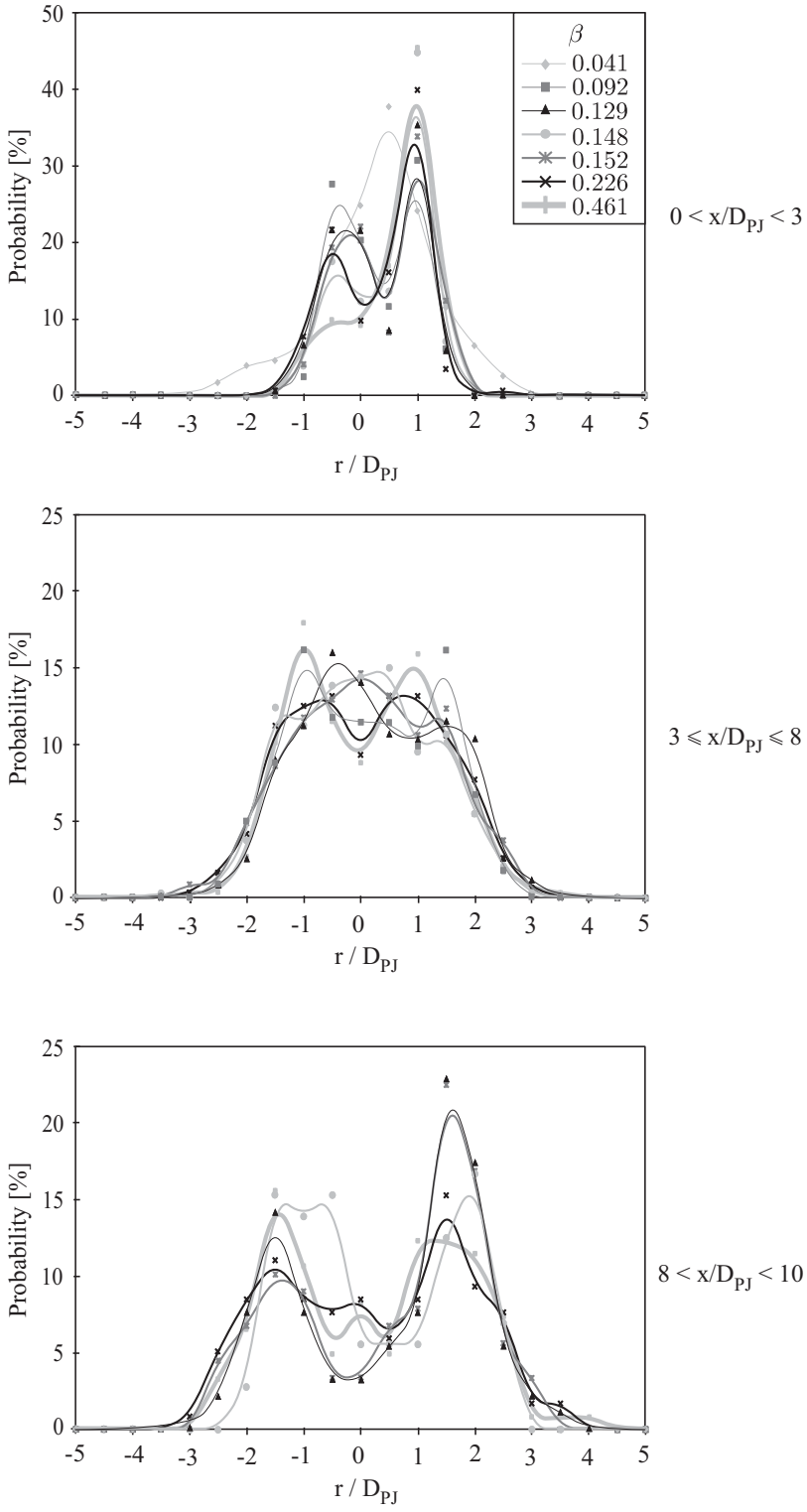

Figure A.4: PDFs of the radial location of large-cluster centroids located in the near-, mid- and downstream edge-regions for varying β.

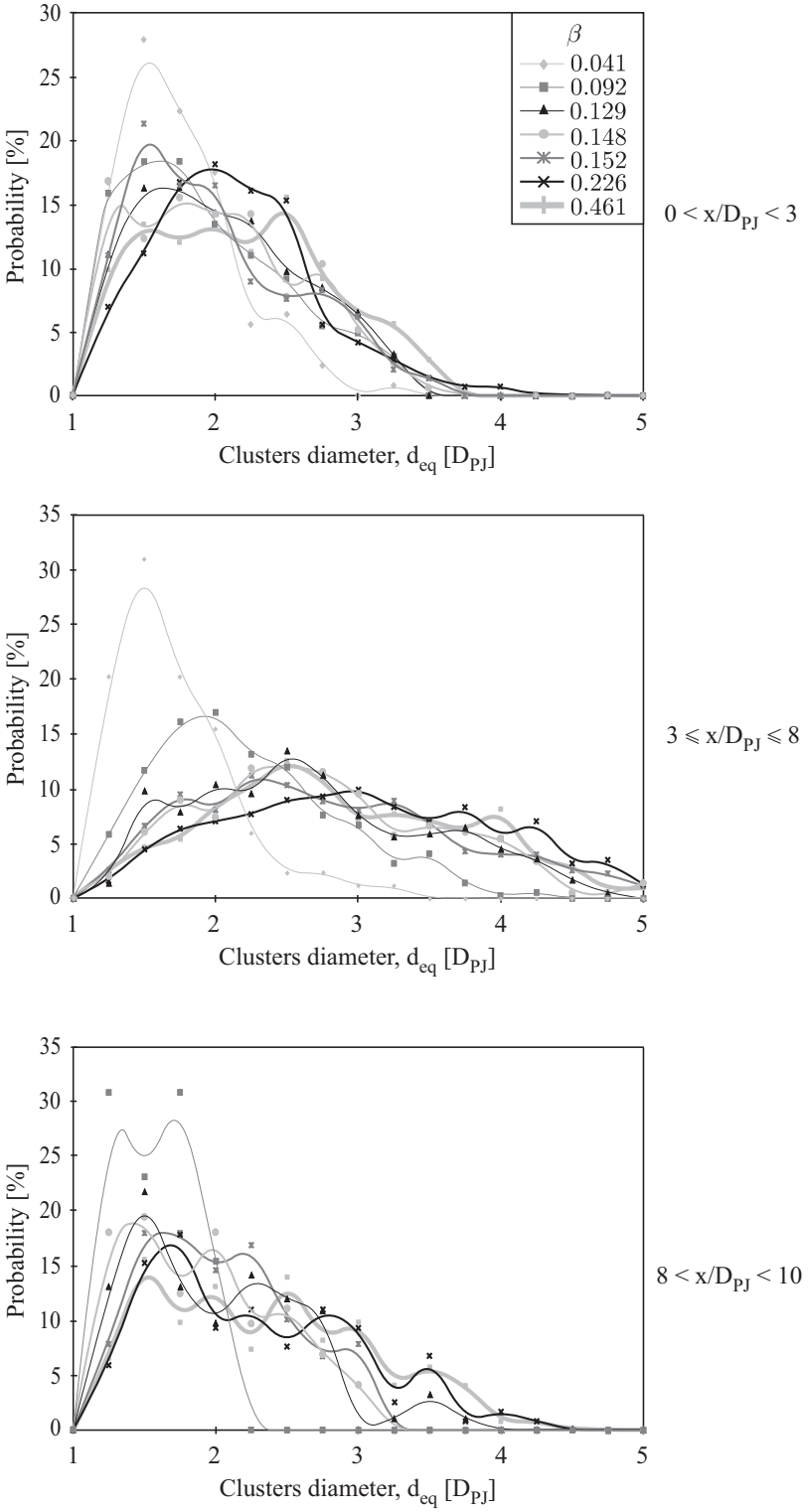

Figure A.5: PDFs of d_{eq} for large-clusters located in the near-, mid- and downstream edge-regions for varying β.

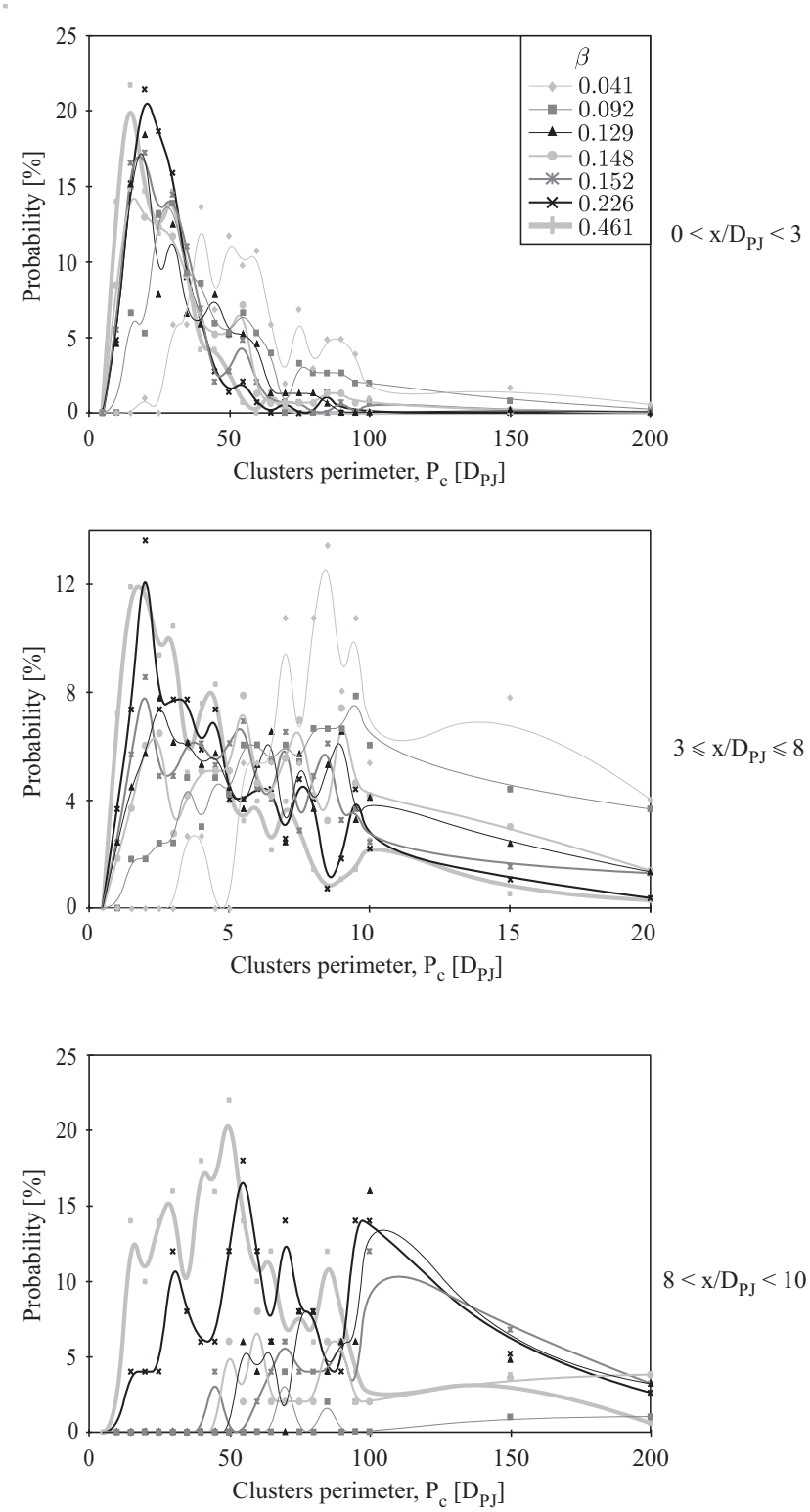

Figure A.6: PDFs of P_c of large-clusters located in the near-, mid- and downstream edge-regions for varying β.

Publications

Publications arising from the current work:

[1] Birzer, C.H., Kalt, P.A.M., and Nathan, G.J., 2009, The Influence of Jet Precession on Near Field Particle Distributions, International Journal of Multiphase Flow, 35, 288-296.

[2] Birzer, C.H., Kalt, P.A.M., and Nathan, G.J., 2008, A Methodology for Measuring Particle Clustering From Planar Images, 11th International Conference on Multiphase Flow in Industrial Plants.

[3] Birzer, C.H., Kalt, P.A.M., and Nathan, G.J., 2008, A Statistical Analysis of a Technique to Measure Large-Scale Particle Clusters, 5th Australia Conference on Laser Diagnostics in Fluid Mechanics and Combustion.

[4] Kalt, P.A.M., Birzer, C.H., and Nathan, G.J., 2007, Corrections to Facilitate Planar imaging of Particle Concentration in Particle-Laden Flows Using Mie-Scattering Part 1: Collimated Laser Sheets, 46, 23, 5823-5834.

[5] Birzer, C.H., Kalt, P.A.M., Nathan, G.J., and Smith, N.L., 2005, Planar Measurements of the Distribution of Particles in a Two-Phase Precessing Jet Flow, 5th Asia-Pacific Conference on Combustion.

[6] Birzer, C.H., Kalt, P.A.M., Smith, N.L., and Nathan, G.J., 2005, Particle Image Velocimetry in the Near Field of a Particle-Laden Precessing jet Flow, 4th Australia Conference on Laser Diagnostics in Fluid Mechanics and Combustion.

[7] Kalt, P.A.M., and Birzer, C.H., 2005, Calibrtations for Planar Laser Nephelometry in Densely Seeded Two-Phase Flows, 4th Australia Conference on Laser Diagnostics in Fluid Mechanics and Combustion.

[8] Birzer, C.H., Kalt, P.A.M., Nathan, G.J., and Smith, N.L., 2004, The Influence of Mass Loading on Particle Distribution in the Near Field of a Co-Annular Jet, 15th Australasian Fluid Mechanics and Combustion Conference.

Bibliography

T. Abbas, P. Costen, F.C. Lockwood, and C.A. Romo-Millares. The effect of particle size on NO in a large-scale pulverised coal-fired laboratory furnace: Measurements and modeling. *Combustion and Flame*, 93:316–326, 1993.

S. Aggarwal. Relationship between Stokes number and intrinsic frequencies in particle-laden flow. *AIAA Journal*, 32(6):1322–1324, 1993.

A.M. Al Taweel and J. Landau. Turbulence modulation in two-phase jets. *International Journal of Multiphase Flow*, 3:341–351, 1977.

D. Albagli and Y. Levy. Two-phase flow measurements in confined coaxial jets. *International Journal of Multiphase Flow*, 16(5):929–932, 1990.

I. Ayranci, G. Pinguet, D. Escudié, N. Selçuk, R. Vaillon, and F. André. Effect of particle polydispersity on particle concentration measurement by using laser doppler anemometry. *Experimental Thermal and Fluid Science*, 31:839–847, 2007.

C. Bauer. PYRO-JET burners to reduce NOx emissions - Current development and practical experience. *World Cement*, (4):118–124, 1990.

H.A. Becker. Mixing, concentration fluctuations, and marker nephelometry. In B.E. Launder, editor, *Studies in Convection*, volume 2. Academic Press, 1977.

H.A. Becker. Concentration fluctuations in ducted turbulent jets. *Combustion and Flow*, pages 791–798, 1966.

H.A. Becker, H.C. Hottel, and G.C. Williams. Concentration intermittency in jets. In *Tenth Symposium (International) on Combustion*, pages 1253–1263. The Combustion Institute, 1965.

C.H. Birzer, P.A.M. Kalt, G.J. Nathan, and N.L. Smith. The influence of mass loading on particle distribution in the near field of a co-annular jet. In *15th Australasian Fluid Mechanics Conference*, 2004.

C.H. Birzer, P.A.M. Kalt, G.J. Nathan, and N.L. Smith. Planar measurements of the distribution of particles in a two-phase precessing jet flow. In *5th Asia-Pacific Conference on Combustion*, 2005.

C.H. Birzer, P.A.M. Kalt, and G.J. Nathan. A methodology for measuring particle clustering from planar images. In *11th International Conference on Multiphase Flow in Industrial Plants*, 2008a.

C.H. Birzer, P.A.M. Kalt, and G.J. Nathan. A statistical analysis of a technique to measure large-scale particle clusters. In *5th Australian Conference on Laser Diagnostics in Fluid Mechanics and Combustion*, 2008b.

C.H. Birzer, P.A.M. Kalt, and G.J. Nathan. The influences of jet precession on near field particle distributions. *International Journal of Multiphase Flow*, 35:288 – 296, 2009.

C.T. Bowman. Control of combustion-generated nitrogen oxide emissions: Technology driven by regulations. In *Twenty-Fourth Symposim (International) on Combustion*, pages 859–878. The Combustion Institute, 1992.

P. Bradshaw and R. C. Pankhurst. The design of low-speed wind tunnels. Aero Report 1039, NPL Aero, 1964.

H.M. Cassel and I. Leibman. The cooperative mechanism in the ignition of dust dispersions. *Combustion and Flame*, 3:467–475, 1958.

R. Chein and J.N. Chung. Effects of vortex pairing on particle dispersion in turbulent shear flows. *Int. J. Mulitphase Flow*, 13(6):785–802, 1987.

A.M. Cormack. Representation of a function by its line integra with some radiological applications. *Journal of Applied Physics*, 34:2722–2727, 1963.

M. Costa, S. Godoy, F.C. Lockwood, and J. Zhou. Initial stages of the devolatilization of pulverised coal in a turbulent jet. *Combustion and Flame*, 96:150–162, 1994.

C. Crowe, M. Sommerfeld, and Y. Tsuji. *Multiphase flows with droplets and particles*. CRC Press, 1998.

C.T. Crowe. Review - Numerical models for dilute gas-particle flows. *Journal of Fluids Engineering*, 104:297–302, September 1982.

J.L. Cui, H.Q. Zhang, B. Wang, Y. Rong, and X.L. Wang. Flow visualization and laser measurement on particle modulation to gas-phase turbulence. *Journal of Visualization*, 9(3):339–345, 2006.

M.L. Davis and D.A. Cornwell. *Introduction to environmental engineering*. McGraw Hill, 3rd edition, 1998.

M. Deussner. Clinker burning with reduced NOx emissions. *World Cement*, pages 52–58, December 1995.

M. DiGiacinto, F. Sabetta, and R. Piva. Two-way coupling effects in dilute gas-particle flows. *Transaction of the ASME*, 104:304–312, September 1982.

J. Dirgo and D. Leith. *Design of Cyclone Separators*, volume 4, chapter 41, pages 1281–1306. Gulf Publishing Co., 1986.

R. Domann and Y. Hardalupas. A study of parameters that influence the accuracy of the Planar Droplet Sizing (PDS) technique. *Particle and Particle System Characterization*, 18:3 – 11, 2001a.

R. Domann and Y. Hardalupas. Spatial distribution of fluorescence intensity within large droplets and its dependence on dye concentration. *Applied Optics*, 40:3586 – 3597, 2001b.

W. Du, C. Gopalakrishnan, and K. Annamalai. Ignition and combustion of coal particle streams. *Fuel*, 74(4):487 – 494, 1995.

D. Dunsome. Staged combustion for NOx control at the Calaveras Tehachapi plant. *World Cement*, February 1995.

J.K. Eaton and J. R. Fessler. Preferential concentration of particles by turbulence. *International Journal of Multiphase Flow*, 20:169–209, 1994.

EIA. [http://www.eia.doe.gov/emeu/iea/coal.html]. Technical report, Energy Information Administration, U.S. Government, 2005.

T. Elperin, N. Kleeorin, and I. Rogachevskii. Dynamics of particles advected by fast rotating turbulent fluid flow: Fluctuations and large-scale structures. *Physical Review Letters*, 81(14):2898–2901, 1998.

R.J. Essenhigh, M.K. Misra, and D.W. Shaw. Ignition of coal particles: A review. *Combustion and Flame*, 77:3–30, 1989.

J. Fan, L. Zhang, H. Zhao, and K. Cen. Particle concentration and particle size measurements in a particle laden turbulent free jet. *Experiments in Fluids*, 9:320–322, 1990.

J. Fan, H. Zhao, and K. Cen. An experimental study of two-phase turbulent coaxial jets. *Experiments in Fluids*, 13:279–287, 1992.

J. Fan, H. Zhao, and K. Cen. Particle concentration and size measurments in two-phase turbulent coaxial jets measurements in two-phase turbulent coaxial jets. *Chemical Engineering Communications*, 156:115–129, 1996a.

J. Fan, H. Zhao, and J. Jin. Two-phase velocity measurements in particle-laden coaxial jets. *The Chemical Engineering Journal*, 63:11–17, 1996b.

J. Fan, Z. Zhang, L. Chen, and K. Cen. New stochastic particle dispersion modeling of a turbulent particle-laden round jet. *Chemical Engineering Journal*, 66:207–215, 1997.

J.R. Fessler and J.K. Eaton. Turbulence modification by particles in a backward-facing step flow. *Journal of Fluid Mechanics*, 394:97–117, 1999.

J.R. Fessler, J.D. Kulick, and J.K. Eaton. Preferential concentration of heavy particles in a turbulent channel flow. *Physics of Fluids*, 6(11):3742–3749, 1994.

D. Fleckhaus, K. Hishida, and M. Maeda. Effect of laden solid particles on the turbulent flow structure of a round free jet. *Experiments in Fluids*, 5:323–333, 1987.

R. Foreman. Mass loading and Stokes number effects in steady and unsteady particle-laden jets. Master's thesis, Univeristy of Adelaide, 2008.

W. Fulkerson, R.R. Judkins, and M.K. Sanghvi. Energy from fossil fuels. *Scientific American*, pages 83–89, September 1990.

S. Geiss, A. Dreizler, Z. Stojanovic, M. Chrigui, A. Sadiki, and J. Janicka. Inverstigation of turbulence modification in a non-reactive two-phase flow. *Experiments in Fluids*, 36:344–354, 2003.

I. Gillandt, U. Fritsching, and K. Bauckhage. Measurement of phase interaction in dispersed gas/particle two-phase flow. *International Journal of Multiphase Flow*, 27: 1313–1332, 2001.

I. Goldhirsch and G. Zanetti. Clustering instability in dissipative gases. *Physical Review Letters*, 70(11):1619–1622, 1993.

R.A. Gore and C.T. Crowe. Effect of particle size on modulating turbulent intensity. *International Journal of Multiphase FLow*, 15(2):279–285, 1989.

Y. Hagiwara, T. Murata, M. Tanaka, and T. Fukawa. Turbulence modification by the clusters of settling particles in turublent water flow in a horizontal duct. *Powder Technology*, 125:158–167, 2002.

E. Hansen. Burning of solid waste in cement kilns. *World Cement*, pages 15–18, March 1993.

Y. Hardalupas and S. Horender. Fluctuations of particle concentration in a turbulent two-phase shear layer. *International Journal of Multiphase Flow*, 29:1645–1667, 2003.

Y. Hardalupas, A.M.K.P. Taylor, and J.H. Whitelaw. Velocity and particle-flux characteristics of turbulent particle-laden jets. *Proceedings of the Royal Society of London*, 426:31–78, 1989.

P.O. Hedman and L.D. Smoot. Particle-gas dispersion effects in confied coaxial jets. *American Institute of Chemical Engineering*, 21(2), 1975.

G. Hetsroni. Particle-turbulence interaction. *International Journal of Multiphase Flow*, 15(5):735–746, 1989.

S.J. Hill, G.J. Nathan, and R.E. Luxton. Precessing and axial flows following a sudden expansion in an axisymmetric nozzle. In *11th Australiasin Fluid Mechanics Conference*, University of Tasmania, Hobart, Australia, December 1992.

K. Hishida, K. Kaneko, and M. Maeda. Turbulence structure of a gas-solid two-phase circular jet (in japanese). *Transactions from the Japanese Society of Mechanical Engineers*, 51:2330–2337, 1985.

K. Hishida, A. Ando, and M. Maeda. Experiments on particle dispersion in a turublent mixing layer. *International Journal of Multiphase Flow*, 18(2):181–194, 1992.

IPCC. Fourth assessment report - summary for policy makers. Technical report, Intergovernmental Panel on Climate Change, 2007.

B.-H. Jou, H.-J. Sheen, and Y.-T. Lee. Particle mass loading effect on a two-phase turbulent downward jet flow. *Particle and Particle Systems Characterization*, 10: 173–181, 1993.

T. Kajishima and S. Takiguchi. Interaction between particle clusters and particle-induced turbulence. *International Journal of Heat and Fluid Flow*, 23:639–646, 2002.

P. A. M. Kalt and C.H. Birzer. Calibrations for planar laser nephelometry in densely seeded two-phase flows. In *4th Australian Conference on Laser Diagnostics in Fluid Mechanics and Combustion*, The Univeristy of Adelaide, Australia, 2005.

P. A. M. Kalt and G.J. Nathan. Corrections to facilitate planar imaging of particle concentration in particle-laden flows using mie-scatting part 2: Diverging laser sheets. *Applied Optics*, 46(30):7227–7236, 2007.

P. A. M. Kalt, C.H. Birzer, and G.J. Nathan. Corrections to facilitate planar imaging of particle concentration in particle-laden flows using mie-scatting part 1: Collimated laser sheets. *Applied Optics*, 46(23):5823–5834, 2007.

P.A.M. Kalt and M.B. Long. OMA - image processing for Mac OS X. *www.oma-x.org*, 2008.

J.D. Kulick, J.R. Fessler, and J.K. Eaton. Particle response and turbulence modification in fully developed channel flow. *Journal of Fluid Mechanics*, 277:109–134, 1994.

M.K. Laats and F.A. Frishman. Scattering of an inert admixture of different grain size in a two-phase axisymmetric jet. *Heat Transfer - Soviet Research*, 2(6), November 1970.

S. Lain, M. Sommerfeld, and J. Kussin. Experimental studies and modelling of four-way coupling in particle-laden horizontal channel flow. *International Journal of Heat and Fluid Flow*, 23:647–656, 2003.

P. LeGal, N. Farrugia, and D.A. Greenhalgh. Laser Sheet Dropsizing of dense sprays. *Optics and Laser Technology*, 31:75–83, 1999.

Y. Levy and F.C. Lockwood. Velocity measurements in a particle laden turbulent free jet. *Combustion and Flame*, 40:333–339, 1981.

R.I. Loehrke and H.M. Nagib. Control of free-stream turbulence by mean of honeycombs: A balance between suppression and generation. *Transactions of the ASME*, September 1979.

E.K. Longmire and J.R. Eaton. Structure of a particle-laden round jet. *Journal of Fluid Mech*, 236:217–257, 1992.

J.L. Lumley. Passage of a turbulent stream thorugh honeycomb of large length-to-diameter ratio. *Transactions of the ASME*, June 1964.

J.L. Lumley and J.F. McMahon. Reducing water tunnel turbulence by means of a honeycomb. *Transactions of the ASME*, December 1967.

A.T. McQueen, S.J. Bortz, M.S. Hatch, and R.L. Leonard. Cement kiln NOx control. *IEEE Transaction on Industry Applications*, 31(1):36–43, January/February 1995.

N.P. Megalos, N.L. Smith, and D.K. Zhang. The potential for low NOx from a precessing jet burner of coal. *Combustion and Flame*, 124:50–64, 2001.

D. Modarress, J. Wuerer, and S. Elghobashi. An experimental study of a turbulent round two-phase jet. *Chemical Engineering Communications*, 28:341–354, 1984a.

D. Modarress, H. Tan, and S. Elghobashi. Two-component LDA measurements in two-phase turbulent jets. *AIAA*, 22(5):624–630, May 1984b.

A.A. Mostafa and H.C. Mongia. On the interaction of particles and turbulent fluid flow. *International Journal of Heat Mass Transfer*, 31(10):2063–2075, 1988.

A.A. Mostafa, H.C. Mongia, V.G. McDonell, and G.S. Samuelsen. Evolution of particle-laden jet flows: A theoretical and experimental study. *AIAA Journal*, 27(2):167–183, 1989.

P.J. Mullinger. Cement kiln firing and clear air requirements. *World Cement*, pages 27–31, December 1994.

G.J. Nathan and S.J. Hill. Performance assessment of the solid fuel Gyro-Therm burner. Interim Report Stage II RS720, FCT - Combustion Pty. Ltd., December 2001.

G.J. Nathan and S.J. Hill. Full scale assessment of the influence of a precessing jet of air on the performance of pulverised coal flame in a cement kiln. In *6th European Conference on Industrial Furnaces and Boilers (INFUB)*, April 2002.

G.J. Nathan and R.E. Luxton. Flame stability and emission charcteristics of the enhanced mixing burner. In *2nd European Conference on Industrial Furnaces and Boilers*, pages 5–14, April 1991.

G.J. Nathan and C.G. Manias. The role of process and flame interaction in reducting NOx emissions. *Combustion and Emissions Control*, pages 309–318, 1995.

G.J. Nathan, R.E. Luxton, and J.P. Smart. Reduced NOx emissions and enhanced large scale turbulence from a precessing jet burner. In *Twenty-Fourth Symposium (International) on Combustion*, pages 1399–1405. The Combustion Institute, 1992.

G.J. Nathan, J.P. Smart, and B.G. Jenkins. *Criterion for modeling Gryo-Therm burners (draft)*, 1995.

G.J. Nathan, S.J. Hill, and R.E. Luxton. An axisymmetric 'fluidic' nozzle to generate jet precession. *Journal of Fluid Mechanics*, 370:347–380, 1998.

G.J. Nathan, N.L. Smith, P.J. Mullinger, and J.P. Smart. Performance characteristics of, and an aerodynamic scaling parameter for, a practical PF burner design employing jet excitation to promote particle clustering. In *5th International Conference on Industrial Furnaces and Boilers (INFUB)*, Porto, Portugal, April 2000.

G.J. Nathan, J. Mi, Z.T. Alwahabi, G.J.R. Newbold, and D.S. Nobes. Impacts of a jet's exit flow pattern on mixing and combustion performance. *Progress in Energy and Combustion Science*, 32:496–538, 2006.

J.M. Nouri, J.H. Whitelaw, and M. Yianneskis. Particle motion and turbulence in dense two-phase flows. *International Journal of Multiphase Flow*, 13(6):729–739, 1987.

Y. Ono. Microscopical estimation of burning condition and quality of clinker. In *7th International Congress on Chemcial Cement*, pages I–206 I–211, 1980.

J.J Parham, G.J. Nathan, J.P. Smart, S.J. Hill, and B. G. Jenkins. The relationship between heat flux and NOx emissions in gas fired rotary kilns. *Journal of Institute of Energy*, 73:25–34, 2000.

J. Popper, N. Abuaf, and G. Hetsroni. Velocity measurements in a two-phase turbulent jet. *International Journal of Multiphase Flow*, 1:715–726, 1974.

S. Pothos and E.K. Longmire. Control of a particle-laden jet using a piezo-electric actuator. In *11th International Symposium on Applications of Laser Techniques to Fluid Mechanics*, 2002.

M.J. Prather and J.A. Logan. Combustion's impact on the global atmosphere. In *25th Symposium (International) on Combustion*, pages 1513–1527. The combustion Institute, 1994.

J.M. Rhine and R.J. Tucker. *Modelling of gas-fired furnaces and boilers and other industrial heating processes*. McGraw-Hill, 1991.

R.E. Rosensweig, H.C. Hottel, and G.C. Williams. Smoke-scattered light measurements of turbulent concentration fluctuations. *Chemical Engineering Science*, 15:111–129, 1961.

W. Ryan and K. Annamalai. Group ignition of a cloud of coal particles. *Journal of Heat Transfer*, 113:677–686, August 1991.

R. Sadr and J.C. Klewicki. Flow field characteristics in the near field region of particle-laden coaxial jets. *Experiments in Fluids*, 39:885–894, 2005.

J. Sakakibara, R.B. Wicker, and J.K. Eaton. Measurements of the particle-fluid velocity correlation and the extra dissipation in a round jet. *International Journal of Mulitphase Flow*, 22(5):863–881, 1996.

G.M. Schneider, J.D. Hooper, A.R. Musgrove, G.J. Nathan, and R.E. Luxton. Velocity and Reynolds stresses in a precessing jet flow. *Experiments in Fluids*, 22:489–495, 1997b.

J-S. Shuen, A.S.P. Solomon, Q-F. Zhang, and G.M. Faeth. Structure of particle-laden jets: Measurements and predictions. *AIAA Journal*, 23(3):396–404, 1985.

J.P. Smart. *On the effect of burner scale and coal quality on low NOx burner performance*. PhD thesis, University of London, London, England, March 1992.

N.L. Smith. The influence of precessing jet flows on particle trajectories, ignition and NOx emissions from, pulverised fuel flames. Upgrade report, University of Adelaide, April 1996.

N.L. Smith. *The influence of the spectrum of jet turbulence on the stability, NO_X emissions and heat release profile of pulverised coal flames*. PhD thesis, University of Adelaide, Department of Mechanical Engineering, October 2000.

N.L. Smith, D.K. Zhang, and G.J. Nathan. Pre-ignition particle heating mechanisms in precessing jet pulverised coal flames. In *Australian Symposium on Combustion*, 1997.

N.L. Smith, N.P. Megalos, G.J. Nathan, D.K. Zhang, and J.P. Smart. The role of fuel-rich clusters in flame stabilization and NOx emission reduction with precessing jet pulverised fuel flames. In *Twenty-Seventh Symposium (International) on Combustion*, pages 3173–3179. The Combustion Institute, 1998a.

N.L. Smith, N.P. Megalos, G.J. Nathan, D.K. Zhang, and J.P. Smart. Precessing jet burners for stable and low NOx pulverised fuel flames - Preliminary results from small-scale trails. *Fuel*, 77(9/10):1013–1016, 1998b.

N.L. Smith, G.J. Nathan, D.K. Zhang, and D.S. Nobes. The significance of particle clustering in pulversied coal flames. In *Proceedings of the Combustion Institute*, volume 29, pages 797–804, 2002.

K.D. Squires and J.K. Eaton. Particle response and turbulence modification in isotropic turbulence. *Physics of Fluids A*, 2(7):1191–1203, July 1990.

B.D. Stojkovic and V. Sick. Evolution and impingement of an automotive fuel spray investigated with simultaneous Mie/LIF techniques. *Applied Physics B*, 73:75–83, 2001.

Y. Tsuji, Y. Morikawa, and H. Shiomi. LDV measurement of an air-solid two-phase flow in a vertical pipe. *Journal of Fluid Mechanics*, 139:417–434, 1984.

Y. Tsuji, Y. Morikawa, T. Tanaka, and K. Karimine. Measurement of an axisymmetric jet laden with coarse particles. *International Journal of Multiphase Flow*, 14:565–574, 1988.

S.R. Turns. *An introduction to combustion.* McGraw Hill, 2nd edition, 2000.

H.C. Van De Hulst. *Light Scattering By Smaller Particles.* John Wiley and Sons, Inc., 1957.

T.F. Wall, V. Subramanian, and P. Howley. An experimental study of the geometry, mixing and entrainment of particle-laden jets up to ten diameters from the nozzle. *Transactions of the Institute of Chemical Enegineers*, 60, 1982.

C. Wark, K. Eickmann, and C. Richards. The structure of an acoustically forced, reacting two-phase jet. *Combustion and Flame*, 120:539–548, 2000.

E. Wassen and T. Frank. Simulation of cluster formation in gas-solid flow induced by particle-particle collisions. *International Journal of Multiphase Flow*, 27:437–458, 2001.

R.B. Wicker and J.K. Eaton. Effect of injected longitudinal vorticity on particle dispersion in a swirling, coaxial jet. *Transactions of the American Society of Mechanical Engineers*, 121:766–772, 1999.

R.B. Wicker and J.K. Eaton. Structure of a swirling, recirculating coaxial free jet and its effect on particle motion. *International Journal of Mulitphase Flow*, 27:949–970, 2001.

A. Williams, M. Pourkashanian, J.M. Jones, and L. Rowlands. A review of NOx formation and reduction mehcanisms in combustion systems, with particular reference to coal. *Journal of the Institute of Energy*, 70:102–113, September 1997.

C.M. Winkler, S. L. Rani, and S.P. Vanka. Preferential concentration of particles in a fully developed turbulent square duct flow. *International Journal of Multiphase Flow*, 30:27–50, 2004.

C.Y. Wong, P.V. Lanspeary, G.J. Nathan, R.M. Kelso, and T. O'Doherty. Phase-averaged velocity in a fluidic precessing jet nozzle and in its near external field. *Experimental Thermal and Fluid Science*, 27:515–524, 2003.

A.M. Wood, W. Hwang, and J.K. Eaton. Preferential concentration of particles in homogeneous and isotropic turbulence. *International Journal of Multiphase Flow*, 31:1220–1230, 2005.

J.J. Wylie and D.L. Koch. Particle clustering due to hydrodynamic interactions. *Physics of Fluids*, 12(5):964–970, May 2000.

C.-N. Yeh, H. Kosaka, and T. Kamimoto. A fluorescence/scattering imaging technique for instantaneous 2-D measurements of particle size distribution in a transient spray. In *Proceeding of the 3rd Congress on Optical Particle Sizing*, Yokohama Japan, 1993.

D.K. Zhang and T.F. Wall. An analysis of the ignition of coal dust clouds. *Combustion and Flame*, 92:475–480, 1993.

L. Zimmer, Y. Ikeda, R. Domann, and Y. Hardalupas. Simultaneous LIF and Mie scattering measruements for branch-like spray cluster in industrial oil burner. In *AIAA conference*. AIAA, 2002a.

L. Zimmer, Y. Ikeda, K. Fujimoto, and T. Nakajima. Planar Droplet Sizing for the characteriszation of clusters in an industrial gun-type burner. In *11th International Symposium of Applications of Laser Techniques to Fluid Mechanics*, Lisbon-Portugal, 2002b.

C.K. Zoltani and A.F. Bicen. Velocity measurements in a turbulent, dilute, two-phase jet. *Experiments in Fluids*, 9:295–300, 1990.